Point-by-point response to the reviews

Response to Farquharson #2

Coats and her co-authors have addressed the majority of my previous comments satisfactorily, either by well-argued rebuttal or by making amendments to the text, for which I applaud them. In particular, they have improved the clarity of the manuscript in many parts, and performed a more in-depth interrogation of their data using the various micromechanical damage models discussed in the text. I only have one outstanding concern, which relates to the balancing of units in Eq. 11. As highlighted in my original review, the units (as stated) do not balance out if b does not equal 1. This is a fundamental problem stemming from the use of an exponent model. The authors counter this comment by couching their constant k in units of $\sqrt{Pa.s}$ (i.e. $Pa.s^b$). While this is not particularly satisfactory (the "flow consistency index" has an ambiguous physical meaning if it is not in measurable units, i.e. Pa.s as it is currently explicitly defined in the manuscript), it does solve the immediate unit balancing problem. However, it is not a suitable solution as later in the manuscript their non-unity value of b appears again (in the Deborah number equation). The authors indicate that

$$De = \frac{\left(\sigma/k\right)^{1/b}\eta_m}{G_\infty}$$

If the authors use units of $Pa.s^b$ to define k, then the units balance thus:

$$De = \frac{\left(Pa/\sqrt{Pa.s}\right)^2}{Pa}Pa.s$$

when b = 0.5, which is to say De = Pa. The Deborah number is a dimensionless ratio (a timescale divided by a timescale), so presenting it in units of pressure is clearly not desirable, and I'm sure was not the authors' intention. Moreover, this assumes that b is a "neat" fraction, so that 1/b is resolved into an integer and the degree of the k radical is also an integer. Things become more complex if 0.5 < b < 1.0. I urge the authors to look more critically at this problem, and perhaps reconsider the use of a power-law model, which propagates problems when incorporated into more involved analyses. Failing this, the authors should at least take care that their representation of k and b do not lead to errors later in the manuscript. For example, defining a critical strain rate λ such that λ = 1 s⁻¹, viscosity could be presented as

$$\eta_A = k\left(\frac{\dot{\epsilon}}{\lambda}\right)^{b-1}$$

such that the units balance out without the need to redefine k:

$$Pa.s = Pa.s\left(\frac{s^{-1}}{s^{-1}}\right)^{0.5} \rightarrow Pa.s = Pa.s\sqrt{1}$$

I acknowledge that this may not be a perfect (or even correct) solution, but it may be a useful avenue for the authors to explore. In any case, the authors ought to discuss some of the shortcomings of their power-law approach. This point aside, I recommend this article for publication in Solid Earth.

Yours faithfully,

Jamie Farquharson

-We thank the reviewer for taking the time to review the manuscript for a second time. We acknowledge his concerns over unit balance and refer him to the reference Jahangiri et al., 2012, now referred to in the manuscript. Here it is stated that the Ostwald–de Waele or power-law fluid relationship is defined as: $\tau = K\gamma\,n$, where τ is shear stress (Pa); K is the flow consistency

1

index (Pa.s^n); γ is the Shear rate (s^{-1}) and n is the flow behaviour index. The reviewer has inadvertently taken the units of k as (Pa.s)$^b \neq$ Pa.s^b. We have found a technical error in our text on line 610 which stated that the unit of k were Pa.s, this has now been amended so that the unit of k are defined as Pa.s^b.

This simple unit correction means that the units of Equation 12, the Deborah number equation, balance as follows:

$$De = \frac{(\frac{Pa}{Pa.s^b})^{1/b}}{Pa} \, Pa.s \;\rightarrow\; De = \frac{(\frac{1}{s^b})^{1/b}}{Pa} \, Pa.s \;\rightarrow\; De = \frac{s^{-1}}{Pa} \, Pa.s \rightarrow De = 1$$

Thus, the Deborah number is dimensionless as expected.

We thank the reviewer for his efforts which have much improved our manuscript.

Jahangiri, P., Streblow, R. and Müller, D.: Simulation of Non-Newtonian Fluids using Modelica, Proc. 9th Int. Model. Conf., 57–62, doi:10.3384/ecp1207657, 2012

Response to Farquharson

Dear Editor and authors,

I have read the manuscript *Failure criteria for porous dome rocks and lavas: a study of Mt. Unzen, Japan* with great interest. By way of a targeted experimental campaign, Coats *et al.* map

out the failure conditions for suites of variably-porous crystalline andesite as a function of different temperatures and strain rates. The conclusion of the study is an empirical threshold for the

failure of these materials derived from their data.

The article is assiduous and well written, the experimental protocol appears rigorous, and the study yields a wealth of interesting new data. Overall, this article represents a commendable

research effort from the authors. Where the authors perhaps do themselves a disservice is in the analysis of their data, which could be more comprehensive. Below I outline minor

comments or concerns that I feel the authors should address or clarify. Pending these changes, I recommend this article for publication in *Solid Earth*.

Yours faithfully,
Jamie Farquharson

(Please forgive the clumsy formatting, I was forced to write this report on my phone)

Lines 39-56: Sparks (1997) is highly relevant to this study, and is a surprising omission here.
Sparks (1997) The causes and consequences of pressurisation in lavas done eruptions. *Earth and Planetary Science Letters*
150(3-4): 177-189
- We thank the reviewer for bringing this to our attention and have added the reference in question, an oversight given its relevance to the fundamentals to this study.

Line 66: how do the authors define the "temperature range of interest"?

75   - Webb and Dingwell (1989) compiled a large dataset of elastic modulus at infinite frequency, G_∞, for silicate melts and many other compounds, over a range of temperatures. Previous studies found that G_∞ ranges from 5 to 42 GPa at room temperature for glasses with silica contents ranging between 5-99 mole% (Bansal and Doremus, 1986), and at temperatures between 400 and 1600 °C, G_∞ = 33 GPa ± 5% (Bucaro and Dardy, 1974). Webb and Dingwell (1989) added data to find that for silicate melts and glasses, G_∞ ranges between 3.2 and 32 GPa and thus can be approximated at $10^{10\pm0.5}$

80   as it only weakly varies with temperature (unlike viscosity). This brings an important simplification to the modelling of viscoelastic melts, which has been pivotal in its integration to volcanology. Therefore, we can assume $G_\infty = 10^{10\pm0.5}$ for all silicate melts (and glasses) at ~20-1600 °C, which extends beyond the temperature range of most (contemporaneous) volcanic systems reported in the literature. Hence, the "temperature range of interest" is all volcanic temperatures.

85

Line 101: it might be useful to provide the equation for *Ca* here.

- The paragraph details our knowledge of complex lavas (such as dome lavas) containing crystals and bubbles. The capillary number is highly relevant in aphyric lavas, but in the lavas discussed here, it remains to be adapted, which is beyond the scope

90   of this study. Hence, we wish not to introduce the equation here and believe a qualitative description is sufficient.

Lines 134-144, and elsewhere: the authors describe two inclusion models which they highlight may explain their data: the pore-emanating crack model of Sammis and Ashby, and the sliding

95   wing crack model of Ashby and Sammis. However, the authors do not go on to employ either of these models subsequently. As I intimated previously, it seems something of a shame that

there is not a more involved analysis of these data. Analytical solutions for both these models are provided by Zhu *et al.* 2010 *JGR* and Baud *et al.* 2014 *IJRMS*, respectively. Previous

authors have utilised one or other in order to describe the failure behavior of volcanic materials or analogues, for example Zhu

100   *et al.* 2011 *JGR* (for tuffs), Vasseur *et al.* 2013 *GRL* (sintered

glass), Heap *et al.* 2014 *JGR* (andesite), Zhu *et al.* 2016 *JGR* (basalts). Moreover, Zhu *et al.* 2011 extend the analytical solution to a dual-porosity medium, and Zhu *et al.* 2016 combine both

models so as to have a representative element volume comprised of an effective medium including a pore surrounded by many cracks. If Coats *et al.* were to interrogate their data in a

105   similar manner, they may be able to glean valuable information about the governing microstructural elements in their samples contributing to failure (for example by contouring for different

values of KIc/√[πr]).

-We thank Dr Farquharson for his detailed comments. Indeed, we had previously investigated the comparison of our data with the pore and wing-crack models but had excluded it from the results based on the assumptions of parameters we had to make

110   in fitting the wing crack model. However, as the reviewer asked for this data we felt it important to extend our analysis. The following has been added to the manuscript in section 1.3:

An analytical estimation of this model was derived by Zhu et al., (2010) to estimate the uniaxial compressive stress (σ) of a sample, with an average pore radius (r), as a function of its porosity (φ) and the fracture toughness (K_{IC}):

115   $\sigma = \dfrac{1.325}{\varphi^{0.414}} \dfrac{K_{IC}}{\sqrt{\pi r}},$ (2)

The analytical approximation for this model was developed by Baud et al., (2014):

$$\sigma = \frac{1.346}{\sqrt{1+\mu^2}-\mu}\frac{K_{IC}}{\sqrt{\pi c}}D_0^{-0.256}, \quad (3)$$

where μ is the friction coefficient of the crack, c is the half–length of a pre–existing crack, and D_0 is an initial damage parameter (which takes into consideration the number of cracks per unit area and their angle with respect to the principal stress).

And the following in section 4.1.2:

The uniaxial compressive strength was calculated for the samples for both the pore–emanating crack model of Sammis & Ashby (1986) (Eq. 3) and the sliding wing crack model of Ashby & Sammis (1990) (Eq. 4). For the former, the uniaxial compressive strength was calculated with varying values of $\frac{K_{IC}}{\sqrt{\pi r}}$ from 5 MPa to 25 MPa (Fig. 11). For the latter, approximate values for μ, $\frac{K_{IC}}{\sqrt{\pi c}}$ and D_0 were taken from Table 3 in Paterson and Wong (2005) as 0.51, 20–30 MPa and 0.3–44, respectively. This gave a range of estimated strength between 54 and 90 MPa (Fig. 11). At higher porosities, > 0.25, the pore–emanating crack model with $\frac{K_{IC}}{\sqrt{\pi r}}$ = 5–10 MPa seems to fit the data well, whereas for most rocks with porosities of 0.12–0.2 $\frac{K_{IC}}{\sqrt{\pi r}}$ = 10–15 MPa is a better fit. This could be explained by a decrease in the pore radius at these porosities, leading to higher values of $\frac{K_{IC}}{\sqrt{\pi r}}$, though, as the samples are heterogeneous and pore radius variability is high we cannot observe this (Figure 3). For the densest rocks in the study (~0.08–0.12), the UCS data would suggest yet a higher $\frac{K_{IC}}{\sqrt{\pi r}}$ of 20–25 MPa. The pore–emanating crack model could explain this switch in behaviour if there was a fundamental change in pore radius. However, the switch could also be explained by a transition in failure mechanism from pore–emanating cracks to wing cracks, meaning the wing–crack model would be more applicable. Alternatively, it may be a complex combination of the two. Although the solutions to the sliding wing–crack model are non–unique, as there are few experimentally constrained parameters, when combined with information gained from the pore structures (Fig. 3), the results of the modelling presented (Fig. 11) give us an insight into the dominant micromechanical failure mode of our samples. It is likely that the complex pore structures of these lavas, generated by a combination of vesiculation, deformation and cooling-driven contraction require an as-yet undefined combination of the two models. The weighting towards one or the other, however indicates that for the higher porosity specimens the behaviour of failure could be described using the pore–emanating crack model of Sammis & Ashby (1986), whereas in the lower porosity samples deformed in uniaxial compression, the main failure mechanism is explained by the sliding wing–crack model of Ashby & Sammis (1990).

The following figure and caption were also added to the manuscript as new Figure 11:
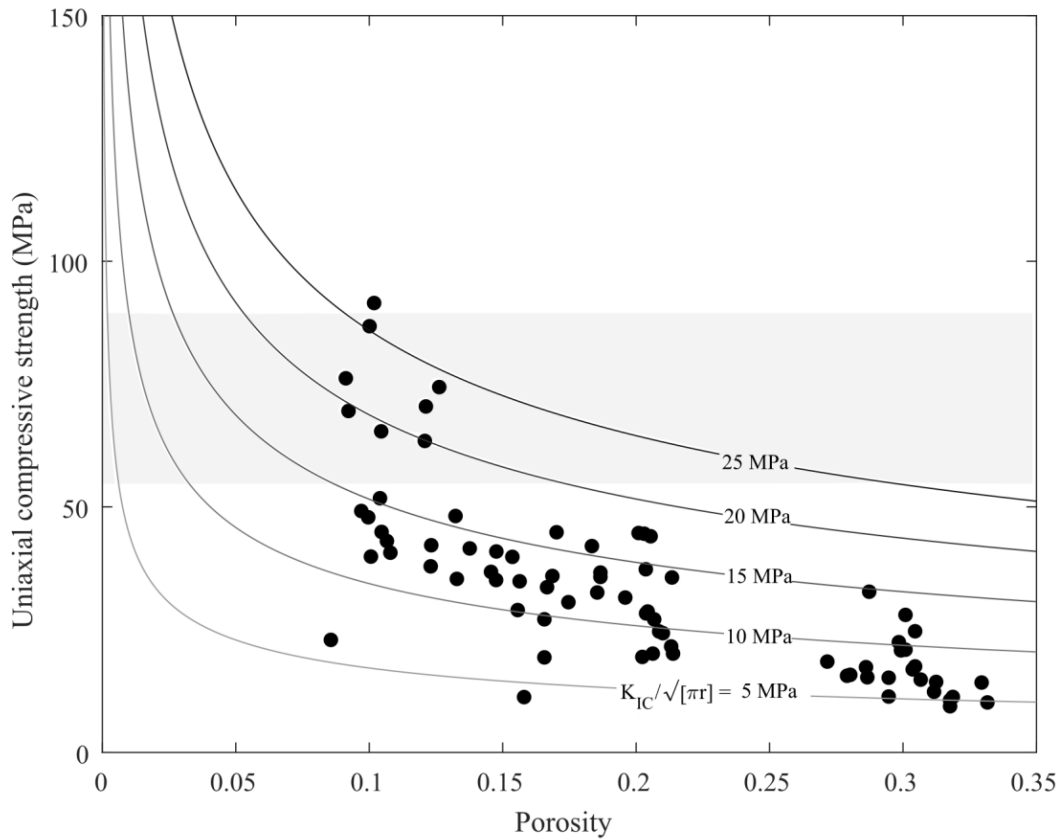
4

Figure 11 Plot of uniaxial compressive stress against porosity showing the ambient temperature mechanical data (black dots), along-side contours of various values of $\frac{K_{IC}}{\sqrt{\pi r}}$ (5–25 MPa) from the pore–emanating crack model (Eq. 2). The range of UCS given by the wing-crack model is also plotted as a shaded region. The mechanical data are cross-cut by the contours, suggesting a change in the dominant porous structure. At porosities > 0.25 the UCS given by the pore-emanating crack model with $\frac{K_{IC}}{\sqrt{\pi r}}$ = 5–10 MPa seems to fit the data well. For porosities ranging from 0.12–0.2 the UCS given by the pore-emanating crack model with $\frac{K_{IC}}{\sqrt{\pi r}}$ = 10–15 MPa encloses the data. The UCS for the densest rocks in the study (~0.08–0.12) would suggest yet a higher $\frac{K_{IC}}{\sqrt{\pi r}}$ of 20–25 MPa. For porosities < 0.1 the UCS given by the wing–crack model is similar to the mechanical data (σ = 54.2–89.7 MPa).

Line 146: the authors should state clearly that they here define "lava" as something at high temperature (volcanic rocks may often also be referred to as lava).

-We thank the reviewer for this comment and agree the definition between cold lava and

high temperature lava was unclear at certain points in the manuscript. We have edited the manuscript with the following note:

'[note: From here, samples deformed at high temperature will be defined as lavas, and those tested at room temperature as rocks].'

Line 184: in which direction has the lobe moved (*i.e.* rotation, inflation, advance)?

-We have now added that: The mechanism of movement is thought to be down-slope advancement to the East (Matsushima and Takagi, 2000).

Line 279, and elsewhere: is this a change of 1 % or 1 vol.%?

-It is a change of 1 vol.%. We have changed the manuscript to read 0.01 in place of 1%, in line with the method of reporting porosity used throughout the manuscript (e.g. Table 1). We have also noted this change elsewhere in the manuscript so that porosities are reported as a fraction. Where crystals are concerned we have reported these as vol.%

Line 296 and 298: which software was used to run the scripts? Are they publicly available?

-The software used to run the scripts was MATLAB. A version of the script is now freely available on Github (https://doi.org/10.5281/zenodo.1287237). This has now been made clear in the manuscript.

Line 322: the observation that in dense materials the connectivity is higher than in porous materials is somewhat counter-intuitive, and runs counter to results from previous researchers
(Farquharson *et al.* 2015 *JVGR* and Collombier *et al.* 2017 *EPSL*, both of which noted that connectivity generally increased with increasing porosity). Do the authors have any comment on
this difference?

-We agree it seems counter intuitive, but the difference is very small: a matter of 0.01-0.02 unconnected pores. We attribute this to the presence of more small, isolated pores in the high porosity samples than in the low porosity samples. We also note that the porosity range of our rocks is considerably smaller (0.09-0.32) than Farquharson et al., (2015) (0.025-0.73) and Collombier et al., (2017) (~0.0-1.0), and so note that we are not evaluating the same range as these other studies. Our 'high porosity' samples could be considered low porosity in comparison to these other studies and so a comparison cannot be clearly drawn.

Line 342: cristobalite isn't a polymorph of quartz. Rather, both quartz and cristobalite are silica polymorphs.

-We thank the reviewer for bringing this to our attention and agree the text would be clearer if the polymorph was referred to as a silica polymorph. The manuscript and Figure 3 have been edited in accordance with this.

Line 355-359: did sample volume change upon heating? This really is surprising, as one would anticipate thermal cracking upon heating and subsequent cooling, due to thermal expansion
mismatch between the constituent microstructural components (*e.g.* Browning *et al.* 2016 *GRL*). This may be especially pronounced given the existence of cristobalite in your samples,
which undergoes a significant volumetric change as it transitions between its alpha and beta forms (a function of temperature: see for example, Damby *et al.* 2014 *JAC*).

- We refer Dr Farquharson to the supplementary data, S5. Thermo-mechanical analysis (TMA) of the Mt. Unzen dome rock shows thermal expansion upon heating until the softening point of the material. We also refer him to lines 503-506 in the original manuscript ("A recent study by Eggertsson et al., *in review*, found that the strength and porosity of samples that hosted microfractures (like Mt. Unzen dome rock) were not affected by thermal stressing, while those that showed a trivial fraction of pre-existing micro-fractures were more significantly influenced through thermal stressing and as a result became more permeable."). In accordance with Eggertsson et al., (2018), as our samples contained a pre-existing network of microfractures they were not readily fractured by thermal expansion and contraction.

We also would like to point out that samples containing cristobalite, UNZ-13 (see Figure 3), were not tested at high temperature nor thermally stressed to avoid adding effects of mineralogical reactions in this study that would not be relevant in the lava dome setting – i.e. the cristobalite post-dates high-temperature emplacement. We also would like to state that the heating and cooling rates used (4 °C min^{-1}) were low enough to limit the differential expansion of the samples (that is, caused by temperature gradients across the samples, which also contribute to thermal cracking and which are not always considered independently from differential expansion of the constituent phases).

indicate that thermal stressing doesn't affect the porosity of the samples. Moreover, I would think that induced cracking would serve to decrease the material stiffness, rather than increase it.

I suggest the authors re-word this section for clarity and consistency.

215   - No, the rock stiffness (i.e. Young's Modulus) does not increase with thermal stressing, it in fact decreases (Figure 9c and lines 479-498, original manuscript). We attribute the initial convex portion of the stress-strain curves to the closure of microcracks perpendicular and sub-parallel to the principal stress (as in Heap et al., 2014, JGR). This initial section of the stress-strain curve is more pronounced in the case of the thermally stressed samples (Figure 4c), indicating that either 1) the width of pre-existing macro-fractures increased or that 2) more microfractures (generated by thermal stressing) are available

220   to close; however, the porosity determined from post-thermal stressing pycnometric measurements suggests that no microfracturing took place. We suggest that thermal stressing did indeed slightly modify the network of micro-fractures but on too-small a scale to affect the UCS and pycnometry results. The manuscript has been edited to highlight this observation and changes have been made to section 3.2.1.

225   Line 400-401: as previously, it would by useful if the authors were to distinguish between % and vol. %.

       - We have amended this throughout, as previously mentioned.

       Line 431: Young's modulus ought to be capitalised. Also, there is a full stop missing at the end of this sentence.

       -These typos have now been corrected in the manuscript.

230

       Line 441-445: see comment above concerning these inclusion models.

       -We have added analysis of these micromechanical models; see reply to comments above.

       Line 470: could this observation be due to pore anisotropy (*e.g.* Bubeck *et al.* 2017; Griffiths *et al.* 2017)?

235   - Here the reviewer is referring to the statement "This suggests that these samples are stiffer than the other specimens tested, and indeed those experiments reached unusually high peak stresses at relatively low strains to failure.", which is discussing samples UNZ-2 and UNZ-13. We looked at the thin section of UNZ-13 and conclude that the pore anisotropy may indeed contribute. Here the pores are preferentially aligned toward the principal stress direction (Fig.3) and so this is a likely case for stiffening. The manuscript has been amended at this line and in the conclusions section, see the reviewer's comment below.

240   For UNZ-2 it is possible that these vesicles had a pore anisotropy that could have led to minor strengthening and an increase in stiffness, like that seen by Bubeck *et al.* (2017) and Griffiths *et al.* (2017). Yet, our investigation was not sufficient to constrain and explicitly state this as fact.

       Line 480-481: do the authors have any information on the pore size distribution or pore anisotropy that could help explain

245   this?

       -The reviewer is referring to the following statement "In addition, thermally stressed samples have slightly lower (~ 0.5–1.5 GPa) Young's Moduli than their unstressed equivalents, as previously noted in dacites from Mt. St. Helens (Kendrick et al., 2013a). This highlights a potential change in

       porosity distribution that was not recognised by other means (e.g. total porosity, strength)."

250

The decrease in Young's Modulus is very slight, therefore information on pore size distribution or pore anisotropy, e.g. from a thin section, is unlikely to help in explaining this decrease. As the samples are very heterogenous any change in pore behaviour would be difficult to quantify as the change would be expected to be small and comparing the exact material before and after thermal stressing is not possible in thin section. This would rely on pre and post stressing CT scans which are time consuming and would likely provided reconstruction with spatial resolution too low to accurately distinguish slight pore morphology changes. Hence, the most sensitive measure of change we have is the pycnometry – which as stated previously, did not indicate any change – and the mechanical data which shows a decrease in Young's modulus.

Line 525: shear-induced development of pore connectivity was also shown experimentally by Kushnir *et al*. 2017 *EPSL*.

-We regret the oversight in not citing this article and have now added it to the manuscript.

Line 535-560: as with my previous comments concerning the inclusion models of Ashby and Sammis and Sammis and Ashby, I believe the authors could extend this Deborah number

analysis some more. As far as I can tell, the dimensions of Equation 10 only balance out if *b* = 1. Pa = [Pa.s × s^-1] is fine (*b* = 1), but Pa = √[Pa.s × s^-1] is not, as would be the case were *b* = 0.5. To me,

this highlights a serious shortcoming in the empirical approach adopted here, especially as there has been more recent work on the topic which adopt physical rather than empirical

parameters, for example the Wadsworth *et al*. 2017 chapter referenced elsewhere in the manuscript. For example, that chapter addresses the physical scaling of *De* with crystal

content. Ultimately, a similar physical approach could yield a much more generally applicable failure criterion for porous materials.

-With regards to the units of Equation 11, the equation balances if constant k has units of MPa.s$^{1/2}$, as shown below:

$$\sigma(MPa) = k\left(MPa.s^{1/2}\right).\dot{\varepsilon}_{obs}(s^{-1})^{b=1/2}$$

In the Wadsworth *et al*. 2017 chapter, only the single or two-phase cases are discussed. Within this chapter, the equation for the Deborah number is only given for a two-phase, crystal-bearing medium (Equation 3, Wadsworth et al., 2017). Here we are working with a three-phase medium, for which no models exist and thus an empirical approach must be adopted. For the sake of this argument, if we assume that the material from Mt. Unzen is a two-phase, crystal-bearing medium we can use Figure 2 in Wadsworth et al., (2017) to calculate the critical Deborah number expected. Given that the Unzen material has a crystal content, ϕ_x, (microlites+phenocrysts) of ~0.75 we can use this to find the critical Deborah number if no bubbles were present. To find this critical value, the maximum packing fraction, ϕ_m, also has to be known. As ϕ_m is defined as "the volume fraction of particles beyond which there is no space remaining which would accommodate further particles" (Mader et., 2013), it is clear from thin section and SEM images that our material has not yet reached ϕ_m (see Fig. 3). Therefore, it can be assumed that for the Mt. Unzen material investigated here, $\phi_m \approx 0.76 - 0.99$, and $\frac{\phi_x}{\phi_m}$ = 0.76-0.99. According to Figure 2 in Wadsworth et al. (2017), this range gives the range of critical Deborah number as 9.9x10^{-5}-7.6x10^{-4}. Therefore, our estimation of the critical Deborah number of the dense material as 9.4x10^{-5} -6.6 x10^{-4} is a very reasonable one indeed.

The method used in this manuscript to find the Deborah number and then critical Deborah numbers is empirical but, as well as giving a working solution to find the Deborah number for a three-phase material, it shows that there is a reduction in critical Deborah number due to the addition of particles and also provides a linear relationship for the critical Deborah number and the addition of pores. This study is a novel, first-step approach into characterising the De number and failure constraints on real, volcanic samples using mechanical testing data.

using *exp* as a subscript is a little ambiguous (at first glance I presumed it signified an exponential).

-For clarity, we have changed the *exp* subscript to *obs* to stand for observation in line with the symbol for observation time t_{obs}.

Oswald should presumably be Ostwald.

-Yes, this has now be changed in the manuscript.

here, the authors state values of k and b of 1653 and 0.5, yet in the caption for Figure 10, the values are $k = 1606$ and $b = 0.7755$. Which of these are correct? What is the sensitivity of the the following analysis to variations on k and/ or b?

-We thank the reviewer for pointing out this typo. The correct k and b values were those written within the manuscript. These values shifted due to an addition of data to the plot. We have now added the standard error of estimate for these values to the plot to show the variation of k and b.

Equation 11: Based on equation 9, shouldn't σ relate to strain rate × viscosity (or equivalently, $De \times G\infty$)?

-We believe the reviewers confusion lies with the presentation of the equations, Equation 8 has now been edited from:

$$De = {\eta_m}/{G_\infty t_{obs}}$$

to:

$$De = \frac{\eta_m}{G_\infty t_{obs}}$$

(now Equation 9)

And Equation 9 from:

$$De = \dot{\varepsilon}_{obs}\, \eta_m / G_\infty$$

to:

$$De = \frac{\dot{\varepsilon}_{obs}\, \eta_m}{G_\infty}$$

(now Equation 10)

To get to Equation 11 from Equation 9 a substitution is made for $\dot{\varepsilon}_{obs}$, which from Equation 10 is $\dot{\varepsilon}_{obs} = \left(\frac{\sigma}{k}\right)^{1/b}$.

(now Equation 11)

this is in contrast to existing theory, models, and experimental data. Perhaps this effect is masked in your data by sample heterogeneity? I would be wary of including this point as a key conclusion of the study.

-The reviewer is referring to conclusion 3: The orientation of a vesicle may not necessarily have a discerning control on the strength of a rock, however it does have an influence on the strains reached at failure and, as such, the Young's Modulus. Here we agree with the reviewer and this point has now been removed as a key conclusion, in light of the discussion regarding anisotropy in the reply to an earlier reviewer comment above made regarding line 470. The manuscript has also been edited to reflect this change.

Figure 4: there appears to be some data obscured by the legend in panels *a* and *b*.

-We thank the reviewer for his keen eye and have clarified the figure accordingly.

335 -As the stress (which is proportional to viscosity) is plotted against strain rate on Figure 12b (previously Figure 10a). The b-value obtained from the curve in Fig 12b is 0.5 which matched the values obtained from previous studies on crystalline dome material (Caricchi et al., 2007; Lavallée et al., 2007, 2012), therefore we feel that there is no more information to be gained by alternative plots.

345 -We thank the reviewer for highlighting this point which has spurred a number of changes (also in light of reviewer 2's comments). We now refer the reviewer to the revised Figure 12 and additional manuscript changes which have been edited to show two separate transitional regimes: viscous-dominated and brittle-dominated. Figure 12 shows clearly the evolution of failure and at which critical Deborah numbers this occurs. Figure 12c shows the standard error of estimate windows of this data and their R^2 values.

350 For a non-porous material, the data suggest the Critical Deborah number would lie between $De_c = 1 \times 10^{-4}$-6.6×10^{-4}. This is approximately two orders of magnitude lower than that reported by Webb and Dingwell (1989), which we attribute to the high crystal content as crystals also decrease this critical Deborah number (Cordonnier et al., 2012; Wadsworth et al., 2017), see also the reply to reviewer's comments on lines 535-560 of the manuscript.

For the porosity range of material tested herein, we expect the critical Deborah number to follow a linear trend as shown in
355 Figure 12c.

Response to Quane

-We thank the reviewer, Steve Quane, for his concise summary and descriptive comments which are answered below.
370

a) Deformation in experimental charges cannot be interpreted by using the rheological data alone. For example, seemingly "viscous" behavior and "brittle" behavior were interpreted (starting is section 4.1) based on the "mechanical responses" of the rocks. The authors make assumptions and "attributions" about the actual mechanical behavior of the samples with no empirical evidence. For example, they "attribute to a narrowing of pre-existing cracks" and "hypothesize may reflect a contribution of viscous deformation upon loading". It is possible that these interpretations are correct, however, it would be relatively easy to test the attributions and hypotheses by halting an experiment at the requisite place on the deformation path and doing microstructural analysis.

-We thank the reviewer for bringing this point to our attention. With reference to the high temperature viscous responses we refer the reviewer to work by Cordonnier et al., (2012), referenced in the text, who look, in detail, at the mechanical response curves of deformed samples and label them 'viscous', 'transitional' and 'brittle' according to X-ray microcomputed tomography scans of deformed samples. We particularly refer to Figures 1 and 2 in Cordonnier et al., (2012) – as such we are not defining new regimes but simply categorising our samples according to regimes already defined. With reference to the brittle experiments, we refer the reviewer to publications mentioned in the text (Hoek and Bieniawski, 1965; e.g. Brace et al., 1966; Scholz, 1968; Heap et al., 2014a) who describe, in detail, the four stages of mechanical loading and brittle failure with reference to the mechanical stress-strain curves. Although the authors agree that 'halting an experiment at the requisite place on the deformation path and doing microstructural analysis' would be a very informative study, this work has already previously been tackled, stress-strain curves have been dissected with respect to sample attributes, and for brittle experiments, the regimes of crack-closure, elastic deformation, strain hardening, and failure are well defined and identifiable by the mechanical curves. Therefore, we reassure the reviewer that care has been taken when labelling a response as 'viscous' or 'brittle' by referring to previous work in rock and lava deformation, based on their stress-strain curves.

That said, we understand the need to examine the experimental run products and have taken the reviewers concerns on board. We have illustrated our examination of the experimental products acquired by SEM imaging to create a new Figure 5, along with further descriptions and photographs of samples after deformation to Figure 12 (previously Figure 10). This analysis, based on the reviewers' comments made us revisit our labelling of samples, and we have issued a new comprehensive, visual description of failure, as seen in Figure 12. We also further concluded that the state of 'transitional' can be further sub-divided to clearly express that it is a spectrum leading from viscous behaviour, indicated from a continuous plateau in stress with substantial strain, to brittle behaviour, defined by a sharp drop in stress with little strain beyond an initial elastic loading response. Therefore, we suggest that a sample can either be in the viscous dominated regime while undergoing a transitional behaviour, where the stress plateaus with strain but there are small stress drops along the way, or the brittle dominated regime where the stress-drop is poorly defined and 'curves' before reaching high strain at failure (Figure 5; Figure 11). Although the post deformation photographs and SEM images are a useful guide, as the same strains before experiment termination/sample failure were not met by every sample (we chose our end strains based on characteristics of the stress-strain curves not on a set total strain) the results are not entirely comparable e.g. a viscous sample experiment would be terminated at much shorter strains (than a transitional sample) as its curve was already defining viscous behaviour. Thus, we consider the stress-strain curves a better method for quantitatively of defining the deformation mode of lavas.

b) Post experiment analysis of end products can lead to surprising conclusions about mechanical behavior. In these multicomponent systems, deformation can occur via several mechanisms. Bubble collapse, brittle fracturing, viscous flow of groundmass glass, microcracking, rotation of grains, grain boundary sliding, internal grain deformation. All of these are factors in accommodating strain in the samples. Hence, strain can be accommodated homogenously (throughout the sample evenly)

-We thank the reviewer for his comments and agree, understanding the complex mechanisms that led to failure in volcanic rocks is important, yet, here, this paper is not trying to decipher the deformation mechanism (e.g., viscous, plastic, brittle) but the deformation mode of lavas (i.e, ductile vs brittle) necessary to constrain (and distinguish between) flow and fragmentation processes. [Please note that the distinction between the two is that of scale: a deformation mode refers to the macroscopic character of sample deformation whereas a deformation mechanism refers to microscopic deformation processes. Thus, unfortunately in this field of laboratory testing, brittle may be used when refereeing to both a deformation mode (sample failure) and a deformation mechanism (i.e., a cracking event); see also Rutter in Tectonophysics (1986) and Heap et al. in Bull. Volc. (2015a) for clarity] We have conducted further analysis of the experimental products as described above. We also guide the reviewer to Figure 2 in Lavallee et al., (2007) where post-experiment textures have been viewed and deformation mechanisms discussed, and to Figure 2 in Kendrick et al., (2013), as well as Figure 2 in Kendrick et al., (2017), where textural evolution with strain is depicted and the deformation mechanisms are interpreted. Appreciating the need for a more in-depth explanation of the overarching deformation mechanisms in the deformation mode discussed (e.g. 'brittle' and 'viscous' and offer the reviewer the new Figure 12 (previously Figure 10) with accompanying edits in the manuscript. A detailed study of the exact microstructural deformation mechanisms at play across all samples is beyond the scope of this paper seeking to constrain deformation mode (not mechanism), and as it has already previously been discussed in other studies, we chose to highlight samples representative of each regime and map the textures associated with the different deformation regimes and link these to the stress-strain curve characteristics used to define the remaining samples.

-We advise the reviewer that samples that remained completely intact (only those with a completely 'viscous' response, i.e. those carried out at strain rates of 10^{-5} s^{-1}) were re-measured to constrain changes in connected porosity. However, the results showed no significant change in porosity, nor in the volume of the sample determined by pycnometry (Table 1); hence, we mention this in the text but do not present the data in the study. Due to minor loss of volume from the experimental process (removal of sample from pistons etc.) the pycnometer readings are within error and thus we concluded, cannot be considered.

Table 1. Example of volume measurements made using pycnometery on samples that remained intact after deformation. Fractional change in volume is $< \pm 0.05\%$ of the measured volume

Sample	Initial porosity	Strain rate tested (s^{-1})	Temperature tested (°C)	Measured volume before (cm^3)	Measured volume after (cm^3)	Fractional change in measured volume
UNZ-4-16	0.12	1.00E-05	900	12.17	12.14	0.003

| UNZ-4-17 | 0.12 | 1.00E-05 | 900 | 11.67 | 11.72 | -0.005 |
| UNZ-8-16 | 0.18 | 1.00E-05 | 900 | 11.38 | 11.32 | 0.005 |

455

d) Characterizing the amount of strain in the samples is an independent measure of machine strain. Does the sample show the same amount of strain as the machine? This can be determined through post-experiment analysis of density, porosity and core geometry. It is an important check on the experimental apparatus to ensure all strain from the machine is going into the sample. Quane and Russell, 2005 (cited by authors) and Quane et al., 2004 from American Mineralogist go through these procedures in detail.

We refer the reviewer to the first paragraph in section 2.3. of the manuscript: '[Note: all mechanical data have been corrected for the compliance of the setup, quantified via Instron procedures that monitor length changes due to loading of the pistons in contact with one another]'. This compliance method is carried out at all temperatures tested in our laboratory. Following the application of the compliance correction, the total strain referred to in the manuscript is the sample strain and not machine strain. Post-deformation sample geometry (i.e. final sample length, for the in-tact samples) was measured for the samples to confirm final strains were correct. This point has been added to the manuscript, as well as "…at the relevant experimental temperature" in the sentence describing compliance, to clarify that the different behaviour of the machine at temperature is also accounted for. To clarify, the method to quantify strain in deforming porous samples in Quane et al., (2004) and Quane and Russell (2005) may be applied for glass-bead compacts, but unfortunately not for natural multi-phase material.

Without post-experiment characterization (on samples that will allow it-sometimes even brittle deformation samples can be salvaged and epoxyed), the authors cannot speak with authority on the types of deformation occurring. Unfortunately, by not having that authority, the Conclusions they draw come into question. Certainly, the authors can do an analysis of the run products and produce a figure or two (like Figure 3 does for pre-experiment cores) to describe the major mechanisms of deformation and strain accommodation. Without this, this otherwise very strong, methodical and detailed contribution falls incomplete.

-As mentioned above, this study is first and foremost concerned with a description of the macroscopic deformation modes of lava, not the deformation mechanism. Yet, we fully agree that textural information provides insight into the underlying microscopic deformation mechanism. We draw the reviewer's attention to the newly created Figure 5 and Figure 12 a). Due to the fragmental nature of the samples, particularly those marked as having a brittle or brittle-dominated response, it was impracticable to reconstruct the position of each fragment with epoxy, yet we looked at some fragments (new Figure 5) taken from the inner part of the sample. We provide new data in Figure 10 (now Figure 12), containing photographs of the run-products and accompanying comments in the manuscript. With the photographs, the now more detailed explanation of the curves, and the SEM images in Figure 5, we believe we have satisfied the reviewers concerns about sample characterisation.

Technical corrections in this manuscript a very minimum. Found one spelling mistake, but I lost it!

-We thank the reviewer for searching the document for typos, we have found the assaulting spelling mistake mentioned and have track changed it in the manuscript.

495

List of relevant changes

The following manuscript has been edited with tracked changes to indicate what amendments have been made after reviewer's comments. Minor text edits have been made throughout the manuscript to aid with flow and to correct for typing issues, major changes include:

500
- The addition of a translated abstract from English to Japanese
- The addition of references suggested by reviewers
- The extension of our analysis of our data with comparison to the pore-emanating crack model and wing-crack model, this includes text additions to sections 1.3 and 4.1.2 and the addition of a new figure, Figure 11.
- The addition of an accessible MATALB code for the calculation of Young's Modulus, found at:
505   https://doi.org/10.5281/zenodo.1287237
- A more detailed description of the rheological response of the dome lavas, after comments by Steve Quane. This involved carrying out more SEM work, as seen in Figure 6, and the addition of text in section 3.2.2
- An updated description of the effect of pore anisotropy on rock strength, section 4.1.2, after comments by Jamie Farquharson
510
- An updated description of the failure criterion of porous lavas in section 5.2. This included the newly updated Figure 10, which is now labelled Figure 12.
- Edits were made to Figure 3, Figure, 9 (Now Figure 10), and Figure 4 for consistency
- A correction was made to the units of Equation 11 and a new reference added for clarity

515   The manuscript now includes 12 figures, 6 supplementary figures, and ~13,000 words excluding references and figure captions.

Failure criteria for porous dome rocks and lavas: a study of Mt. Unzen, Japan

Rebecca Coats[1], Jackie E. Kendrick[1], Paul A. Wallace[1], Takahiro Miwa[2], Adrian J. Hornby[1,3], James D. Ashworth[1], Takeshi Matsushima[4], Yan Lavallée[1]

[1]Department of Earth, Ocean and Ecological Sciences, The University of Liverpool, Liverpool, L69 3GP, UK

[2]National Research Institute for Earth Science and Disaster Prevention, Ibaraki, 305-0006, Japan

[3]Now at Department of Earth and Environmental Sciences, Ludwig-Maximilians-Universität München, Munich, 80333, Germany

[4]Institute of Seismology and Volcanology, Kyushu University, Nagasaki, 855 0843, Japan

Correspondence to: Rebecca Coats (r.coats@liverpool.ac.uk)

Abstract

The strength and macroscopic deformation mode (brittle vs ductile) of rocks is generally related to the porosity and pressure conditions, with occasional considerations of strain rate. At high temperature, molten rocks abide to Maxwell's viscoelasticity and their deformation mode (brittle vs ductile) is generally defined by strain rate or reciprocally, by comparing the relaxation timescale of the material (for a given condition) to the observation timescale – a dimensionless ratio known as the Deborah (*De*) number. Volcanic materials are extremely heterogeneous, with variable concentrations of crystals, glass/ melt and vesicles (of different sizes), and a complete description of the conditions leading to flow or rupture as a function of temperature, stress and strain rate (or timescale of observation) eludes us. Here, we examined the conditions which lead to the macroscopic failure for of variably vesicular ($0.0$9-$0.$35 %), crystal-rich (~ 75 vol.%), pristine and altered, dome rocks (at ambient temperature) and lavas (at 900 °C) from Mt. Unzen Volcano, Japan. We found that the strength of the dome rocks decreases with porosity and is commonly independent of strain rate; when comparing pristine and altered rocks, we found that the precipitation of secondary mineral phases in the original pore space alteration caused minor strengthening. The strength of the lavas (at 900 °C) also decreases with porosity. Importantly, the results demonstrate that these dome rocks are weaker at ambient temperatures than when heated and deformed at 900 °C (for a given strain rate resulting in brittle behaviour). Thermal stressing (by heating and cooling a rock up to 900 °C at a rate of 4 °C min^{-1}, before testing its strength at ambient temperature) was found not to affect the strength of rocks.

In the magmatic state (900 °C), the rheology of the dome lavas is strongly strain rate dependent. Under low experimental strain rate conditions ($\leq 10^{-4}$ s^{-1}) ductile deformation dominated the lavas behaved ductilly (i.e., the material sustained substantial, pervasive deformation) and displayed a non–Newtonian, shear thinning behaviour. In this regime, the apparent viscosities of the dome lavas were found to be essentially equivalent, independent of vesicularity, likely due to the lack of pore pressurisation and efficient pore collapse during shear. At high experimental strain rates ($\geq 10^{-4}$ s^{-1}) the lavas displayed an increasingly brittle response (i.e., deformation resulted in failure along localised faults); we observed an increase in strength and a decrease in strain–to–failure as a function of strain rate. To constrain the conditions leading to failure of the lavas, we analysed and compared the critical Deborah number at failure (De_c, the ratio between the relaxation time and the experimental observation time) of these lavas to that of pure melt ($De_{melt}=10^{-3}$–10^{-2}; Webb & Dingwell, 1990). We found that the presence of crystals decreases De_c to between 6.6×10^{-4}–$2.1$$1\times10^{-4}$. The vesicularity ($\varphi$), which dictates the strength of lavas, further controls De_c following a linear trend $5.1\times10^{-4}\varphi+2.11\times10^{-4}$. We discuss the implications of these findings for the case of magma ascent and lava dome structural stability.

多孔質な岩石及び溶岩の破壊基準：雲仙火山溶岩ドームでの研究

マグマ(溶岩)と岩石のレオロジーと強度は，応力の蓄積と散逸を支配し，噴火様式や山体の構造的安定性に影響を与える．火山噴出物は極端に不均質であり，様々な量・サイズの結晶，ガラス(メルト),気泡を含む．そのため，温度・応力・歪速度の関数として，その流れや亀裂形成を引き起こす状態を完全に記載することは難しい．ここで我々は，雲仙火山において溶岩ドームを形成し様々な発泡度(9-35%)を有する高結晶度(〜75%)な岩石(常温)と溶岩(900度)について，その破壊を引き起こす状態を検討した．その結果，我々は岩石の強度は空隙率とともに減少し，歪速度に依存しないことを発見した： 新鮮な岩石と変質したものでは，後者でわずかに強度が大きい．また，溶岩(900℃)の強度も空隙率とともに減少する．この結果は重要なことに，脆性的振る舞いを起こす歪速度において，常温における岩石の強度は，それを900℃まで加熱し変形させたときの強度よりも弱いことを示している．このとき，熱応力は岩石の強度に影響を与えない．

高温条件(900℃)では，溶岩のレオロジーは歪速度に強く依存する．低歪速度下($<10^{-4}$ s^{-1})では，溶岩は塑性的に振る舞い(物質が広範な固体変形を持続させる)，非ニュートン流体としてずり粘減の振る舞いを示した．このレジームでは，溶岩の見かけ粘性は，おそらく剪断時の効率的な空隙崩壊のため，発泡度に依存しない．高歪速度下($>10^{-4}$ s^{-1})では，溶岩は益々の脆性的な応答(局所的な断層に沿った破壊による変形)を示す；歪速度の関数として，強度の増加と破壊へ至るときの歪の減少が観察された．溶岩の破壊を引き起こす状態を制約するため，これら溶岩における破壊時の臨界デボラ数(De_c,緩和時間と実験観察時間の比)を解析し，メルトにおけるそれ($De_{melt,} = 10^{-3}$-10^{-2}; Webb & Dingwell, 1990)と比較した．我々は結晶の存在がDecを$6.6×10^{-4}$–$1×10^{-4}$まで減少させることを発見した．またさらに，溶岩の強度に影響する発泡度(φ)もDe_cを線形傾向のようにコントロールする．我々はこれらの発見が与える，マグマ上昇と溶岩ドームの構造的安定性への示唆を議論する．

1 Introduction

1.1 Lava dome eruptions

Magma ascends to the Earth's surface and erupts through a wide spectrum of eruptive style (e.g. Siebert et al., 2015), which contributes to the construction of different volcanic edifices (e.g. de Silva and Lindsay, 2015). Amongst this activity, lava domes form when viscous magma accumulates and creates mounds of rocks and lava above the vent (Sparks, 1997; Fink and Anderson, 2000). These dome–building events make up approximately 6 % of volcanic eruptions worldwide (Calder et al. 2015) and their characteristics are governed by the rheology of the erupted magmas (Gonnermann and Manga, 2007; Lavallée et al., 2007). The emplacement of lava domes may be endogenous or exogenous, whether growing through inflation from within, or through the piling up of discrete extrusive bodies (Hale and Wadge, 2008). In some extreme cases the latter can manifest as lava spines that~~,~~ extrude in a near–solid state (Angelo Heilprin, 1903; Stasiuk and Jaupart, 1997; Young et al., 1998; Tanguy, 2004; Scott et al., 2008; Vallance et al., 2008; Kendrick et al., 2012; Cashman and Sparks, 2013). Dome eruptions can produce a range of primary hazards, from ash fall to large–scale pyroclastic density currents, generated by gravitational collapse (e.g. Sparks and Young, 2002). They also have the potential to generate secondary hazards such as lahars (e.g. Nevado del Ruiz, Colombia; Pierson et al. 1990); edifice failure induced by magma intrusions (Voight and Elsworth, 1997; Reid et al., 2010), and lava dome collapse, as the mass cools or redistributes (e.g. Elsworth and Voight, 1996). In seismically active areas, strong tectonic earthquakes can both initiate activity and promote structural instability (e.g. Mayu–yama, Japan; Siebert et al. 1987), even in long–dormant systems (e.g. Merapi, Indonesia; Surono et al. 2012). T~~hus, t~~he eruption, emplacement and stability of lava domes reflects the mechanical properties of the~~ir~~ constituent materials ~~they consist of~~. ~~,thus,~~ ~~It~~ it is ~~therefore~~ essential that the evaluation of monitoring data and development of improved hazard forecasting tools at lava dome volcanoes ~~to the continued monitoring effort of lava domes that the modelling and evaluation of their state~~ be based on a description of the mechanical and rheological properties of the materials. ~~for the development of improved forecasting tools.~~

1.2 Lava dome rheology

The rheology of silicate melts has been explored extensively (e.g. Dingwell and Webb, 1989, 1990; Webb and Dingwell, 1990; Webb and Knoche, 1996; Fluegel, 2007; Giordano et al., 2008; Cordonnier et al., 2012b). Dingwell and Webb (1989) demonstrated that silicate liquids are viscoelastic bodies, that abide to the glass transition– a temperature–time space that defines their structural relaxation according to the theory of viscoelasticity of Maxwell (1867). Maxwell's work established that the structural relaxation time–scale τ equals the ratio between the melt viscosity η_m (in Pa.s) and its elastic modulus at infinite frequency G_∞ (in Pa) according to:

$$\tau = \eta_m / G_\infty$$ (1).

Dingwell and Webb (1989) compiled information for different silicate liquids and showed that G_∞ is essentially invariant and approximately $10^{10\pm0.5}$ Pa in the temperature range of interest for magmatic systems. Thus, the relaxation time–scale of silicate melts can simply be related to their viscosity at a given temperature. Extensive experimental efforts in the community have resulted in the creation of a complete, non–Arrhenian model for silicate melt viscosity, as a function of composition and temperature (e.g. Giordano et al., 2008). The concept of viscoelasticity and relaxation timescale can therefore be applied to a range of volcanic processes.

Viscoelasticity dictates the behaviour of a magma. A rheological description of viscoelastic materials may be cast via the non–dimensional Deborah number, *De* (e.g. Reiner 1964), which is defined by a ratio between Maxwell's relaxation time–scale, τ (Eq. 1) and the time–scale of observation, t_{obs}:

$$De = \frac{\tau}{t_{obs}},$$ (2)

This relationship states that under observation timescales longer than the relaxation timescale (for a given melt viscosity), a melt may flow like a liquid; but at short observation timescales, a melt may behave as a solid (like a glass). In such a kinetic framework, increasing the temperature reduces the viscosity and therefore the time required for structural relaxation. As the relaxation time–scale is inversely proportional to the structural relaxation rate, it can thus be said that the structural relaxation rate defines the transition between the liquid and solid states (commonly referred to as the glass transition, T_g). Dingwell and Webb (1990) demonstrated that at $De < 10^{-3}$, a silicate melt can be described as a Newtonian fluid. However, when silicate melts are deformed at higher rates where the observation time–scale is short, $10^{-3} < De < 10^{-2}$, the melt structure accumulates damage upon deformation which results in an apparent non–Newtonian behaviour. At $De > 10^{-2}$, silicate melts undergo the glass transition and ruptures (Dingwell and Webb, 1990; Wadsworth et al., 2017); this is known as the critical Deborah number, De_c – a criteria met in several eruptive scenarios, including fragmentation and explosive eruptions (e.g. Dingwell, 1996).

During transport and eruption, magmas crystallise and volatiles are exsolved (e.g. Cashman, 1992; Martel and Schmidt, 2003), resulting in magmatic suspensions, undergoing significant rheological changes (e.g. Lejeune and Richet, 1995; Barmin et al., 2002). In particular, dome–building eruptions have been observed to produce variably vesicular (generally ≲ 0.40 %) and crystalline (e.g. 0–100 vol.%) lavas (Castro et al., 2005; Mueller et al., 2005, 2011a; Lavallée et al., 2007; Pallister et al., 2008; Cordonnier et al., 2009; Calder et al., 2015; Heap et al., 2016a). The addition of crystals to a melt increases the effective viscosity (Lejeune and Richet, 1995). At moderate crystal fraction (below ~ 25 vol.%) this can be approximated by the Einstein–Roscoe equation (Einstein, 1911; Roscoe, 1952), and variations thereof (see Mader et al., 2013 and references therein). When particle concentrations reach a critical fraction that promotes interaction (typically ≤ 0.25, depending on crystal morphology (Mader et al., 2013)), the suspension becomes non–Newtonian (Deubelbeiss et al., 2011). Experiments on dome lavas at high temperature have shown that the apparent viscosity of these suspensions decreases with strain rate (Lavallée et al., 2007; Avard and Whittington, 2012) – a shear thinning effect influenced by crystal alignment and interaction (Vona et al., 2011); crystal plasticity (Kendrick et al. 2017), and fracture processes (Lavallée et al., 2008; Kendrick et al., 2013b). The addition of a separate gas phase to a magma adds further rheological complexity (Lejeune et al., 1999), serving to increase or decrease viscosity depending upon the volume fraction of bubbles, pore pressure, the initial viscosity of the melt, and the amount of deformation they are subjected to (e.g. Manga et al., 1998; Llewellin and Manga, 2005), and pore connectivity, which may promote outgassing and pore compaction (e.g. Ashwell and Kendrick et al., 2015). Bubbles will affect the viscosity of the suspension depending on their capillary number, Ca, a dimensionless ratio of the deforming viscous stress over the restoring stress from surface tension. A more spherical bubble will generally have a low Ca, as restoring stresses dominate, and will behave as a barrier which fluid flow will have to deviate around resulting in an increased viscosity of the suspension. On the other hand, an elongate bubble generally has a high Ca, as deforming stresses dominate, and may act as free slip surface causing a decrease in the suspension viscosity (e.g. Manga et al., 1998; Mader et al., 2013). Three–phase models, although less explored than two–phase flows, have been modelled by Truby et al. (2015) by combining two sets of two–phase equations. Despite the aforementioned rheological studies focused on the viscosity of magmatic suspensions, the conditions leading to failure of such magmatic suspensions have received less attention. Following the work of Lavallée et al. (2007), Gottsmann et al. (2009) showed that the presence of crystals may reduce the strain rate required to rupture magma (if one was to consider the melt relaxation rate) to conditions where $De < 10^{-2}$ and Lavallée et al. (2008) and Gottsmann et al. (2009) showed that brittle processes may be active at conditions two orders of magnitude lower than such a purely brittle limit. Cordonnier et al. (2012a) explored the effect of crystallinity on magma rupture, showing that *De* indeed decreases with crystallinity. However,

18

here we note that when determining the Deborah number for their experimental findings, the relaxation time–scale was calculated using the apparent viscosity of the suspension rather than the viscosity of the interstitial melt, which is the basis for the applicability of viscoelasticity in this scenario (this will be discussed further in section 5.2). Important questions remain as to the contribution of vesicles on the rupture of magmas, as the strength of geomaterials in the brittle field is generally described in terms of porosity (e.g. Paterson and Wong, 2005, and references in section 1.3).

1.3 Lava dome mechanics

Various numerical models have been developed to evaluate the structural stability of lava domes and, with sufficient knowledge of a volcanic edifice and the properties of the materials it holds, collapse events can be modelled effectively (e.g. Elsworth and Voight, 1996). Although elegant and complex, these simulations tend to make non–trivial assumptions regarding vent geometry, dome morphology, and material properties (e.g. Ball et al., 2015). Volcanic domes are composed of materials with a vast spectrum of heterogeneities and degree of coherence (Mueller et al., 2011b; Lavallée et al., 2012, 2018) and although assigning fixed values for the material properties of dome rocks may be computationally beneficial, accounting for the wide range of physical and mechanical properties of dome materials remain a great source of uncertainty. Mechanical testing can be carried out to resolve the behaviour of rocks (see Paterson and Wong, 2005 and references therein) and this has resulted in a recent surge in laboratory testing to advance the understanding of the tensile strength, compressive strength, frictional coefficient and flow behaviour of these heterogeneous dome rocks and magmas as a function of temperature and stresses or strain rates (Smith et al., 2007, 2011; Lavallée et al., 2007; Hess et al., 2008; Kendrick et al., 2012, 2013b, 2013a; Kolzenburg et al., 2012; Heap et al., 2014a; Hornby et al., 2015; Lamb et al., 2017; Lamur et al., 2017 and more.)

The uniaxial compressive strength of volcanic rocks has been found to inversely correlate with porosity (Al-Harthi et al., 1999; Kendrick et al., 2013b; Heap et al., 2014a, 2014b, 2016b; Schaefer et al., 2015), and to positively correlate with strain rate (Schaefer et al., 2015). In volcanic rocks, porosity is made up of vesicles and micro–fractures, which contribute to the mechanical behaviour and strength of the rock (Sammis and Ashby, 1986; Ashby and Sammis, 1990; Heap et al., 2014a; Bubeck et al., 2017; Collombet et al., 2017; Griffiths et al., 2017). Two models have gained traction to explain the strength of rocks. The pore–emanating crack model of Sammis and Ashby (1986), describes the case of a pore–only system where cracks nucleate from the pores and propagate in the direction parallel to the principal stress, when the applied stress overcomes the fracture toughness of a rock. As the applied stress increases, the micro–fractures propagate and coalesce, leading to macroscopic failure. An analytical estimation of this model was derived by Zhu et al., (2010) to estimate the uniaxial compressive stress (σ) of a sample, with a pore radius (r), as a function of its porosity (φ) and the fracture toughness (K_{IC}):

$$\sigma = \frac{1.325}{\varphi^{0.414}} \frac{K_{IC}}{\sqrt{\pi r}} \tag{2}$$

In contrast, the sliding wing–crack model of Ashby and Sammis (1990) considers only pre–existing micro–fractures inclined from the principal stress direction. The model describes that first, the frictional resistance of the crack must be overcome before wing–cracks can form, then the fracture toughness must be overcome for them to propagate and interact. The analytical approximation for this model was developed by Baud et al., (2014):

$$\sigma = \frac{1.346}{\sqrt{1+\mu^2}-\mu} \frac{K_{IC}}{\sqrt{\pi c}} D_0^{-0.256} \tag{3}$$

where μ is the friction coefficient of the crack, c is the half–length of a pre–existing crack, and D_0 is an initial damage parameter (which takes into consideration the number of cracks per unit area and their angle with respect to the principal stress).

Heap et al., (2014a) experimentally demonstrated that neither model fully satisfied the mechanical data obtained for volcanic rocks and suggested that a microstructural model that combines the two mechanisms must be ~~considered~~ developed to permit

19

the design of simulations considering the mechanical behaviour of ~~when studying volcanic rocks, due to their~~ microstructurally complex~~ity~~ volcanic materials.

The problem of lava dome stability does not simply require knowledge of hot lavas or cold rocks; it further requires understanding of the effects of temperature (e.g. Harris et al., 2002); chemical alteration (e.g.~~,~~ Lopez & Williams 1993; Ball et al. 2015); pore pressure (Farquharson et al., 2016), thermal stressing (Heap et al., 2009, 2010, 2014a; Kendrick et al., 2013a; Schaefer et al., 2015) and mechanical stressing at different rates such as during seismic shaking (Cole et al., 1998; e.g. Voight, 2000; Calder et al., 2002) or magmatic intrusions (Walter et al., 2005) on the mechanical properties of the materials, many aspects of which have been tested in the context of edifices. The cooling of crystalline lava bodies results in the generation of fractures (Fink and Anderson, 2000; Takarada et al., 2013; Eggertsson et al., 2018) – leaving a highly fractured, blocky mass, the mechanical impact of which is difficult to quantify (Voight, 2000; Voight and Elsworth, 2000). Furthermore, thermal stressing cycles that could result from proximity of hot magma in a conduit, lava dome or edifice following a new eruptive episode, have been found to only weakly modify the strength of commonly micro-–fractured volcanic rocks (Heap et al. 2009; Kendrick et al. 2013; Schaefer et al. 2015,), unless they contain thermally liable minerals (Heap et al., 2012, 2013a, 2013b). Recent experiments on porous basalt by Eggertsson et al. (2018) ~~(in review)~~ have shown that rocks that are essentially void of micro-–cracks (likely due to slow cooling), are however susceptible to fracture damage by thermal stressing (i.e., forming cooling joints); in contrast, micro-fractured rocks, may not necessarily accumulate more damage during cooling, yet upon contraction, pre-existing fracture may widen to give way to the ingression of hydrothermal fluids (e.g. Lamur et al., 2018), further contributing to the stress balance and mechanical response.

1.4 Mt. Unzen lava dome

The Unzendake volcanic complex is situated on the Shimabara peninsula in South–Western Japan (Fig. 1a). The volcanic complex began to grow 0.5 Ma ago and now covers 20 km (E–W) by 25 km (N–S) (Takarada et al., 2013). Unzendake exhibits an intricate eruptive history of lava domes, flows and pyroclastic deposits (Nakada and Fujii, 1993) of predominantly dacitic composition (Nakada and Motomura, 1999).

On 17 November 1990, after 198 years of quiescence, a phreatic eruption occurred at Mt. Unzen, which was accompanied by multiple earthquake swarms, ~~after 198 years of quiescence~~ (Matsushima and Takagi, 2000). This was followed shortly afterwards by a phreatomagmatic eruption along with intense edifice swelling, and on 20 May 1991, the extrusion of a lava spine initiated the growth of the Heisei–Shinzan dome complex (Nakada and Fujii, 1993; Takarada et al., 2013). This introduced a 45-–month long period of lava dome activity with growth being primarily exogenous in periods of high extrusion rate, and endogenous in times of low effusion rate (Nakada et al., 1995b, 1999a). The final stage of growth was marked by the extrusion of a spine between October 1994 and February 1995 (which can be seen this present day; Fig. 1b~~1~~-c), characterised by pulsatory ascent and seismicity (Umakoshi et al., 2008; Lamb et al., 2015), along fault zones defined by compactional shear (Ashworth et al.*, in prep*) and mineral reactions, crystal plasticity and comminution (Wallace et al., ~~submitted~~*in review*). The end of the eruption was followed by cooling of the lava dome and thermal contraction that caused multiple joints (Takarada et al., 2013). Fumarole activity has continued to the present day, with temperatures decreasing from 300 °C in mid–2007 to 90 °C in 2011 (Takarada et al., 2013).

In total, 13 lava lobes were formed, and, at its maximum size, the lava dome was 1.2 km (E–W) by 0.8 km (N–S) wide. In particular lobe 11, which dominated the Eastern side of the complex (Nakada et al., 1995a, 1999b) has long been unstable, which has led to partial collapses that generated several pyroclastic density currents (PDCs; Nakada et al., 1999a; Sakuma et al., 2008). The flows were estimated to have travelled at 200 km hr^{-1}, up to 5.5 km down the Oshigadani Valley (Yamamoto et al., 1993; Takarada et al., 2013). All in all, pyroclastic flows buried and/or burned approximately 800 buildings, ~~and~~ with debris flows ~~destroyed~~ destroying a further ~ 1,700, and in the summer of 1991 the number of evacuated persons exceeded 11,000 (Nakada et al., 1999a). The Committee of Survey and Countermeasure on Lava Dome Collapse at Mt. Unzen advises

that the risk of collapse of lobe 11 is high, an exclusion zone remains active to the E of the summit and access to the lava dome is strictly limited. Data from electro–optical distance measuring instruments suggest that ~~the~~ lobe 11 has ~~moved~~ advanced 1 m in 14 years (measurements from 1997–2011), and recent observations from ground-based synthetic aperture radar show the development of a shear fracture (Kohashi et al., 2012). Therefore, the complete or partial collapse of the lobe and the generation of block–and–ash flows are likely hazards, ~~a block and ash flow is likely~~, particularly after large regional earthquakes. The current uncertainty regarding the structural~~of~~ stability of the dome at Mt. Unzen, particularly after seismic activity, has led to recent field campaigns and mechanical studies of the dome material (e.g. Cordonnier et al., 2009; Hornby et al., 2015). The destabilisation ~~Movement~~ of lava domes due to ~~such~~ tectonic activity is essentially a superficial process, meaning the ~~issue canstress~~ balance may be considered as a uniaxial problem, and tested as such (e.g. Quane and Russell, 2005).

2 Materials and methods

2.1 Sample selection

Mt. Unzen lava dome is made up of porphyritic, dacite (~ 63 wt.% SiO_2) lava blocks which typically have large (> 3 mm) and abundant (> 25 vol.%) plagioclase phenocrysts, along with lesser amounts of amphibole (~ 5 vol.%), biotite (~ 2 vol.%) and quartz (~ 2 vol.%) phenocrysts and microphenocrysts set in a partially crystalline (~ 50 vol.%) groundmass of plagioclase, pyroxene, quartz pargasite, and Fe–Ti oxides in a rhyolitic interstitial glass (Nakada & Motomura 1999; Wallace et al. *in review*). However, as the dome was formed through both, exogenous and endogenous growth, the petrological history of the eruptive products varies widely and as such the ~~both exogenously and endogenously the~~ microstructure of the~~se~~ blocks forming the dome varies considerably. Furthermore, lasting heat sources and ongoing fumarolic activity have led to local thermal and hydrothermal alteration of the dome (Almberg et al., 2008). This heterogeneity calls for a variable sample suite to represent the dome material, and to constrain the processes of deformation and cooling that occurred throughout lava dome formation, that influences its current structural stability.

In this study, 9 samples were selected with different properties. Samples UNZ-1, 2, 4, 5, 7, and 8 were collected from easily accessible, June 1993 block–and–ash flow deposits in the Minami–Senbongi area, north–east of the spine; UNZ-13 was collected from the May-August 1991 deposits in the restricted area of the Mizunashi River, east of the spine (see Fig. 1b). These rocks were collected as they represent the freshest (unaltered) materials that originate from dome collapse events during eruption, prior to any chemical alteration (e.g.~~,~~ Cordonnier et al., 2008). Sample UNZ-11 was collected on lobe 11 of the dome, selected as it showed signs of hydrothermal alteration (crusted, white and friable). UNZ-12 was collected on the dome, just east of the lava spine, and was chosen specifically for its reddish colour which suggested thermal alteration and oxidation. Each sample block was then cored to make multiple 20 mm diameter cylindrical cores, cut, and then ground parallel to 40 mm in length (Fig. S1) to maintain a 2:1 aspect ratio in accordance with the ISRM suggested method (ISRM Turkish National Group, 1979)~~(IRSM Turkish National Group, 1979)~~.

2.2 Sample characterisation and preparation

2.2.1 Geochemistry

The bulk geochemical compositions of selected samples were determined in a PANalytical Axios Advanced X–Ray Fluorescence Spectrometer (XRF) at the University of Leicester (using fused glass beads prepared from ignited powders). Sample to flux ratio was kept at 1:5, 80 % Li metaborate: 20 % Li tetraborate flux. Results are quoted as component oxide weight percent and re–calculated to include LOI (loss–on–ignition).

The geochemical composition of the interstitial glass in sample block UNZ-4 was determined using a Cameca SX–5 Field Emission Electron Probe Microanalyser (EPMA) at the University of Oxford. A variety of standards were used to calibrate the spectrometers, including Wollastonite for Ca, and Albite for Al, Na and Si. Secondary reference standards, of which the exact chemistry was known, were utilised for better precision and accuracy. These were Labradorite and kn18 glass (comendite obsidian, Kenya), used as the chemistries were similar to those of the Mt. Unzen glass sample. Analyses used an accelerating voltage of 15 KeV, a beam current of 6 nA and a defocussed spot size of 10 μm. The data were checked for major element oxides' totals.

The bulk geochemical compositions of selected samples were determined in a PANalytical Axios Advanced X–Ray Fluorescence Spectrometer (XRF) at the University of Leicester (using fused glass beads prepared from ignited powders). Sample to flux ratio was kept at 1:5, 80 % Li metaborate: 20 % Li tetraborate flux. Results are quoted as component oxide weight percent and re–calculated to include LOI (loss–on–ignition).

2.2.2 Porosity

The porosity and character of the pores (i.e., whether connected or isolated) was assessed using an AccuPyc 1340 helium pycnometer from Micromeritics. Firstly, height (h; in m), radius (r; in m) and mass (m; in kg) were recorded for each cylindrical core sample, providing a constraint on sample density (ρ_s; in kg/m^3):

$$\rho_s = {m}/{\pi r^2 h} \tag{34}$$

Secondly, the solid density of the rocks (ρ_0) was constrained by measuring the mass and volume of a powdered lump from each rock in a pycnometer; from these measurements, the total porosity of each rock could be estimated via:

$$\varphi_T = 1 - ({\rho_s}/{\rho_0}) \tag{45}$$

To constrain the fraction of isolated pores in the rocks, the skeletal volume ($V_{skeletal}$; in m^3) of each core was measured in the pycnometer. The porosity connected to the outside of the sample (henceforth termed connected porosity), φ_O, could then be calculated via:

$$\varphi_O = 1 - ({V_{skeletal}}/{\pi r^2 h}) \tag{56}$$

and isolated porosity, φ_i, via:

$$\varphi_i = \varphi_T - \varphi_O \tag{67}$$

The porosity determination was used to omit outliers from any sample block to ensure that the rocks of a given porosity were tested and compared to one another.

2.2.3 Microstructures

Thin sections of UNZ- 4,11,12 and 13 were prepared with a fluorescent dyed epoxy; selected as they cover a vast range of sample diversity; including both the lower and upper bounds of porosity, and collection site. Images were acquired using a DM2500P Leica microscope in plane–polarised light. To further constrain the microstructures of each sample block, backscattered electron (BSE) images were taken of each sample using a Philips XL30 tungsten filament scanning electron microscope (SEM), equipped with an energy–dispersive X–ray spectrometer (EDS), and a Hitachi TM3000 SEM at the University of Liverpool. Stubs of the samples were set in epoxy, polished and carbon coated, before being imaged in the Philips

XL30 at a working distance of 13±0.1 mm using a 20 kV beam voltage, a 60–90 μA beam current and a spot size of 5. Thin sections of the samples were imaged with the Hitachi TM3000 using a 15 kV beam and 10 mm working distance.

2.2.4 Thermal Analysis

To constrain the conditions at which to carry out the high temperature uniaxial tests, we evaluated the softening point of the Mt. Unzen dome rock using a Netzsch 402 F1 Hyperion thermomechanical analysis (TMA) at the University of Liverpool. Under a 20 mL.min^{-1} argon flow, a 6.37 mm tall, 5.87 mm wide, cylindrical sample of UNZ-8 was placed under a constant load of 3 N and heated at 10 ˚C/min to 1100 ˚C. The softening point of the material was found as the temperature at which the applied load counteracts sample expansion by inducing viscous flow (and sample shortening) during heating. This was detected at 824.6 °C, 80.6 minutes into the measurement (Fig. S5). An experimental temperature of 900 °C was selected as, being well above the softening point, this is high enough to allow for flow to occur on the timescales under investigation. This chosen temperature is close to the magmatic temperature (850–870 °C) constrained to have followed mixing (Venezky and Rutherford, 1999) and above the glass transition of Unzen spine material (790 °C) measured by differential scanning calorimetry at a rate of 10 °C.min^{-1} (Wallace et al. *in review*), though the temperature profile within the conduit and dome during emplacement is poorly constrained.

2.2.5 Thermal stressing

Selected cores of pristine material were thermally stressed in a Carbolite box furnace to examine the effects of experimentally induced heating–cooling cycles on the residual strength of rock cores. Cores were subjected to heating at 4 °C min^{-1} followed by 1–hr dwell at 900±3 °C (sample temperature) and cooling at 4 °C min^{-1}. The density and porosity of each sample were measured before and after thermal stressing, and the products were further subjected to uniaxial compressive strength tests.

2.3 Uniaxial compression experiments

Uniaxial compressive strength tests were carried out using a 50 kN 5969 Instron benchtop press and a 100 kN Instron 8862 uniaxial press with a three–zone, split cylinder furnace using the parallel plate method in the Experimental Volcanology and Geothermal Research Laboratory at the University of Liverpool (Fig. 2). Experiments were carried out both at ambient temperature (~20 °C) and at high temperature (900 °C, using a heating rate of 4 °C min^{-1}). Tests were conducted at constant strain rates of 10^{-1}, 10^{-3} or 10^{-5} s^{-1} (see Table 1 for the range of experimental conditions). The apparatus monitored the applied load and piston extension at 10–1000 Hz (depending on set experiment rate) and the Bluehill® 3 software was used to compute data and calculate strain (ε) and compressive stress from the input sample dimensions. [Note: all mechanical data have been corrected for the compliance of the setup at the relevant experimental temperature, quantified via Instron procedures that monitor length changes due to loading of the pistons in contact with one another]. The end of each experiment was defined by either (1) in the case of viscous flow, when there was a constant stress recorded for a significant amount of time (>1 hour), or (2) in the case of brittle behaviour, a stress drop exceeding 20 % of the monitored peak stress achieved, highlighting that failure had occurred. Repeat experiments were performed on samples with a similar porosity (i.e., within 0.01 % of the other sample tested) at various conditions to verify findings.

2.3.1 High temperature experiments

Prepared cores were placed upright in between the pistons of the press; the furnace was closed around the sample which was heated at 4 °C min^{-1} to 900±3 °C (sample temperature); a K–type thermocouple was left in contact with the sample at all times and the temperatures of the top, middle and bottom zones of the furnace were monitored throughout the experiment. Following

thermal equilibration for 1 hour at target temperature, the piston was then brought into contact with the sample at low load (< 30 N), and the temperature of the sample was read from the thermocouple. A stepped strain–rate experiment (at 10^{-6} then 10^{-5}, 10^{-4} and 10^{-3} s^{-1}) was first carried out to constrain the viscous–brittle transition of the material and inform subsequent testing at unique strain rates. Tests at unique strain rates were then carried out at 10^{-3}, 10^{-4}, 10^{-5} s^{-1}, after which, the samples were cooled to ambient temperature at 4 °C min^{-1} [note: From here, samples deformed at high temperature will be defined as lavas, and those tested at room temperature as rocks].

2.3.2 Ambient temperature experiments

Ambient temperature experiments were carried out on all collected sample blocks. Prepared cores were placed upright between the pistons where they underwent compressive tests at various strain rates until failure. The thermally stressed samples were tested at a strain rate of 10^{-3} s^{-1}, whereas the remaining pristine specimens were axially loaded at strain rates of 10^{-1}, 10^{-3}, or 10^{-5} s^{-1} until failure (see Table 1).

2.3.3 Treatment of data

The strain at failure for these samples was selected using a semi–automated MATLAB script which identified the strain value at peak stress. The static Young's Mmodulus was calculated computed for each experiment that exhibited a brittle response (e.g. after Heap et al. 2014a) by calculating the slope of the linear portion of the as the linear slope of the stress–strain curve via an automated script written in MATLAB and available at https://doi.org/10.5281/zenodo.1287237. To ensure that only the linear portion was selected, points within 10 % of the maximum slope were considered to define the Young's modulus for that sample (Fig. S6), minimising the potential contribution of mechanical data obtained during crack closure (during initial loading) and during strain hardening (beyond the onset of dilation).

For samples that demonstrated a viscous response, the apparent viscosity (η_a; in Pa.s) was calculated using the equation of Gents' (1960) equation developed for the parallel–plate viscometric method, given the absence of slip along the sample/piston interfaces:

$$\eta_a = \frac{2\pi F h^4}{3V\dot{\varepsilon}(V+2\pi h^3)},$$ (78),

where F (N) is the applied force on the sample; h (m) is the height of the sample; V (m^3) is the initial volume of the sample, assumed constant, and $\dot{\varepsilon}$ (s^{-1}) is the applied strain rate.

3. Results

3.1 Sample characterisation

3.21.1 Mineralogy and geochemistry

Normalised geochemical analysis for bulk and glass geochemistry, obtained by XRF and EPMA respectively, are displayed in Table 2. Optical examination of the samples reveals that they consist of 20–50 vol.% phenocrysts and microphenocrysts of plagioclase (> 25 vol.%), amphibole (~ 5 vol.%), biotite (~ 2 vol.%) and quartz (~ 2 vol.%) (Fig. 3), where plagioclase and amphibole are the largest of the phenocrysts, and are generally greater than 3 mm. These phenocrysts and microphenocrysts are set in a partially crystalline (~ 50 vol.%) groundmass containing microlites of plagioclase, pyroxene, quartz, pargasite, and Fe–Ti oxides in a peraluminous rhyolitic interstitial glass (as described in Cordonnier et al. 2009). Cristobalite is occasionally observed as pore infills (also recorded by Nakada and Motomura, 1999). The bulk chemistries of samples UNZ-11 and UNZ-

12 (deemed visually altered) have slightly more (1.1–1.4 wt.%) SiO_2 and slightly less (0.55–0.63 wt.%) CaO than UNZ-4, whilst K$_2$O and Na$_2$O ~~potassium and sodium~~ concentrations are almost identical.

3.~~2~~1.2 Rock porosities

The total porosities of the samples determined by helium pycnometry measurements range from 0.10–0.32 (Table 3); a scatter which has previously been studied in an investigation of rock frictional properties (Hornby et al., 2015) and which is consistent with field measurements of Mt. Unzen 1991-1995 eruptive ~~dome~~ products (Kueppers et al., 2005). The pores of the denser products, notably UNZ-4 and UNZ-12, are fully connected, whereas the higher porosity blocks contain a portion (0.01–0.02) of isolated pores. The small standard deviation for the connected, isolated and thus total porosity of the rocks ensures the comparability of mechanical data obtained on samples with similar porosities during repeats.

3.~~2~~1.3 Microstructures

Microstructural examination can be used to assess any pre–existing anisotropy or fabrics in the lavas. Photomicrographs along with SEM images, of a selected group of samples (UNZ-4,-11,-12,-13) can be seen in Figure 3. These samples are shown due to their contrasting nature, covering the span of textures studied here: UNZ-11 and UNZ-12 are visually altered samples; UNZ-13 has a different pore anisotropy than UNZ-11, and UNZ-4 is a typical product of the block–and–ash flow and is representative of the remaining samples tested. The images in Figure 3 show the original materials, orientated so that the direction of principal stress, σ_1, applied to the cores prepared of each rock would be in the vertical direction.

It is evident from Figure 3 that the pores in the Mt. Unzen dome rock samples are preferentially elongate. In some cases, the elongation has a visually preferred orientation (e.g. UNZ-11,-13), while in others it is unsystematic (e.g. UNZ-4,-12). In UNZ-11 vesicles, and microlites, appear to bottleneck around phenocrysts in a horizontal direction (i.e., perpendicular to σ_1 imposed in the experiments), whereas in UNZ-13 their alignment is vertical (i.e., parallel to σ_1), indicating a sense of shear in those directions. UNZ-4,-11, and -13 have significant number of larger pores (>1 mm) when compared to UNZ-12, and across the shown sample set, these larger pores appear as pressure shadows around the phenocrysts (e.g. see McKenzie and Holness, 2000). Fractures are only clearly visible in UNZ-4, this is most likely due to higher abundance and larger fracture widths in this sample, allowing them to be visible in both thin section and BSE images. The fractures appear to connect pores via the tip of their major axis.

The groundmass of UNZ-12 contains a scaly–textured silica~~quartz~~ polymorph that appears to have filled vesicles. Common silica~~quartz~~ polymorphs seen at Mt. Unzen, and other domes across the world (e.g. Mt. St. Helens; Voight et al. 1981), are cristobalite precipitates, formed from hydrothermal activity (Nakada and Motomura, 1999; Voight et al., 1981, 2009; Yilmaz et al., *in review*). This silica deposit has filled a considerable amount (~ 50 vol.%) of the vesicles in UNZ-12, reducing its porosity (Fig. 3c). Although the polymorph is a sign of alteration, in the highest magnification BSE image, some glass appears to have remained vitreous between ~~quartz~~ silica polymorph areas. ~~Similarly, i~~In UNZ-11, neither the phenocrysts nor the groundmass show evidence of alteration (Fig. 3b,c).

In UNZ-12 the phenocrysts are visually more abundant (> 20 vol.%) than in the other specimens (Fig. 3). Nakada and Motomura (1999a) observed that groundmass crystallinity increased from (33 to 50 vol.%) with decreasing effusion rate, as was the case towards the end of the eruption (Nakada et al., 1995b), consistent with ~ 55 vol.% groundmass crystallinity in the 1994–95 spine (Wallace et al. *in review*). These observations are also consistent with the crystal fractions measured in UNZ-12, collected from the near–vent area.

3.~~2~~1.4 The influence of thermal stressing

The skeletal volume, mass and dimensions of each core were measured before and after thermal stressing in order to assess changes in porosity that may accompany microstructural adjustment in the process. Results showed that over the 12 cores subjected to thermal stressing, the change in connected porosity was less than 0.001, which is within the resolution of the method. Thus, it may be said that thermal stressing did not markedly create pores or connect isolated vesicles~~create significantly more pores nor connect isolated vesicles~~. It did however cause a slight decrease in the values of Young's Modulus.

3.2 Uniaxial compressive experiments

3.2.1 Mechanical response of Mt. Unzen dome rocks

Uniaxial compressive strength tests were conducted on 66 cores at ambient temperature. For those samples which had a brittle response to uniaxial compression, the failure process can be segregated into 4 stages (Hoek and Bieniawski, 1965; e.g. Brace et al., 1966; Scholz, 1968; Heap et al., 2014a). An initial build–up of stress has been attributed to the closure of micro–cracks perpendicular to σ_1, this is the initial convex segment on the stress–strain curve (e.g. Fig. 4a,b). The second, linear increase in stress and strain ~~is recoverable and~~ has been attributed to dominantly elastic (recoverable) deformation. Strain hardening, marks the onset of micro–fracturing that imparts permanent, non–recoverable damage, causing deviation from the linear elastic regime during loading (seen as the concave section of the stress–strain curve; Fig. 4a,b). Finally, a peak in stress is reached, followed by an abrupt stress drop, this is associated with through–going fracture propagation and coalescence before macroscopic failure is reached. This behaviour is seen in the stress–strain curves (Fig. 4a,b, Fig. S3, S4) of all samples deformed in the brittle regime, be it at ambient temperature (for all strain rates) or at high temperatures (for faster strain rates; see section 3.2.2).

The strength of the rocks was observed to decrease with porosity (Fig. 5a). The range of strength of dense rocks is higher than porous rocks. We observe that rock strength increases with applied strain rates at all porosities, although this effect is more pronounced for dense rocks. The data suggest that the rocks deemed altered (UNZ-11, UNZ-12) are not weaker, but indeed stronger than pristine rocks with equivalent porosities (see circled data points in Fig. 5a).

The overlap between the datasets obtained for thermally stressed and as–collected samples suggests that thermal stressing did not impart significant damage or mineralogical changes (if any) to modify the strength of these rocks (Fig. 5). Yet, a closer look at the mechanical data suggests that the initial convex increase in stress with strain is more pronounced for the thermally stressed samples than for their pristine equivalent (Fig. 4c), indicating that the thermally stressed samples have more cracks to close than their untreated equivalents. It is therefore likely that t~~t~~hermal stressing has caused the creation or opening of micro–fractures, dislocating the rocks slightly in the process, but not enough to cause a notable increase in porosity or decrease in strength~~.~~

3.2.2 Rheological response of Mt. Unzen dome lavas

The mechanical data of lavas show a wider range of behaviour than those obtained on rocks at ambient temperature (Fig. 4a,b). At slower strain rates of 10^{-4} and 10^{-5} s^{-1}, samples may provide a viscous response. Initially, the stress-strain curves exhibit only a mildly convex stress build–up, but then deformation is dominated by a stress relaxation phase which results in a levelling of the stress to a steady value as strain amasses (orange and red lines, Fig. 4a, 4b). This represents the viscous flow of the suspension and, as such, its apparent viscosity can be calculated from the mechanical data. At faster strain rates $> 10^{-3}$ s^{-1}, samples may respond brittlely. In this regime, as at ambient (room) temperature, stress accumulation may eventually lead to failure and a significant stress drop (e.g. maroon line Fig. 4b). The behaviour that links the viscous and brittle response is termed transitional. If the plateau in the stress-strain curves is marked with minor stress drops, this signals a transitional

response to deformation that is dominantly viscous. Where there is a major drop in the stress-strain curve that takes place over an extended period of strain, we termed this response brittle–dominated transitional (maroon line Fig. 4a). This interpretation of mechanical data can also be confirmed by analysing the microstructure of deformed samples (Fig. 6). Samples with pervasive macro–fractures that propagate through both groundmass and, to a lesser extent, the phenocrysts have likely undergone fully brittle deformation. Likewise, samples with a response classified as brittle–dominated transitional also have pervasive macro–fractures, however the phenocrysts are only slightly displaced along their cleavage planes, rather than shattered. Samples that have had a viscous–dominated transitional response to strain display microfractures in both the groundmass and phenocrysts, and those that have had a viscous response show little to no micro–fracturing. A viscous response may also lead to elongation of porosity parallel to the sense of shear.

~~At the faster strain rate of 10^{-3} s^{-1}, the samples responded brittlely, like at room temperature; stress accumulation eventually led to failure and significant stress drop, although not as rapid as the stress drops monitored during failure of cold lavas (e.g. Fig. 4a). The samples deformed at lower strain rates of 10^{-5} s^{-1} and 10^{-4} s^{-1} underwent viscous responses, and thus have differently shaped stress–strain curves. Initially, they exhibit only a mildly convex stress build–up (more obvious in the brittle examples), but then deformation is dominated by a stress relaxation phase which results in a levelling of the stress to a steady value as strain amasses. This represents the viscous flow of the suspension, and as such its apparent viscosity can be calculated from the mechanical data.~~

The evolution of apparent viscosity is strain–rate dependent as shown by the stepped strain rate experiment (~~Fig. 6~~Fig. 7). An increase in the strain rate resulted in an order of magnitude decrease in viscosity – a thixotropy of similar magnitude as that described for highly crystalline magmas in Lavallée et al. (2007). In this experiment, deformation at low strain rates of 10^{-6} s^{-1}, 10^{-5} s^{-1} and 10^{-4} s^{-1}, is marked by a non–linear increase in apparent viscosity (upon stress relaxation) and plateauing to a constant value for each strain–rate step; this value decreased with increase of the applied strain rate (~~Fig. 6~~Fig. 7). Deformation was pervasive (i.e., ductile), which, being above T_g, suggests that it may have dominantly occurred via a viscous response. At 10^{-3} s^{-1}, however, the apparent viscosity plummeted as the sample underwent failure along a localised fault, evidencing a transition into the brittle regime (~~Fig. 6~~Fig. 7b).

~~When in the brittle regime (a~~At strain rates of 10^{-3} s^{-1}~~)~~ the sample suite tested reached peak stresses of ~ 20–80 MPa (~~Fig. 7~~Fig. 8a) and strength decreased inversely with porosity. Here the samples responded with a brittle and brittle–dominated transitional response to strain. ~~T~~The mechanical responses of samples tested at ~~hese~~ high temperature ~~experiments~~ were more repeatable than those carried out at ambient temperature~~:~~, the strength of samples (within a family with ~ 0.01 ~~%~~ porosity range) was~~failed~~ within ~ 2 % of each other at low porosities (< 0.20) and within ~ 5 % of each other at high porosities (> 0.20), whereas at ambient temperatures a variation of ~ 60 % is observed in the lower porosity regime (Table 1).

When a strain rate of 10^{-4} s^{-1} was applied some of the samples reached peak stresses between ~ 10 and 35 MPa (Fig.7b), before relaxing the stress through substantial strain. Here, ~~instead of solely brittle behaviour,~~ the lavas display a viscous and viscous–dominated transitional response to strain. In some samples, an initially viscous response transitioned to fracturing after a certain amount of strain~~At first, the response was viscous, then, in some samples, after a certain amount of strain, fracturing occurred~~, leading to macroscopic failure. Samples that did not fracture continued to flow viscously with increasing strain, with a component of strain hardening, similar to that seen by Kendrick et al. (2013b). Samples that were subjected to a strain rate of 10^{-5} s^{-1} had a fully viscous response over the strain rates tested (~~Fig. 7~~Fig. 8c). Remarkably, the peak stresses of samples tested at 10^{-4} and 10^{-5} s^{-1} were seemingly independent of porosity (~~Fig. 7~~Fig. 8d).

The apparent viscosities calculated from the responses at 10^{-5} and 10^{-4} s^{-1} show an initial increase (due to relaxation in the first 0.7 % strain) and levelling to within a narrow range (see ~~Fig. 8~~Fig. 9a,b). For a given strain rate, we note a small range of apparent viscosities, but importantly, no systematic change in viscosity as a function of sample porosity (within the range tested; ~~Fig. 8~~Fig. 9c).

These results indicate that the transition in deformation mode from macroscopically ductile to brittle behaviour is straddled by our experiments in the range 10^{-5} to 10^{-3} s^{-1}.

4. Interpretation of dome rock mechanics

4.1 Mechanical responses of rocks and lavas in the brittle and brittle–dominated transitional regime

The experimental findings presented here suggest that the mechanical response of lavas and rocks is similar, but important differences remain. Experiments carried out on rocks at ambient temperature and (all strain rates), and on some lavas at high temperature and high strain rates of 10^{-3} s^{-1}, resulted in brittle behaviour. However, there are significant differences in the mechanical response between the two (Fig. 4). (1) We noted a shorter convex portion at high temperature at the onset of the stress–strain curve of tests at high temperature (Fig. S3), which we attribute to a narrowing of pre–existing cracks at high temperature (due to thermal expansion of the materials with heating; e.g., Fig. S5), resulting in a smaller extent of crack closure during initial loading; of samples at high temperature; (2) Most most high-temperature samples have a shallower linear portion of stress–strain build–up, which we hypothesise may reflect a contribution of viscous deformation upon loading, leading to a brittle–dominated transitional classification; and (3) we observed a less angular concave down portion of the stress–strain curve, which we attribute to more pervasive deformation (as seen by longer strain to failure; Fig. 9 Fig. 10) and micro–fracturing leading to failure. The exception to these findings is in the highest porosity sample, UNZ-7, where there appears to be no significant change in shape between high and ambient temperature experiments (see Fig. S3, S4). This sample was classified in the fully brittle regime. But iIt remains that at higher temperature, lavas are stronger (by 10–40 MPa; Figs 4–9) than their rock equivalents at ambient temperature. Before delving in their differences (section 4.1.4), we will first interpret the results on the strength (section 4.1.2) and Yyoung's Mmodulus (section 4.1.3) of porous rocks at ambient temperature.

4.1.2 The effect of porosity on material strength

From the results of the uniaxial compressive experiments it is evident that porosity is a major control on the strength of dome materials maximum stresses reached by the samples. Previous studies on volcanic rocks (Al-Harthi et al., 1999; Heap et al., 2014a, 2014b, 2016b; Schaefer et al., 2015) have found a similar correlation. Therefore, it can be said that, in which. to a first order, strength is inversely proportional to the porosity of the rock.

Here, the strength of samples with higher porosities have display less scatter than those with lower porosities (Fig. 9 Fig. 10a). The mMicrostructuresal examination of the samples (Fig. 3) show reveals the porosity of the porous specimens to be dominated by vesicles, while whereas the porosity of the denser samples is dominated by microfractures, which may define a change in the microstructural control on the strength and failure mechanism between of low and high porosity samples. Given the pore structures, in the higher porosity specimens the behaviour of failure could be described using the pore emanating crack model of Sammis & Ashby (1986), whereas, in the lower porosity experiments, the main failure mechanism could be explained by the sliding wing crack model of Ashby & Sammis (1990). In these lower porosity specimens, the non–systematic orientation of microfractures could be responsible for the large scatter in strength. The uniaxial compressive strength was calculated for the samples for both the pore–emanating crack model of Sammis & Ashby (1986) (Eq. 3) and the sliding wing crack model of Ashby & Sammis (1990) (Eq. 4). For the former, the uniaxial compressive strength was calculated with varying values of $\frac{K_{IC}}{\sqrt{\pi r}}$ from 5 MPa to 25 MPa (Fig. 11). For the latter, approximate values for μ, $\frac{K_{IC}}{\sqrt{\pi c}}$ and D_0 were taken from Table 3 in Paterson and Wong (2005) as 0.51, 20–30 MPa and 0.3–44, respectively. This gave a range of estimated strength between 54 and 90 MPa (Fig. 11). At higher porosities, > 0.25, the pore–emanating crack model with $\frac{K_{IC}}{\sqrt{\pi r}} = 5–10$ MPa seems to fit the data well, whereas

28

for most rocks with porosities of 0.12–0.2 $\frac{K_{IC}}{\sqrt{\pi r}}$ = 10–15 MPa is a better fit. This could be explained by a decrease in the pore radius at these porosities, leading to higher values of $\frac{K_{IC}}{\sqrt{\pi r}}$, though, as the samples are heterogeneous and pore radius variability is high we cannot observe this (Figure 3). For the densest rocks in the study (~0.08–0.12), the UCS data would suggest yet a higher $\frac{K_{IC}}{\sqrt{\pi r}}$ of 20–25 MPa. The pore–emanating crack model could explain this switch in behaviour if there was a fundamental change in pore radius. However, the switch could also be explained by a transition in failure mechanism from pore–emanating cracks to wing cracks, meaning the wing–crack model would be more applicable. Alternatively, it may be a complex combination of the two. Although the solutions to the sliding wing–crack model are non–unique, as there are few experimentally constrained parameters, when combined with information gained from the pore structures (Fig. 3), the results of the modelling presented (Fig. 11) give us an insight into the dominant micromechanical failure mode of our samples. It is likely that the complex pore structures of these lavas, generated by a combination of vesiculation, deformation and cooling-driven contraction require an as-yet undefined combination of the two models. The weighting towards one or the other, however indicates that for the higher porosity specimens the behaviour of failure could be described using the pore–emanating crack model of Sammis & Ashby (1986), whereas in the lower porosity samples deformed in uniaxial compression, the main failure mechanism is explained by the sliding wing–crack model of Ashby & Sammis (1990).

This transition in the preference of fracture nucleation site from pore to crack is likely to be gradual and dependent on the pore network architecture of a suite of samples; in these Mt. Unzen samples it is found at a porosity of ~ 0.2. Other studies have also alluded to such a transition when studying permeability, finding a transition from crack-dominated to pore-connectivity-dominated regime of fluid flow at values of ~ 0.14 (Farquharson et al., 2015), 0.155 (Heap et al., 2015b), 0.105–0.31 (Kushnir et al., 2016), ~ 0.15 (Eggertsson et al., 2018)(Eggertsson et al., *in review*), and 0.11–0.18 (Lamur et al., 2017). Samples UNZ-11 (porosity: 0.30) and UNZ-13 (porosity: 0.32) both have elongated vesicles. The cores were cut so that the vesicles were either perpendicular or parallel to the applied principal stress, σ_1, for UNZ-11 and UNZ-13, respectively (Fig.3). The porosities of the two rocks are comparable, and there is no great difference in strength, indicating that pore orientation may not have a significant influence on strength within dome rocks. Although we do note that UNZ-11 undergoes a higher strain to failure (Fig. 9Fig. 10b) and thus lower Young's Modulus (Fig. 9Fig. 10c) than UNZ-13, indicating that it is less stiff.; Sample UNZ-2 (porosity: 0.13) however, does have a remarkably larger uniaxial compressive strength (~20 MPa) and Young's Modulus (~5–10 GPa) than samples of similar porosity. This may be due to UNZ 2, it has the highest number of spherical isolated pores (Table 3) which are spherical (i.e. low Ca) (see Fig. S2) and sowhich act as rigid bodies. However, it cannot be explicitly stated that pore anisotropy did not play a role in this and thus it is possible As the porosities of the two rocks are comparable, and as they have similar strengths, it can be noted that, for Mt. Unzen, the orientation of a vesicle does not have a major influence on the strength of a rock. Although recent findings indicate that the orientation of a pore may havehas a dominant effect on the a rock's strength and stiffness of the dome rock (Bubeck et al., 2017; Griffiths et al., 2017) we do not observe that for the porous network architecture of the Mt. Unzen rocks tested here. However, we do note that UNZ-11 undergoes a higher strain to failure (Fig. 9b) and thus lower Young's Modulus (Fig. 9c) than UNZ-13; as their porous structure is similar, we turn to their mineral constituents. UNZ-11 had been collected from the dome, owing to its altered look (crusted, white and friable; see Fig. S1). Although the geochemical analysis suggests a certain degree of alteration, we did not observe any alteration of the main mineral phases nor deposition of any secondary mineral phases in our textural analysis, yet the latter may still have in-filled fine cracks and it is possible that the glass devitrified as a result of hydration, which may affect the mechanical response. For instance, UNZ-12, which was also selected for its altered and oxidised appearance, have less Mg, Ti, and Fe (attributed by Goto et al. (2008) to the production of haematite from oxidisation), a higher degree of microfractures and a far more complex microstructure than similar rocks; yet, it is the strongest rock investigated here. Thus, future studies on rock strength may benefit from an in-depth study of rock strength as a function of pore fractionosity, orientation and alteration.and connectivity.

29

4.1.3 Static Young's Modulus

At ambient temperatures, the static Young's modulus decreases from > 15 GPa to < 5 GPa with increasing porosity (~~Fig. 9~~Fig.
1085   10c). This is an indication that samples with lower porosities were stiffer than those with higher porosities. However, there
were outliers to the data trend, UNZ-13 and UNZ-2 (with average porosities of 0.32 and 0.13, respectively) are stiffer and have
higher (> 5 GPa) Young's Moduli than other rocks with similar porosities (see Table 1~~).);~~ ~~This suggests that these samples~~
~~are stiffer than the other specimens tested, and indeed those experiments reached unusually high peak stresses at relatively low~~
~~strains to failure. This is intuitive as the pores~~ in UNZ-13~~-~~, this may be explained by the preferred orientation of pores~~are~~
1090   parallel to the principal stress (Figure 3a) ~~and are therefore harder to deform~~(cf, Griffiths et al., 2017)~~, as for UNZ-2, it has the~~
~~highest number of isolated pores (Table 3) which are spherical (i.e. low Ca) (see Fig. S2) and so act as rigid bodies~~. The
naturally altered samples, tested at similar conditions, exhibited Young's Moduli trends like those of comparable fresh rocks
(~~Fig. 9~~Fig. 10c).

Lavas deformed at 900 °C~~, but which failed in the brittle field (i.e~~. at a strain rate of 10^{-3} s^{-1}~~)~~ have systematically lower (~ 5–
1095   10 GPa) Young's ~~M~~moduli. It is this malleability that allows the lava to be deformed to higher strains before macroscopic
failure (~~Fig. 9~~Fig. 10b), an observation recognised in Schaefer et al., (2015) in tests on basaltic lavas.

In addition, thermally stressed samples have slightly lower (~ 0.5–1.5 GPa) Young's ~~M~~moduli than their unstressed
equivalents, as previously noted in dacites from Mt. St. Helens (Kendrick et al., 2013a) and andesites from Colima volcano
(Heap et al., 2014a). The slight decrease in static Young's modulus with thermal stresses~~. This~~ highlights a potential change
1100   in porosity distribution that was not recognised by other means (e.g. total porosity, strength).

4.1.4 The effect of temperature on sample strength

Remarkably, when in the brittle regime at high temperature, samples exhibited strengths ~ 10–40 MPa greater than at ambient
temperature. This may be attributed to the way the samples respond to stress at higher temperatures. First, upon heating a rock,
it expands, which may partially close pre~~-~~existing micro~~-~~fractures, thus modifying the resultant elastic response of the
1105   material (see section 4.1.1). Moreover, at 900 °C the presence of interstitial melt in a sample allows for considerably more
strain than if it were deformed at ambient temperature (when in a solid, glassy state). The initial strain upon loading would be
accommodated by both an instantaneous and a delayed ~~(relaxation)~~ elastic response (e.g. Dingwell and Webb, 1989) and
perhaps minor micro–crack closure (e.g. Heap et al., 2014a), before the onset of viscous (e.g. Lavallée et al., 2007) and crystal
plastic (e.g. Kendrick et al. 2017) deformation that results in permanent ~~deformation~~ strain (and barrelling of the sample).
1110   Thus, at higher temperatures, more strain is accommodated upon loading than at ambient temperature (~~Fig. 6~~Fig. 7a), leading
to higher strain to failure (~~Fig. 9~~Fig. 10b) and lower Young's Moduli than their rock counterparts (~~Fig. 9~~Fig. 10c). The Young's
Moduli for lavas undergoing failure at high temperature are rate–dependent, perhaps as they may undergo further stress
dissipation by viscous relaxation in the melt.

A similar increase in strength with temperature was also noted in basaltic rocks from Pacaya volcano (Schaefer et al., 2015).
1115   There, the authors attributed the increase in strength of the glass–poor rock to the closure of micro–cracks (likely formed upon
cooling after their eruption) due to thermal expansion, a process that equally occurs in Mt. Unzen dome rocks. Rocks may also
become weaker from thermal stressing, this can be due to crack initiation (Heap et al., 2016a), or alteration, via processes such
as decarbonation and dehydroxylation (Heap et al., 2012, 2013a, 2013b). A recent study by Eggertsson et al., *in review*, found
that samples that hosted microfractures (like Mt. Unzen dome rock) were not affected by thermal stressing, while those that
1120   showed a trivial fraction of pre~~-~~existing micro~~-~~fractures were more readily fractured through thermal stressing and as a result
became more permeable.

5. Rheology of dome lavas

5.1 Viscosity of dome lavas

The style of an eruption – effusive vs explosive – depends on the rheological response of magma (Dingwell, 1996). The urge to understand the alarmingly variable nature of volcanoes, and recent advances in experimental capabilities and computational modelling, have encouraged the community to focus efforts on the development of two and three–phase models of magma rheology (e.g. Lejeune and Richet, 1995; Caricchi et al., 2007; Lavallée et al., 2007; Costa et al., 2009; Mueller et al., 2011b; Truby et al., 2015). Truby et al., (2015) combined two, two–phase flow models (considering melt and +crystals, and melt and+gas bubbles) to elaborate a three–phase model of magmatic suspensions, further tested against a set of controlled analogue laboratory data. Their model shows that while the addition of crystals increases the viscosity of a suspension, leading to a shear thinning rheology, the addition of gas bubbles (which can deform during shear) has variable consequences. Depending upon the initial crystal volume and maximum packing fraction of those crystals, the addition of gas bubbles may result in a further increase in viscosity or, in other cases, a levelling or a decrease in the apparent viscosity of the suspension. Their model suggests that the addition of bubbles to lavas, above their glass transition, with high normalised crystal fractions, like those seen in volcanic domes, would likely decrease the viscosity of the suspension. However, here, the data show that the presence of vesicles (between 0.09 and 0.33) in dome lavas may not necessarily influence the apparent viscosity (at least not systematically). We advance that this could be due to the high connectivity of the pores present in dome lavas, which allows efficient outgassing, thus the gas cannot act as an isolated phase that can pressurise during shear. Thus, it may be that lavas hosting permeable porous networks may have mostly porosity–independent apparent viscosities (at least across the range examined here), as suggested by Lavallée et al. (2007). Current models relating porosity to viscosity, simply account for the presence of isolated gas bubbles via a capillary number, to calculate the apparent viscosity of a multi–phase suspension (e.g. Rust and Manga, 2002; Llewellin and Manga, 2005; Truby et al., 2015). However, this result highlights important shortcomings to the modelling of shallow magmas, where porous networks tend to develop connectivity, especially in sheared crystal–bearing lavas (e.g. Laumonier et al., 2011; Kushnir et al., 2017). This connectivity controls outgassing, and thus pressure build–up or release, which is responsible for rheological variations in magma and therefore eruption style (effusive vs explosive). Our findings suggest that we need to revise three–phase models to account for gas flow through evolving, deformable bubbles, that may also be connected, in order to constrain the apparent viscosity of magmas in lava domes and other open–system settings.

5.2 Failure criterion for porous lavas

During magma ascent, the strain rate, which is proportional to effusion rate (e.g., Goto 1999), plays a key role in determining whether the response of magmas and extruding lavas is that of a solid, or liquid (Webb and Dingwell, 1990). Here, the macroscopic deformation mode (viscous, viscous–dominated transitional, brittle–dominated transitional or brittle) of lavas was characterised based on their resulting stress–strain curve (section 3.2.2; Fig. 12a); these are further supported by micro-structural observations (see Fig. 6; Fig. 12a). [NOTE: sample UNZ-4-28 was not given a classification as its response to deformation was likely an experimental artefact due to a chipping of the sample edge]. The distinction between these rheological regimes can be made using the Deborah number (Eq. 2). In a recent study on the failure of single phase silicate melts, Wadsworth et al., (2017) suggest that fractures can propagate above $De \geq 10^{-2}$ when a sample begins to undergo brittle deformation, although these fractures are often blunted by viscous relaxation. When $De \geq 1$ brittle behaviour dominates over viscous deformation and violent rupture of the sample ensues. This dimensionless ratio of the relaxation timescale of the melt (Eq. 1) and the observation timescale can be rewritten as:

$$De = \frac{\eta_m}{G_\infty t_{obs}},$$

31

$$De = \frac{\eta_m}{G_\infty t_{obs}} \tag{89}$$

---

where the observation time, $t_{obs,}$ is the inverse of the strain rate of magma deformation, $\dot{\varepsilon}_{obsexp}$. Thus Eq. 89 can be rewritten as:

$$De = \dot{\varepsilon}_{exp}\eta_m / G_\infty,$$

$$De = \frac{\dot{\varepsilon}_{obs}\eta_m}{G_\infty} \tag{910}$$

Magmatic suspensions, like those described in this study, are non–Newtonian materials with a shear thinning response (Caricchi et al., 2007; Lavallée et al., 2007; Cordonnier et al., 2009; Avard and Whittington, 2012; Vona et al., 2013), hence their viscosity is strain rate dependent. It has previously been described that the peak stress, σ, shares a power law relationship with strain rate, $\dot{\varepsilon}_{exp}$, via:

$$\sigma = k\dot{\varepsilon}_{obsexp}{}^{b}, \tag{1011}$$

where k is the flow consistency index (in Pa.s) and b is the flow behaviour index and k is the flow consistency index (in Pa.s^b), describing the rheology of the fluids (Ostwald, 1925; Lavallée et al., 2007; Jahangiri et al., 2012). For Newtonian bodies $b = 1$, but for shear thinning suspensions, b decreases below 1 (Caricchi et al., 2007) and reaches a minimum of $b = 0.5$ for crystal–rich materials (Lavallée et al., 2007; Cordonnier et al., 2009). In the present study the Mt. Unzen dome material tested at 900 °C, by fitting a power law to the peak stress–strain curve we obtained Ostwald constants of $k = 1653$ and $b = 0.5$ (Fig. 10a12b). So, we can rewrite Eq. 910, using Eq. 1011, to obtain:

$$De = \frac{\left(\sigma/k\right)^{1/b}\eta_m}{G_\infty}, \tag{1112}$$

which permits the representation of the Deborah number of material failure as a function of strength (which was shown to be dependent on porosity), for a given temperature (and thus interstitial melt viscosity). For our samples, the interstitial melt viscosity can be estimated at $10^{9.42}$ Pa.s (using its chemistry and experimental temperature as an input parameter in the GRD viscosity calculator (Giordano et al., 2008)). In Figure 10Figure 12bc, we present the data using symbols that illustrate the response of the samples, whether it flows or fails near–instantaneously, or after some amount of strain. The onset of transitional behaviour, termed viscous–dominated transitional, is marked by the red line. Similarly, the onset of brittle behaviour, brittle–dominated transitional, is marked by the yellow line. These lines are linear regressions on a semi–log space plot, with their standard error of estimates marked by faded colour windows. Any point that plots between the red and yellow lines would be termed transitional and could demonstrate any type of hybrid behaviour. Above a porosity of 0.27 no transitional zone occurs, and behaviour would be classified as either viscous or brittle. This analysis demonstrates that the critical Deborah number, De_c, which indicates the initiation of rupture, inof dome lavas from Mt. Unzen decreases by just over half analmost one order of magnitude over a 0.35 difference range in porosity; from $\sim 7.652\times10^{-54}$ in the densest sample measured to 4.18×10^{-5} in the most porous, following the trend: $De_c = -1.75.1\times10^{-4}\varphi + 9.402.11\times10^{-54}$ (Fig. 102bc). Such a magnitude is proportional to the strength decrease of material as a function of porosity (see Fig. 9Fig. 10a and Paterson and Wong, 2005 for a discussion), and thus relates the porosity to the ability of high temperature lavas to rupture. By extrapolating the trend and finding the De_c for a hypothetical, pore–free Mt. Unzen sample, we can compare our results to a two–phase (crystals and melt) model for rupture (Wadsworth et al., 2017). Given that the Mt. Unzen material has a crystal content (microlites and phenocrysts), ϕ_x, of ~ 0.75, the bulk De_c can be modelled via:

$$De_c = De_{cx}\left(1 - \frac{\phi_x}{\phi_m}\right), \tag{13}$$

where $\mathbf{De_{cx}}$ is the critical Deborah number for a crystal and bubble free melt, 10^{-2}, and $\boldsymbol{\phi_m}$ is the maximum packing fraction of the system.

For the Mt. Unzen material $\boldsymbol{\phi_m}$ can be assumed to be in the range of ~0.76 – > 0.99, as it is clear from microstructural analysis that our material has not yet reached $\boldsymbol{\phi_m}$ (see Fig. 3) [maximum packing is defined geometrically as the volume fraction at which there is no space remining for further particles (Mader et al., 2013)]. This gives a modelled $\boldsymbol{De_c}$ in the range of ~1×10^{-4} and 7.6×10^{-4} which is in line with the $\boldsymbol{De_c}$ found by the linear extrapolation of experimental results, 9.4×10^{-5} for the onset of rupture and 6.6×10^{-4} for full rupture (Fig. 12c).

Thus both, the addition of crystals (as seen by the fact that De_c of dense dome lavas is reduced by over one order of magnitude compared to that suggested by Dingwell and Webb, (1990)) and vesicles (as shown by the above equation) contributes to an increased brittleness of lava during ascent and eruption at lava domes, and in many other eruptive scenarios.

6. Implications for volcanic scenarios

The findings observed here help constrain the impact of rheological evolution on lava domes as they erupt and cool following emplacement. The rheology of magma has a fundamental influence on the style of a volcanic eruption, be it explosive or effusive (Dingwell, 1996; Gonnermann and Manga, 2007). Understanding how magmas respond to changes in petrology, stress and eruptive shearing conditions that occur during ascent in a volcanic conduit may help to enhance models that aim to predict volcanic activity. The work undertaken here constrains the material behaviour of erupting dome lavas and the relics that remain once the lava cools.

As magma crystallises, its apparent viscosity (generally) increases as the melt evolves and an increasing fraction of the suspension becomes solid (with slower diffusivity and lower rate of plasticity than the viscous liquid melt), thus the suspension becomes increasingly solid–like. For crystalline magmas, we would expect De_c to be lower than that for silicate liquids (*i.e.*, $De_c < 10^{-2}$; e.g. Gottsmann et al., (2009)). Cordonnier et al., (2012a, 2012b) constrained the failure of silicate liquids with different crystal fractions, and they indeed showed that De_c decreases when crystallinity increases. They suggest that De_c linearly decreases from 10^{-2} to 2×10^{-3} between 0 and 60 vol.% crystals. However, the viscosity used to estimate Maxwell's relaxation rate in the De analysis was based on the suspension's apparent viscosity rather than the interstitial melt viscosity. However, tTo constrain how the addition of crystals shifts the onset of failure of a material whose rheology is well known it is advantageous to consider the pure melt. Given this, an even larger decrease of De_c would be observed (perhaps down to ~ 2.119.4$\times10^{-54}$ as constrained by failure of our densest lavas). Since the strength of material is known to be strongly influenced by the presence of pores (commonly vesicles in volcanic materials) and micro–fractures (e.g. Paterson and Wong, 2005 for a review of material properties in the brittle field), here we demonstrate that the addition of porosity to magma shifts failure to lower strain rates; thus, under constant ascent conditions, magma may undergo failure simply by vesiculation, without the need for any increase in strain rate.

Upon extrusion, dome lava cools, contracts and fractures (Lamur et al., 2018)(Heap et al., 2015a). Here we show that the strength of a dome is reduced upon cooling due to contraction and micro–fracturing, leaving a weaker relic structure. This situation may favour the progressive creep of cooling dome structures, as observed in lobe 11 at Mt. Unzen (Kohashi et al., 2012).

Post–emplacement, through time and prolonged exposure to corrosive fluids, dome material may alter (Ball et al., 2015). In this study, the altered rocks tested showed a higher strength than pristine rocks with equivalent porosities. However, previous studies have found that altered volcanic rocks can also be weaker (e.g. Pola et al., 2012). From this distinction we surmise that the structure of the rocks as well as the type of alteration (developing under different conditions in cooling volcanic rocks) may have contrasting effect on the strength of cooled dome lavas. Thus, the data shown here begs for an increased focus on the impact of alteration on volcanic rock strength for improved lava dome structural stability models.

The rate of deformation imposed on dome materials is also an important variable to be considered. In this study, and in others (e.g. Schaefer et al., 2015; Lavallée et al., 2018), volcanic rocks have been shown to withstand higher stresses when deformed at higher strain rates. Previous studies have suggested earthquakes with high ground acceleration have provoked lava dome collapse (Voight, 2000), therefore, it is essential to understand the effect of strain rate on the strength of materials. This is of particular importance for Mt. Unzen as it is located in a very seismically active area. Slow, continuous strain (or recurring stressing cycles) can induce fatigue in a material and promote brittle creep (e.g. Heap and Faulkner, 2008; Heap et al., 2009; Brantut et al., 2013; Kendrick et al., 2013a; Schaefer et al., 2015) thus weakening the rocks which undergo failure at lower stresses. Thus, over long periods (years) of deformation, such as for lobe 11 at Mt. Unzen, the actual strength of the dome rocks may be lower than those reported here at the lowest strain rate of 10^{-5} s^{-1}). Time-dependent deformation can importantly contribute to catastrophic collapse of volcanic structures (e.g. Mt. St. Helens, Reid et al. 2010). Here we ~~surmise~~ advance that it is crucial for future failure models of volcanic materials to incorporate the effect of strain rate.

Volcanic structures are made of heterogeneous rocks and lavas, with intricate mineralogical assemblages, textures and fabrics, with variable degrees of coherence; thus, their mechanical response may vary widely. Although here we have only tested material from the 1991–1995 eruption of Mt. Unzen, this study has the potential to be applied to other dome–forming volcanoes of similar composition, crystallinity, and porosity. Additionally, the work can also be applied to parts of larger volcanic edifices dominantly constructed by the accumulation of lavas, which may be prone to collapse (Ball et al., 2015). The work presented here can help constrain the behaviour of lavas and rocks involved in lava dome eruptions. We anticipate that the results will form the basis for more advanced numerical simulations of dome eruption and related hazards.

7. Conclusion

Uniaxial experiments carried out at ambient and high temperature (900 °C) on a suite of natural lavas from Mt. Unzen have given significant insight into the behaviour of lava domes, both during extrusion and after emplacement. Ambient temperature experiments allowed for the investigation of brittle behaviour, and results from these experiments can be applied to cooling domes (and the relics that they leave in the record) allowing the development of volcanic edifice failure models. Conclusions drawn from experimentation are as follows:

1. In the brittle regime, strength decreases with increasing pore volume both at ambient and high temperatures;

2. Magmas deformed in the brittle regime at high temperature are stronger than rocks of equivalent porosity deformed at ambient temperature;

3. ~~The orientation of a vesicle may not necessarily have a discerning control on the strength of a rock, however it does have an influence on the strains reached at failure and, as such, the Young's Modulus;~~

~~4.~~3. Thermal stressing did not affect the strength of dome rocks within the conditions tested (< 900 ˚C and 4 ˚C.min^{-1}), it did however change the morphology of the stress strain curve, indicating the widening of cracks;

~~5.~~4. The presence of alteration may have variable effects, sometimes strengthening volcanic rocks;

~~6.~~5. The strength of rocks and lavas (in the brittle field at high temperature) increases with strain rate;

~~7.~~6. The viscosity of dome lavas decreased with strain rate (shear thinning) and did not vary for the range of material crystallinity and porosity studied ~~with porosity (for the crystallinity studied)~~;

~~8.~~7. Lavas deformed at high temperature and strain rates of > 10^{-4} s^{-1} becomes increasingly brittle, and adopt fully brittle response above 10^{-3} s^{-1}; and

~~9.~~8. The critical Deborah number, De_c of dense dome lavas was found to be ca. ~~2.1~~1×10^{-4}. It decreases with porosity according to a ~~the~~ linear relationship ~~$De_c = -5.1 \times 10^{-4} \varphi + 2.11 \times 10^{-4}$~~.

These results reveal that current stability models of cooling lava domes, like that of lobe 11 at Mt. Unzen, require an integration of the complex nature of the materials. The outcome of this study suggests that, as a primary control on rock strength, porosity

heterogeneities must be included when modelling failure mechanisms. As secondary controls, it would also be beneficial to include deformation conditions such as temperature and strain rate. Conclusions drawn from high temperature experiments suggest that current three–phase models may not be fully applicable to dome lavas and other crystal–rich lavas. We suggest a new formulation of the Deborah number that applies to porous, crystal–rich lavas and propose that it may help refine the accuracy of models attempting to describe rheological evolution to explain geophysical data monitored during lava dome eruptions.

Data availability

Supplementary data are available in the Supporting Information "S1" to "S6". The script for the Young's Modulus calculation is freely available on Github (https://doi.org/10.5281/zenodo.1287237). Further information can be obtained on request from the corresponding author.

Author contribution

YL and JEK designed the experiments. RC, AJH, TM, JEK, PAW, and JDA carried out the mechanical experiments and physical measurements. PAW collected microprobe data and conducted softening point determination. RC wrote the processing codes, analysed the data, and prepared the manuscript with contributions from all co–authors. All authors contributed to the collection and selection of samples.

Competing interests

The authors declare that they have no conflict of interest.

Acknowledgements

References

Al-Harthi, A. A., Al-Amri, R. M. and Shehata, W. M.: The porosity and engineering properties of vesicular basalt in Saudi Arabia, Eng. Geol., 54(3–4), 313–320, doi:10.1016/S0013-7952(99)00050-2, 1999.

Almberg, L. D., Larsen, J. F., Eichelberger, J. C., Vogel, T. a. and Patino, L. C.: Comparison of eruptive and intrusive samples from Unzen Volcano, Japan: Effects of contrasting pressure-temperature-time paths, J. Volcanol. Geotherm. Res., 175(1–2), 60–70, doi:10.1016/j.jvolgeores.2008.03.020, 2008.

Angelo Heilprin: Mont Pelée and the Tragedy of Martinique: A Study of the Great Catastrophes of 1902, with Observations

and Experiences in the Field, J. B. Lippincott Company., 1903.

1315   Ashby, M. F. and Sammis, C. G.: The damage mechanics of brittle solids in compression, Pure Appl. Geophys., 133(3), 489–521, doi:10.1007/BF00878002, 1990.

Ashwell, P. A., Kendrick, J. E., Lavallée, Y., Kennedy, B. M., Hess, K., Von Aulock, F. W., Wadsworth, F. B., Vasseur, J. and Dingwell, D. B.: Permeability of compacting porous lavas, J. Geophys. Res. - Solid Earth, (120), 1605–1622, doi:10.1002/2014JB011519.Received, 2015.

1320   Ashworth, J. D., Wallace, P. A., Kendrick, J. E., Coats, R., Miwa, T., Matsushima, T. and Lavallée, Y.: Conduit permeability in dilational and compactional shear zones: a case of Unzen volcano, Japan, *(submitted)*

Avard, G. and Whittington, A. G.: Rheology of arc dacite lavas: experimental determination at low strain rates, Bull. Volcanol., 74(5), 1039–1056, doi:10.1007/s00445-012-0584-2, 2012.

Ball, J. L., Stauffer, P. H., Calder, E. S. and Valentine, G. A.: The hydrothermal alteration of cooling lava domes, Bull.
1325   Volcanol., 77(12), 1–16, doi:10.1007/s00445-015-0986-z, 2015.

Barmin, A., Melnik, O. and Sparks, R. S. J.: Periodic behavior in lava dome eruptions, Earth Planet. Sci. Lett., 199(1–2), 173–184, doi:10.1016/S0012-821X(02)00557-5, 2002.

Baud, P., Wong, T. fong and Zhu, W.: Effects of porosity and crack density on the compressive strength of rocks, Int. J. Rock Mech. Min. Sci., 67, 202–211, doi:10.1016/j.ijrmms.2013.08.031, 2014.

1330   Brace, W. F., Paulding, B. W. and Scholz, C.: Dilatancy in the fracture of crystalline rocks, J. Geophys. Res., 71(16), 3939–3953, doi:10.1029/JZ071i016p03939, 1966.

Brantut, N., Heap, M. J., Meredith, P. G. and Baud, P.: Time-dependent cracking and brittle creep in crustal rocks: A review, J. Struct. Geol., 52(1), 17–43, doi:10.1016/j.jsg.2013.03.007, 2013.

Bubeck, A., Walker, R. J., Healy, D., Dobbs, M. and Holwell, D. A.: Pore geometry as a control on rock strength, Earth Planet.
1335   Sci. Lett., 457, 38–48, doi:10.1016/j.epsl.2016.09.050, 2017.

Calder, E. S., Luckett, R., Sparks, R. S. J. and Voight, B.: Mechanisms of lava dome instability and generation of rockfalls and pyroclastic flows at Soufrière Hills Volcano, Montserrat, in Geological Society, London, Memoirs, vol. 21, pp. 173–190., 2002.

Calder, E. S., Lavallée, Y., Kendrick, J. E. and Bernstein, M.: Lava Dome Eruptions, in The Encyclopedia of Volcanoes, edited
1340   by H. Sigurdsson, B. Houghton, H. Rymer, J. Stix, and S. McNutt, pp. 343–362, Elsevier., 2015.

Caricchi, L., Burlini, L., Ulmer, P., Gerya, T., Vassalli, M. and Papale, P.: Non-Newtonian rheology of crystal-bearing magmas and implications for magma ascent dynamics, Earth Planet. Sci. Lett., 264(3–4), 402–419, doi:10.1016/j.epsl.2007.09.032, 2007.

Cashman, K. V.: Groundmass crystallization of Mount St. Helens dacite, 1980-1986: a tool for interpreting shallow magmatic
1345   processes, Contrib. to Mineral. Petrol., 109(4), 431–449, doi:10.1007/BF00306547, 1992.

Cashman, K. V. and Sparks, R. S. J.: How volcanoes work: A 25 year perspective, Bull. Geol. Soc. Am., 125(5–6), 664–690, doi:10.1130/B30720.1, 2013.

Castro, J. M., Manga, M. and Martin, M. C.: Vesiculation rates of obsidian domes inferred from H2O concentration profiles, Geophys. Res. Lett., 32(21), 1–5, doi:10.1029/2005GL024029, 2005.

1350   Cole, P. D., Calder, E. S., Druitt, T. H., Hoblitt, R., Robertson, R., Sparks, R. S. J. and Young, S. R.: Pyroclastic flows generated by gravitational instability of the 1996-97 lava dome of Soufriere Hills Volcano, Montserrat, Geophys. Res. Lett., 25(18), 3425–3428, 1998.

Collombet, M., Wadsworth, F. B., Gurioli, L., Scheu, B., Kueppers, U., Di Muro, A. and Dingwell, D. B.: The evolution of pore connectivity in volcanic rocks, Earth Planet. Sci. Lett., 462, 99–109, doi:10.1016/j.epsl.2017.01.011, 2017.

1355   Cordonnier, B., Hess, K., Lavallée, Y. and Dingwell, D. B.: Rheological properties of dome lavas: Case study of Unzen volcano, Earth Planet. Sci. Lett., 279(3–4), 263–272, doi:10.1016/j.epsl.2009.01.014, 2009.

Cordonnier, B., Caricchi, L., Pistone, M., Castro, J. M., Hess, K., Gottschaller, S., Manga, M., Dingwell, D. B. and Burlini, L.: The viscous-brittle transition of crystal-bearing silicic melt: Direct observation of magma rupture and healing, Geology, 40(7), 611–614, doi:10.1130/G3914.1, 2012a.

1360 Cordonnier, B., Schmalholz, S. M., Hess, K. and Dingwell, D. B.: Viscous heating in silicate melts: An experimental and numerical comparison, J. Geophys. Res. Solid Earth, 117(2), 1–13, doi:10.1029/2010JB007982, 2012b.

Costa, A., Caricchi, L. and Bagdassarov, N.: A model for the rheology of particle-bearing suspensions and partially molten rocks, Geochemistry, Geophys. Geosystems, 10(3), 1–13, doi:10.1029/2008GC002138, 2009.

Deubelbeiss, Y., Kaus, B. J. P., Connolly, J. and Caricchi, L.: Potential causes for the non-Newtonian rheology of crystal-
1365 bearing magmas, Geochemistry, Geophys. Geosystems, 12(5), 1–22, doi:10.1029/2010GC003485, 2011.

Dingwell, D. B.: Volcanic Dilemma: Flow or Blow?, Science (80-.)., 273, 1054–1055, doi:10.1126/science.273.5278.1054, 1996.

Dingwell, D. B. and Webb, S. L.: Structural relaxation in silicate melts and non-Newtonian melt rheology in geologic processes, Phys. Chem. Miner., 16(5), 508–516, doi:10.1007/BF00197020, 1989.

1370 Dingwell, D. B. and Webb, S. L.: Relaxation in silicate melts, Eur. J. Mineral., 2(4), 427–449, doi:10.1127/ejm/2/4/0427, 1990.

Eggertsson, G. H., Lavallée, Y., Kendrick, J. E. and Markússon, S.: Improving fluid flow in geothermal reservoirs by thermal and mechanical stimulation: The case of Krafla volcano, Iceland, J. Volcanol. Geotherm. Res., doi:https://doi.org/10.1016/j.jvolgeores.2018.04.008, 2018.

1375 Einstein, A.: A new determination of the molecular dimensions, Ann. Phys., 34, 591–592 (Translation of the 1906 German version, 1911.

Elsworth, D. and Voight, B.: Evaluation of volcano flank instability triggered by dyke intrusion, Geol. Soc. London, Spec. Publ., 110, 45–53, doi:10.1144/GSL.SP.1996.110.01.03, 1996.

Farquharson, J. I., Heap, M. J., Varley, N. R., Baud, P. and Reuschlé, T.: Permeability and porosity relationships of edifice-
1380 forming andesites: A combined field and laboratory study, J. Volcanol. Geotherm. Res., 297, 52–68, doi:10.1016/j.jvolgeores.2015.03.016, 2015.

Farquharson, J. I., Heap, M. J., Baud, P., Reuschlé, T. and Varley, N. R.: Pore pressure embrittlement in a volcanic edifice, Bull. Volcanol., 78(1), 6, doi:10.1007/s00445-015-0997-9, 2016.

Fink, J. H. and Anderson, S. W.: Lava domes and coulees, in The Encyclopedia of Volcanoes, edited by H. Sigurdsson, B.
1385 Houghton, H. Rymer, J. Stix, and S. McNutt, pp. 307–318, Academic Press., 2000.

Fluegel, A.: Glass viscosity calculation based on a global statistical modelling approach, Glas. Technol. J. Glas. …, 48(1), 13–30 [online] Available from: http://www.ingentaconnect.com/content/sgt/gt/2007/00000048/00000001/art00003, 2007.

Gent, A. N.: Theory of the parallel plate viscometer, Br. J. Appl. Phys., 11(February), 85–87, doi:10.1088/0508-3443/11/2/310, 1960.

1390 Giordano, D., Russell, J. K. and Dingwell, D. B.: Viscosity of magmatic liquids: A model, Earth Planet. Sci. Lett., 271(1–4), 123–134, doi:10.1016/j.epsl.2008.03.038, 2008.

Gonnermann, H. M. and Manga, M.: The Fluid Mechanics Inside a Volcano, Annu. Rev. Fluid Mech., (39), 321–356, doi:10.1146/annurev.fluid.39.050905.110207, 2007.

Goto, A.: A new model for volcanic earthquake at Unzen Volcano: Melt rupture model, Geophys. Res. Lett., 26(16), 2541–
1395 2544, 1999.

Gottsmann, J., Lavallée, Y., Martí, J. and Aguirre-Díaz, G.: Magma-tectonic interaction and the eruption of silicic batholiths, Earth Planet. Sci. Lett., 284(3–4), 426–434, doi:10.1016/j.epsl.2009.05.008, 2009.

Griffiths, L., Heap, M. J., Xu, T., Chen, C. and Baud, P.: The influence of pore geometry and orientation on the strength and stiffness of porous rock, J. Struct. Geol., 96(February), 149–160, doi:10.1016/j.jsg.2017.02.006, 2017.

1400   Hale, A. J. and Wadge, G.: The transition from endogenous to exogenous growth of lava domes with the development of shear bands, J. Volcanol. Geotherm. Res., 171, 237–257, doi:10.1016/j.jvolgeores.2007.12.016, 2008.

Harris, A. J. L., Flynn, L. P., Matías, O. and Rose, W. I.: The thermal stealth flows of Santiaguito dome , Guatemala : Implications for the cooling and emplacement of dacitic block-lava flows, GSA Bull., (5), 533–546, 2002.

Heap, M. J. and Faulkner, D. R.: Quantifying the evolution of static elastic properties as crystalline rock approaches failure,
1405   Int. J. Rock Mech. Min. Sci., 45(4), 564–573, doi:10.1016/j.ijrmms.2007.07.018, 2008.

Heap, M. J., Vinciguerra, S. and Meredith, P. G.: The evolution of elastic moduli with increasing crack damage during cyclic stressing of a basalt from Mt. Etna volcano, Tectonophysics, 471(1–2), 153–160, doi:10.1016/j.tecto.2008.10.004, 2009.

Heap, M. J., Faulkner, D. R., Meredith, P. G. and Vinciguerra, S.: Elastic moduli evolution and accompanying stress changes with increasing crack damage: Implications for stress changes around fault zones and volcanoes during deformation, Geophys.
1410   J. Int., 183(1), 225–236, doi:10.1111/j.1365-246X.2010.04726.x, 2010.

Heap, M. J., Lavallée, Y., Laumann, A., Hess, K., Meredith, P. G. and Dingwell, D. B.: How tough is tuff in the event of fire?, Geology, 40(4), 311–314, doi:10.1130/G32940.1, 2012.

Heap, M. J., Lavallée, Y., Laumann, A., Hess, K., Meredith, P. G., Dingwell, D. B., Huismann, S. and Weise, F.: The influence of thermal-stressing (up to 1000 °C) on the physical , mechanical , and chemical properties of siliceous-aggregate , high-
1415   strength concrete, Constr. Build. Mater., 42, 248–265, doi:10.1016/j.conbuildmat.2013.01.020, 2013a.

Heap, M. J., Mollo, S., Vinciguerra, S., Lavallée, Y., Hess, K., Dingwell, D. B., Baud, P. and Iezzi, G.: Thermal weakening of the carbonate basement under Mt . Etna volcano (Italy): Implications for volcano instability, J. Volcanol. Geotherm. Res., 250, 42–60, doi:10.1016/j.jvolgeores.2012.10.004, 2013b.

Heap, M. J., Lavallée, Y., Petrakova, L., Baud, P., Reuschlé, T., Varley, N. R. and Dingwell, D. B.: Microstructural controls
1420   on the physical and mechanical properties of edifice-forming andesites at Volcán de Colima, Mexico, J. Geophys. Res. Solid Earth, 119(4), 2925–2963, doi:10.1002/2013JB010521, 2014a.

Heap, M. J., Xu, T. and Chen, C.: The influence of porosity and vesicle size on the brittle strength of volcanic rocks and magma, Bull. Volcanol., 76(9), 856, doi:10.1007/s00445-014-0856-0, 2014b.

Heap, M. J., Farquharson, J. I., Baud, P., Lavallée, Y. and Reuschlé, T.: Fracture and compaction of andesite in a volcanic
1425   edifice, Bull. Volcanol., 77(6), 55, doi:10.1007/s00445-015-0938-7, 2015a.

Heap, M. J., Farquharson, J. I. and Kolzenburg, S.: Timescales for permeability reduction and strength recovery in densifying magma, Earth Planet. Sci. Lett., 429, 223–233, doi:http://dx.doi.org/10.1016/j.epsl.2015.07.053, 2015b.

Heap, M. J., Russell, J. K. and Kennedy, L. A.: Mechanical behaviour of dacite from Mount St . Helens (USA): A link between porosity and lava dome extrusion mechanism (dome or spine)?, J. Volcanol. Geotherm. Res., 328, 159–177,
1430   doi:10.1016/j.jvolgeores.2016.10.015, 2016a.

Heap, M. J., Wadsworth, F. B., Xu, T., Chen, C. and Tang, C.: The strength of heterogeneous volcanic rocks: A 2D approximation, J. Volcanol. Geotherm. Res., 319(April), 1–11, doi:10.1016/j.jvolgeores.2016.03.013, 2016b.

Hess, K., Cordonnier, B., Lavallée, Y. and Dingwell, D. B.: Viscous heating in rhyolite: An in situ experimental determination, Earth Planet. Sci. Lett., 275(1–2), 121–126, doi:10.1016/j.epsl.2008.08.014, 2008.

1435   Hoek, E. and Bieniawski, Z. T.: Brittle Rock Fracture Propagation In Rock Under Compression Brittle Rock Fracture Propagation in Rock Under Compression, Int. J. Fract. Mech., 1(3), 137–155, doi:10.1007/BF00186851, 1965.

Hornby, A. J., Kendrick, J. E., Lamb, O. D., Hirose, T., De Angelis, S. H., Von Aulock, F. W., Umakoshi, K., Miwa, T., Henton De Angelis, S., Wadsworth, F. B., Hess, K., Dingwell, D. B. and Lavallée, Y.: Spine growth and seismogenic faulting at Mt. Unzen, Japan, J. Geophys. Res. Solid Earth, 120, doi:10.1002/2014JB011660, 2015.

1440   ISRM Turkish National Group: Suggested methods for determining the uniaxial compressive strength and deformability of rock materials, Int. J. Rock Mech. Min. Sci. Geomech. Abstr., 16(2), 137–140, doi:10.1016/0148-9062(79)91450-5, 1979.

Jahangiri, P., Streblow, R. and Müller, D.: Simulation of Non-Newtonian Fluids using Modelica, Proc. 9th Int. Model. Conf.,

57–62, doi:10.3384/ecp1207657, 2012.

Kendrick, J. E., Lavallée, Y., Ferk, A., Perugini, D., Leonhardt, R. and Dingwell, D. B.: Extreme frictional processes in the volcanic conduit of Mount St . Helens (USA) during the 2004-2008 eruption, J. Struct. Geol., 38, 61–76, doi:10.1016/j.jsg.2011.10.003, 2012.

Kendrick, J. E., Smith, R., Sammonds, P., Meredith, P. G., Dainty, M. and Pallister, J. S.: The influence of thermal and cyclic stressing on the strength of rocks from Mount St. Helens, Washington, Bull. Volcanol., 75(7), 1–12, doi:10.1007/s00445-013-0728-z, 2013a.

Kendrick, J. E., Lavallée, Y., Hess, K., Heap, M. J., Gaunt, H. E., Meredith, P. G. and Dingwell, D. B.: Tracking the permeable porous network during strain-dependent magmatic flow, J. Volcanol. Geotherm. Res., 260, 117–126, doi:10.1016/j.jvolgeores.2013.05.012, 2013b.

Kendrick, J. E., Lavallée, Y., Mariani, E., Dingwell, D. B., Wheeler, J. and Varley, N. R.: Crystal plasticity as an indicator of the viscous-brittle transition in magmas, Nat. Commun., 8(1), 1926, doi:10.1038/s41467-017-01931-4, 2017.

Kohashi, S., Shimokawa, S., Shimizu, K., Satohira, Y., Yamada, T. and Kimura, T.: Document for the committee of survey and countermeasure on lava dome collapse in Unzen Volcano (in Japanese)., 2012.

Kolzenburg, S., Heap, M. J., Lavallée, Y., Russell, J. K., Meredith, P. G. and Dingwell, D. B.: Strength and permeability recovery of tuffisite-bearing andesite, Solid Earth, 3(1), 191–198, doi:10.5194/se-3-191-2012, 2012.

Kueppers, U., Scheu, B., Spieler, O. and Dingwell, D. B.: Field-based density measurements as tool to identify preeruption dome structure: set-up and first results from Unzen volcano, Japan, J. Volcanol. Geotherm. Res., 141(1–2), 65–75, doi:10.1016/j.jvolgeores.2004.09.005, 2005.

Kushnir, A. R. L., Martel, C., Bourdier, J.-L., Heap, M. J., Reuschlé, T., Erdmann, S., Komorowski, J.-C. and Cholik, N.: Probing permeability and microstructure: Unravelling the role of a low-permeability dome on the explosivity of Merapi (Indonesia), J. Volcanol. Geotherm. Res., 316, 56–71, doi:10.1016/j.jvolgeores.2016.02.012, 2016.

Kushnir, A. R. L., Martel, C., Champallier, R. and Arbaret, L.: In situ confirmation of permeability development in shearing bubble-bearing melts and implications for volcanic outgassing, Earth Planet. Sci. Lett., 458, 315–326, doi:10.1016/j.epsl.2016.10.053, 2017.

Lamb, O. D., De Angelis, S. H., Umakoshi, K., Hornby, A. J., Kendrick, J. E. and Lavallée, Y.: Repetitive fracturing during spine extrusion at Unzen volcano, Japan, Solid Earth, 6(4), 1277–1293, doi:10.5194/se-6-1277-2015, 2015.

Lamb, O. D., Angelis, S. De, Wall, R. J., Lamur, A., Varley, N. R., Reyes-Dávila, G., Arámbula-Mendoza, R., Hornby, A. J., Kendrick, J. E. and Lavallée, Y.: Seismic and experimental insights into eruption precursors at Volcán de Colima, Geophys. Res. Lett., doi:10.1002/2017GL073350, 2017.

Lamur, A., Kendrick, J. E., Eggertsson, G. H., Wall, R. J., Ashworth, J. D. and Lavallée, Y.: The permeability of fractured rocks in pressurised volcanic and geothermal systems, Sci. Rep., (May), 1–9, doi:10.1038/s41598-017-05460-4, 2017.

Lamur, A., Lavallée, Y., Iddon, F. E., Hornby, A. J., Kendrick, J. E., Von Aulock, F. W. and Wadsworth, F. B.: Disclosing the temperature of columnar jointing in lavas, Nat. Commun., 9(1), doi:10.1038/s41467-018-03842-4, 2018.

Laumonier, M., Arbaret, L., Burgisser, A. and Champallier, R.: Porosity redistribution enhanced by strain localization in crystal-rich magmas, Geology, 39(8), 715–718, doi:10.1130/G31803.1, 2011.

Lavallée, Y., Hess, K., Cordonnier, B. and Dingwell, D. B.: Non-Newtonian rheological law for highly crystalline dome lavas, Geology, 35(9), 843–846, doi:10.1130/G23594A.1, 2007.

Lavallée, Y., Meredith, P. G., Dingwell, D. B., Hess, K., Wassermann, J., Cordonnier, B., Gerik, A. and Kruhl, J. H.: Seismogenic lavas and explosive eruption forecasting., Nature, 453(7194), 507–510, doi:10.1038/nature06980, 2008.

Lavallée, Y., Varley, N. R., Alatorre-Ibargüengoitia, M. a., Hess, K., Kueppers, U., Mueller, S. P., Richard, D., Scheu, B., Spieler, O. and Dingwell, D. B.: Magmatic architecture of dome-building eruptions at Volcán de Colima, Mexico, Bull. Volcanol., 74(1), 249–260, doi:10.1007/s00445-011-0518-4, 2012.

Lavallée, Y., Heap, M. J., Kueppers, U., Kendrick, J. E. and Dingwell, D. B.: The fragility of Volcán de Colima – a material constraint, in Volcán de Colima – Managing the Threat, edited by N. R. Varley and J. C. Komorowski, Springer., 2018.

Lejeune, A. M. and Richet, P.: Rheology of crystal-bearing silicate melts : An experimental study at high viscosities, J. Geophys. Res., 100(B3), 4215–4229, 1995.

1490 Lejeune, A. M., Bottinga, Y., Trull, T. W. and Richet, P.: Rheology of bubble-bearing magmas, Earth Planet. Sci. Lett., 166(1–2), 71–84, doi:http://dx.doi.org/10.1016/S0012-821X(98)00278-7, 1999.

Llewellin, E. W. and Manga, M.: Bubble suspension rheology and implications for conduit flow, J. Volcanol. Geotherm. Res., 143(1–3), 205–217, doi:10.1016/j.jvolgeores.2004.09.018, 2005.

Lopez, D. L. and Williams, S. N.: Catastrophic Volcanic Collapse: Relation to Hydrothermal Processes, Science (80-.).,

1495 260(5115), 1794–1796, doi:10.1126/science.260.5115.1794, 1993.

Mader, H. M., Llewellin, E. W. and Mueller, S. P.: The rheology of two-phase magmas: A review and analysis, J. Volcanol. Geotherm. Res., 257, 135–158, doi:10.1016/j.jvolgeores.2013.02.014, 2013.

Manga, M., Castro, J. M., Cashman, K. V. and Lowewenberg, M.: Rheology of bubble-bearing magmas, J. Volcanol. Geotherm. Res., 87, 15–28, 1998.

1500 Martel, C. and Schmidt, B. C.: Decompression experiments as an insight into ascent rates of silicic magmas, Contrib. to Mineral. Petrol., 397–415, doi:10.1007/s00410-002-0404-3, 2003.

Matsushima, T. and Takagi, A.: GPS and EDM monitoring of Unzen Volcano ground deformation, Earth, Planets Sp., 52(11), 1015–1018 [online] Available from: http://svr4.terrapub.co.jp/journals/EPS/pdf/5211/52111015.pdf (Accessed 5 November 2013), 2000.

1505 Maxwell, J. C.: On the dynamical theory of gases, Phil Trans. Roy. Soc. Lond., 157, 49–88, doi:10.1098/rstl.1867.0004, 1867.

McKenzie, D. and Holness, M.: Local deformation in compacting flows: Development of pressure shadows, Earth Planet. Sci. Lett., 180(1–2), 169–184, doi:10.1016/S0012-821X(00)00152-7, 2000.

Mueller, S., Melnik, O., Spieler, O., Scheu, B. and Dingwell, D. B.: Permeability and degassing of dome lavas undergoing rapid decompression: An experimental determination, Bull. Volcanol., 67(6), 526–538, doi:10.1007/s00445-004-0392-4,

1510 2005.

Mueller, S., Scheu, B., Kueppers, U., Spieler, O., Richard, D. and Dingwell, D. B.: The porosity of pyroclasts as an indicator of volcanic explosivity, J. Volcanol. Geotherm. Res., 203(3–4), 168–174, doi:10.1016/j.jvolgeores.2011.04.006, 2011a.

Mueller, S. P., Llewellin, E. W. and Mader, H. M.: The effect of particle shape on suspension viscosity and implications for magmatic flows, Geophys. Res. Lett., 38(13), 1–5, doi:10.1029/2011GL047167, 2011b.

1515 Nakada, S. and Fujii, T.: Preliminary report on the activity at Unzen Volcano (Japan), November 1990-November 1991: Dacite lava domes and pyroclastic flows, J. Volcanol. Geotherm. Res., 54(3–4), 319–333, doi:10.1016/0377-0273(93)90070-8, 1993.

Nakada, S. and Motomura, Y.: Petrology of the 1991-1995 eruption at Unzen: Effusion pulsation and groundmass crystallization, J. Volcanol. Geotherm. Res., 89(1–4), 173–196, doi:10.1016/S0377-0273(98)00131-0, 1999.

Nakada, S., Miyake, Y., Sato, H., Oshima, O. and Fujinawa, A.: Endogenous growth of dacite dome at Unzen volcano (Japan),

1520 1993-1994, Geology, 23(2), 157, doi:10.1130/0091-7613(1995)023<0157:EGODDA>2.3.CO;2, 1995a.

Nakada, S., Miyake, Y., Sato, H., Oshima, O. and Fujinawa, A.: Endogenous growth of dacite dome at Unzen volcano (Japan), 1993–1994, Geology, 23(2), 157, doi:10.1130/0091-7613(1995)023<0157:EGODDA>2.3.CO;2, 1995b.

Nakada, S., Shimizu, H. and Ohta, K.: Overview of the 1990 – 1995 eruption at Unzen Volcano, J. Volcanol. Geotherm. Res., (89), 1–22, doi:10.1016/S0377-0273(98)00118-8, 1999a.

1525 Nakada, S., Shimizu, H. and Ohta, K.: Overview of the 1990 – 1995 eruption at Unzen Volcano, J. Volcanol. Geotherm. Res., 89(89), 1–22, doi:10.1016/S0377-0273(98)00118-8, 1999b.

NASA/METI/AIST/Japan Spacesystems, and U. S. /Japa. A. S. T.: NASA EOSDIS Land Processes DAAC ASTER, DEM Prod. N032E130, doi:10.5067/ASTER/AST14DEM.003, 2001.

Ostwald, W.: Concerning the function rate of the viscosity of dispersion systems, , 36(4), 248–250, 1925.

1530 Pallister, B. J. S., Thornber, C. R., Cashman, K. V., Clynne, M. a, Lowers, H. a, Mandeville, C. W., Brownfield, I. K. and Meeker, G. P.: Petrology of the 2004 – 2006 Mount St . Helens Lava Dome — Implications for Magmatic Plumbing and Eruption Triggering, in A Volcano Rekindled: The Renewed Eruption of Mount St. Helens 2004-2006, U.S. Geological Survey Professional Paper 1750, edited by D. R. Sherrod, W. E. Scott, and P. H. Stauffer, pp. 647–702., 2008.

Paterson, M. S. and Wong, T.: Experimental Rock Deformation: The Brittle Field, 2nd Edition, Second Edi., Springer, Berlin
1535 Heidelberg., 2005.

Pierson, T. C., Janda, R. J., Thouret, J.-C. and Borrero, C. A.: Perturbation and melting of snow and ice by the 13 November 1985 eruption of Nevado del Ruiz , Colombia , and consequent mobilization , flow and deposition of lahars, J. Volcanol. Geotherm. Res., 41, 17–66, 1990.

Pola, A., Crosta, G., Fusi, N., Barberini, V. and Norini, G.: Influence of alteration on physical properties of volcanic rocks,
1540 Tectonophysics, 566–567, 67–86, doi:10.1016/j.tecto.2012.07.017, 2012.

Quane, S. L. and Russell, J. K.: Welding: insights from high-temperature analogue experiments, J. Volcanol. Geotherm. Res., 142(1–2), 67–87, doi:10.1016/j.jvolgeores.2004.10.014, 2005.

Quane, S. L., Russell, J. K. and Kennedy, L. A.: A low-load, high-temperature deformation apparatus for volcanological studies, Am. Mineral., 89(5–6), 873–877, 2004.

1545 Reid, M. E., Keith, T. E. C., Kayen, R. E., Iverson, N. R., Iverson, R. M. and Brien, D. L.: Volcano collapse promoted by progressive strength reduction: New data from Mount St. Helens, Bull. Volcanol., 72(6), 761–766, doi:10.1007/s00445-010-0377-4, 2010.

Reiner, M.: The Deborah Number, Phys. Today, 17(1), 62, doi:10.1063/1.3051374, 1964.

Roscoe, R.: The viscosity of suspensions of rigid spheres, Br. J. Appl. Phys., 3(8), 267–269, doi:10.1088/0508-3443/3/8/306,
1550 1952.

Rust, A. C. and Manga, M.: Effects of bubble deformation on the viscosity of dilute suspensions, J. Non-Newtonain Fluid Mechanaics, 104, 53–63, 2002.

Rutter, E. H.: On the nomenclature of mode of failure transitions in rocks, Tectonophysics, 122(3–4), 381–387, doi:10.1016/0040-1951(86)90153-8, 1986.

1555 Sakuma, S., Kajiwara, T., Nakada, S., Uto, K. and Shimizu, H.: Drilling and logging results of USDP-4 - Penetration into the volcanic conduit of Unzen Volcano, Japan, J. Volcanol. Geotherm. Res., 175(1–2), 1–12, doi:10.1016/j.jvolgeores.2008.03.039, 2008.

Sammis, C. G. and Ashby, M. F.: The failure of brittle porous solids under compressive stress states, Acta Metall., 34(3), 511–526, 1986.

1560 Schaefer, L. N., Kendrick, J. E., Oommen, T., Lavallée, Y. and Chigna, G.: Geomechanical rock properties of a basaltic volcano, Front. Earth Sci., 3(June), 1–15, doi:10.3389/feart.2015.00029, 2015.

Scholz, C. H.: Microfracturing and the inelastic deformation of rock in compression, J. Geophys. Res., 73(4), 1417, doi:10.1029/JB073i004p01417, 1968.

Scott, W. E., Sherrod, D. R. and Gardner, C. A.: Overview of the 2004 to 2006, and continuing, eruption of Mount St. Helens,
1565 Washington, in A Volcano Rekindled: The Renewed Eruption of Mount St. Helens, 2004-2006, U.S. Geological Survey Professional Paper 1750, vol. 1750, edited by D. R. Sherrod, W. E. Scott, and P. H. Stauffer, pp. 3–22. [online] Available from: http://pubs.usgs.gov/pp/1750/chapters/pp2008-1750_chapter01.pdf, 2008.

Siebert, L., Glicken, H. and Ui, T.: Volcanic hazards from Bezymianny- and Bandai-type eruptions, Bull. Volcanol., 49(1), 435–459, doi:10.1007/BF01046635, 1987.

1570 Siebert, L., Cottrell, E., Venzke, E. and Andrews, B.: Earth's Volcanoes and Their Eruptions: An Overview, in The Encyclopedia of Volcanoes, edited by H. Sigurdsson, B. F. Houghton, S. McNutt, H. Rymer, and J. Stix, pp. 239–256,

Elsevier., 2015.

de Silva, S. and Lindsay, J. M.: Primary Volcanic Landforms, in The Encyclopedia of Volcanoes, edited by H. Sigurdsson, B. Houghton, S. McNutt, H. Rymer, and J. Stix, pp. 273–298, Elsevier., 2015.

1575   Smith, R., Kilburn, C. R. J. and Sammonds, P. R.: Rock fracture as a precursor to lava dome eruptions at Mount St Helens from June 1980 to October 1986, Bull. Volcanol., 69(6), 681–693, doi:10.1007/s00445-006-0102-5, 2007.

Smith, R., Sammonds, P. R., Tuffen, H. and Meredith, P. G.: Evolution of the mechanics of the 2004-2008 Mt. St. Helens lava dome with time and temperature, Earth Planet. Sci. Lett., 307(1–2), 191–200, doi:10.1016/j.epsl.2011.04.044, 2011.

Sparks, R. S. J.: Causes and consequences of pressurisation in lava dome eruptions, Earth Planet. Sci. Lett., 150(3–4), 177–
1580   189, doi:10.1016/S0012-821X(97)00109-X, 1997.

Sparks, R. S. J. and Young, S. R.: The eruption of Soufrière Hills Volcano , Montserrat (1995-1999): overview of scientific results, in The Eruption of Soufri~re Hills Volcano, Montserrat, from 1995 to 1999., edited by T. H. Druitt and B. P. Kokelaar, pp. 45–69, Geological Society, London, Memoirs., 2002.

Stasiuk, M. V. and Jaupart, C.: Lava flow shapes and dimensions as reflections of magma system conditions, J. Volcanol.
1585   Geotherm. Res., 78(1–2), 31–50, doi:10.1016/S0377-0273(97)00002-4, 1997.

Surono, Jousset, P., Pallister, J., Boichu, M., Buongiorno, M. F., Budisantoso, A., Costa, F., Andreastuti, S., Prata, F., Schneider, D., Clarisse, L., Humaida, H., Sumarti, S., Bignami, C., Griswold, J., Carn, S., Oppenheimer, C. and Lavigne, F.: The 2010 explosive eruption of Java's Merapi volcano-A "100-year" event, J. Volcanol. Geotherm. Res., 241–242, 121–135, doi:10.1016/j.jvolgeores.2012.06.018, 2012.

1590   Takarada, S., Miyabuchi, Y., Hoshizumi, H., Matsushima, T. and Nagai, D.: A02: Unzen and Aso volcanoes, central Kyushu, Japan: Unzen's new lava dome climb and 1991-95 poyroclastic flows and Aso's active crater and one of the largest calderas in Japan, 2013.

Tanguy, J. C.: Rapid dome growth at Montagne Pelée during the early stages of the 1902-1905 eruption: A reconstruction from Lacroix's data, Bull. Volcanol., 66(7), 615–621, doi:10.1007/s00445-004-0344-z, 2004.

1595   Truby, J. M., Mueller, S. P., Llewellin, E. W. and Mader, H. M.: The rheology of three-phase suspensions at low bubble capillary number., Proc. Math. Phys. Eng. Sci., 471(2173), 20140557, doi:10.1098/rspa.2014.0557, 2015.

Umakoshi, K., Takamura, N., Shinzato, N., Uchida, K., Matsuwo, N. and Shimizu, H.: Seismicity associated with the 1991–1995 dome growth at Unzen Volcano, Japan, J. Volcanol. Geotherm. Res., 175(1–2), 91–99, doi:10.1016/j.jvolgeores.2008.03.030, 2008.

1600   Vallance, J. W., Schneider, D. J. and Schilling, S. P.: Growth of the 2004-2006 Lava-Dome Complex at Mount St. Helens, Washington, in A Volcano Rekindled: The Renewed Eruption of Mount St. Helens 2004-2006, edited by D. R. Sherrod, W. E. Scott, and P. H. Stauffer, pp. 169–208, U.S. Geological Survey Professional Paper 1750., 2008.

Venezky, D. Y. and Rutherford, M. J.: Petrology and Fe–Ti oxide reequilibration of the 1991 Mount Unzen mixed magma, J. Volcanol. Geotherm. Res., 89(1–4), 213–230, doi:10.1016/S0377-0273(98)00133-4, 1999.

1605   Voight, B.: Structural stability of andesite volcanoes and lava domes, Philos. Trans. R. Soc. London, 358, 1663–1703, doi:10.1098/rsta.2000.0609, 2000.

Voight, B. and Elsworth, D.: Failure of volcano slopes, Geotechnique, 47(1), 1–31, 1997.

Voight, B. and Elsworth, D.: Instability and collapse of hazardous gas-pressurized lava domes, Geophys. Res. Lett., 27(1), 1–4, 2000.

1610   Voight, B., Glicken, H., Janda, J. and Douglass, P. M.: Catastrophic rockslide avalanche of May 18, in The 1980 eruptions of Mount St Helens, Washington, vol. 1250, edited by P. W. Lipman and D. R. Mullineaux, pp. 347–378, Geological Survey Professional Paper., 1981.

Voight, B., Sparks, R. S. J., Miller, A. D., Stewart, R. C., Hoblitt, R. P., Clarke, A., Ewart, J., Aspinall, W. P., Baptie, B., Calder, E. S., Cole, P. D., Druitt, T. H., Hartford, C., Herd, R. A., Jackson, P., Lejeune, A. M., Lockhart, A. B., Loughlin, S.

1615   C., Luckett, R., Lynch, L., Norton, G. E., Robertson, R., Watson, I. M., Watts, R. and Young, S. R.: Magma Flow Instability and Cyclic Activity at Soufriere Hills Volcano , Montserrat , British West Indies, , 643(May), 2009.

Vona, A., Romano, C., Dingwell, D. B. and Giordano, D.: The rheology of crystal-bearing basaltic magmas from Stromboli and Etna, Geochim. Cosmochim. Acta, 75(11), 3214–3236, doi:10.1016/j.gca.2011.03.031, 2011.

Vona, A., Romano, C., Giordano, D. and Russell, J. K.: The multiphase rheology of magmas from Monte Nuovo (Campi

1620   Flegrei, Italy), Chem. Geol., 346, 213–227, doi:10.1016/j.chemgeo.2012.10.005, 2013.

Wadsworth, F. B., Witcher, T., Vasseur, J., Dingwell, D. B. and Scheu, B.: When Does Magma Break?, in Advances in Volcanology, Springer, Berlin, Heidelberg., 2017.

Wallace, P. A., Kendrick, J. E., Ashworth, J. D., Miwa, T., Coats, R., De Angelis, S. H., Mariani, E., Utley, J., Biggan, A. and Lavallée, Y.: Petrological architecture of a magmatic shear zone: A multidisciplinary investigation of strain localisation during

1625   magma ascent at Unzen volcano, Japan, *(in review)*

Walter, T. R., Troll, V. R., Cailleau, B., Belousov, A., Schmincke, H. U., Amelung, F. and Bogaard, P.: Rift zone reorganization through flank instability in ocean island volcanoes: An example from Tenerife, Canary Islands, Bull. Volcanol., 67(4), 281–291, doi:10.1007/s00445-004-0352-z, 2005.

Webb, S. L. and Dingwell, D. B.: The onset of non-Newtonian rheology of silicate melts - A fiber elongation study, Phys.

1630   Chem. Miner., 17(2), 125–132, doi:10.1007/BF00199663, 1990.

Webb, S. L. and Knoche, R.: The glass-transition, structural relaxation and shear viscosity of silicate melts, Chem. Geol., 128(1–4), 165–183, doi:10.1016/0009-2541(95)00171-9, 1996.

Yamamoto, T., Takarada, S. and Suto, S.: Pyroclastic flows from the 1991 eruption of Unzen volcano, Japan, Bull. Volcanol., 55(3), 166–175, doi:10.1007/BF00301514, 1993.

1635   Yilmaz, T. I., Gilg, H. ., Wallace, P. A., Hess, K., Wadsworth, F. B., Utley, J., Kendrick, J. E., Lavallée, Y., Nakada, S. and Dingwell, D. B.: Rapid three-stage clay alteration of conduit dykes from the Mt Unzen USDP-4 drill core, Geology, *(in review)*

Young, S. R., Sparks, R. S. J., Aspinall, W. P., Lynch, L. L., Miller, A. D., Robertson, R. E. A. and Shepherd, J. B.: Overview of the eruption of Soufriere Hills Volcano, Montserrat, 18 July 1995 to December 1997, Geophys. Res. Lett., 25(18), 3389–3392, doi:10.1029/98GL01405, 1998.

1640   Zhu, W., Baud, P. and Wong, T. F.: Micromechanics of cataclastic pore collapse in limestone, J. Geophys. Res. Solid Earth, 115(4), doi:10.1029/2009JB006610, 2010.
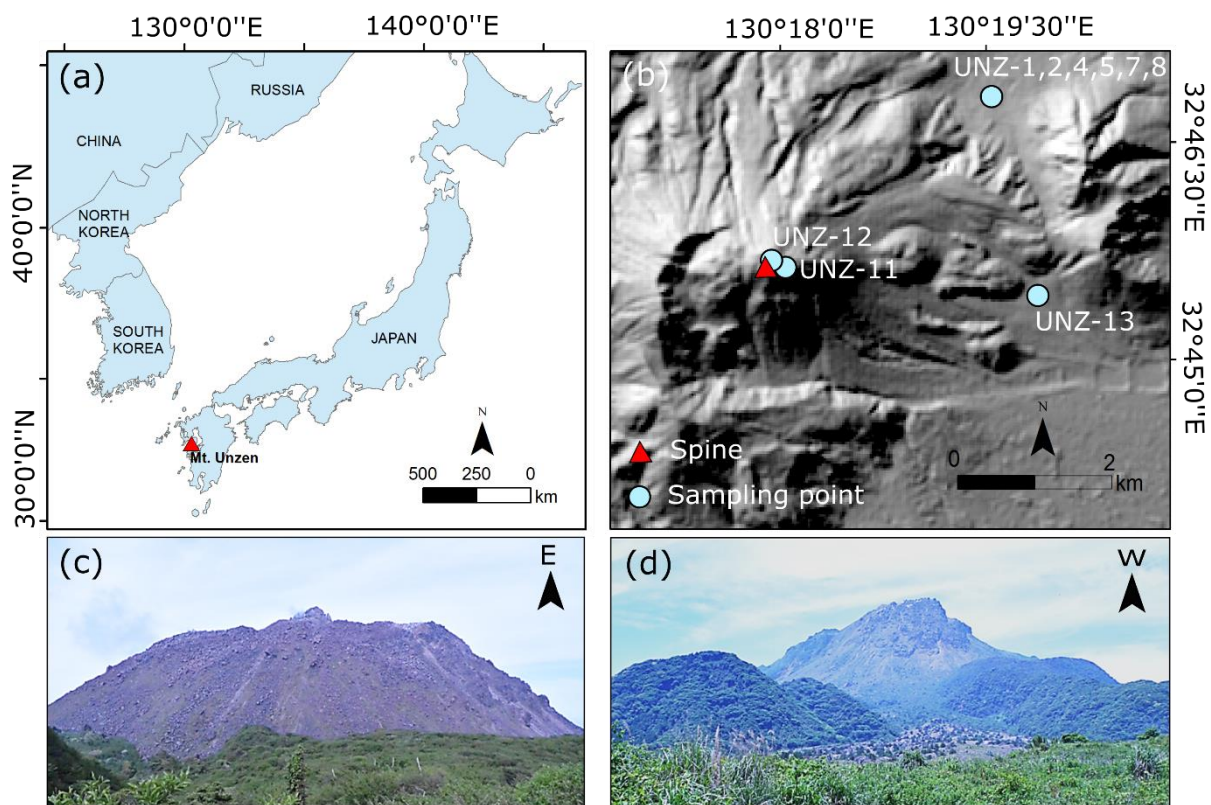
Figure 1. **(a) Location of Mt. Unzen in South Western Japan; (b) Sample collection locations and location of the erupted spine, the summit of Mt. Unzen at 1500 m above sea level (NASA/METI/AIST/Japan Spacesystems, 2001); view of Mt. Unzen lava dome looking East ~ 0.62 km from the spine (c) and West ~ 3.87 km from the spine (d) in 2016.**

1645
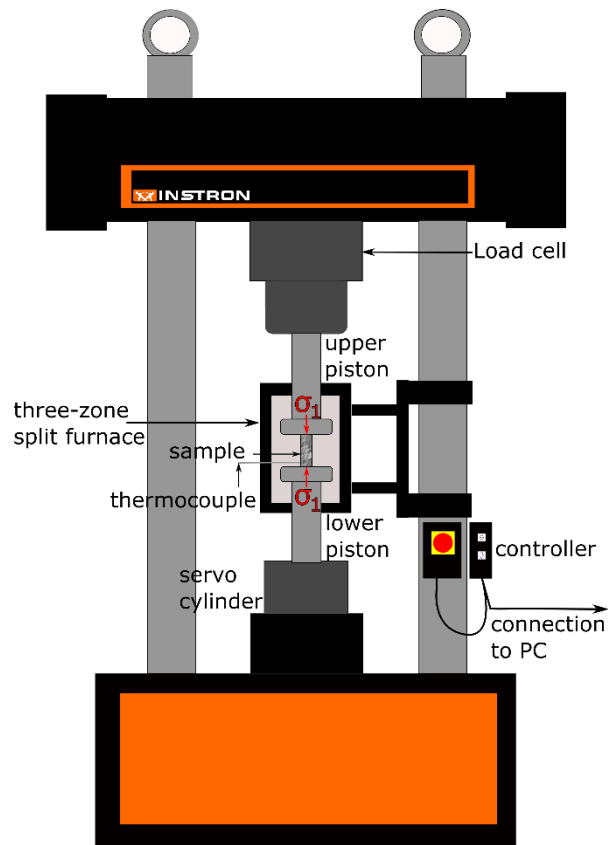
Figure 2. Schematic of the uniaxial compressive strength testing set–up in the Experimental Volcanology and Geothermal Research Laboratory at the University of Liverpool. An 100 kN Instron 8862 uniaxial press with a three–zone, split cylinder furnace was used to perform experiments at varying strain rates and temperatures.

1650

45

UNZ-4   UNZ-11   UNZ-12   UNZ-13

(a)

5 mm

(b)

Ox   Pl   Amp   Qz
                Bt
        Px

2 mm

(c)

        Poly

100 μm
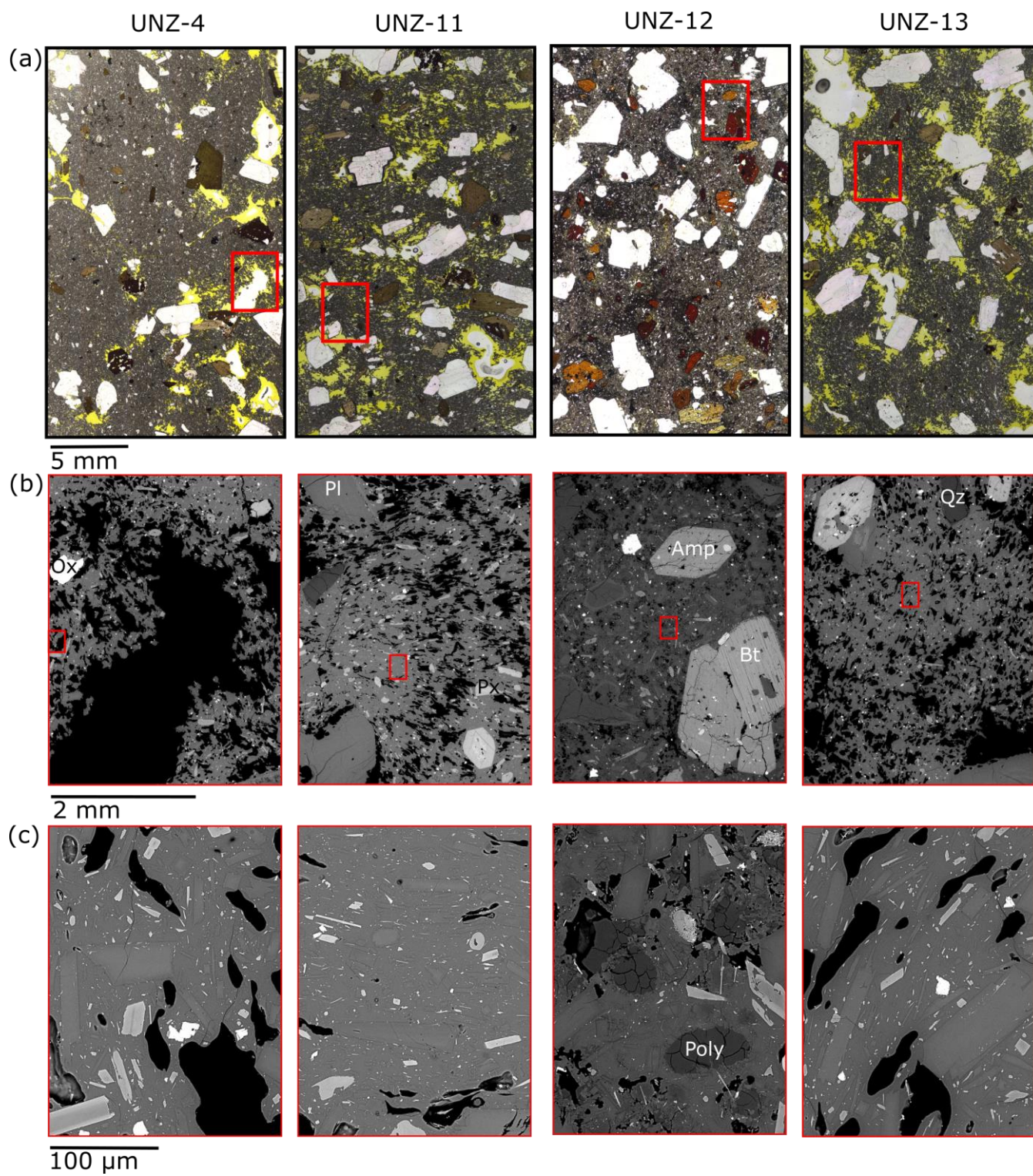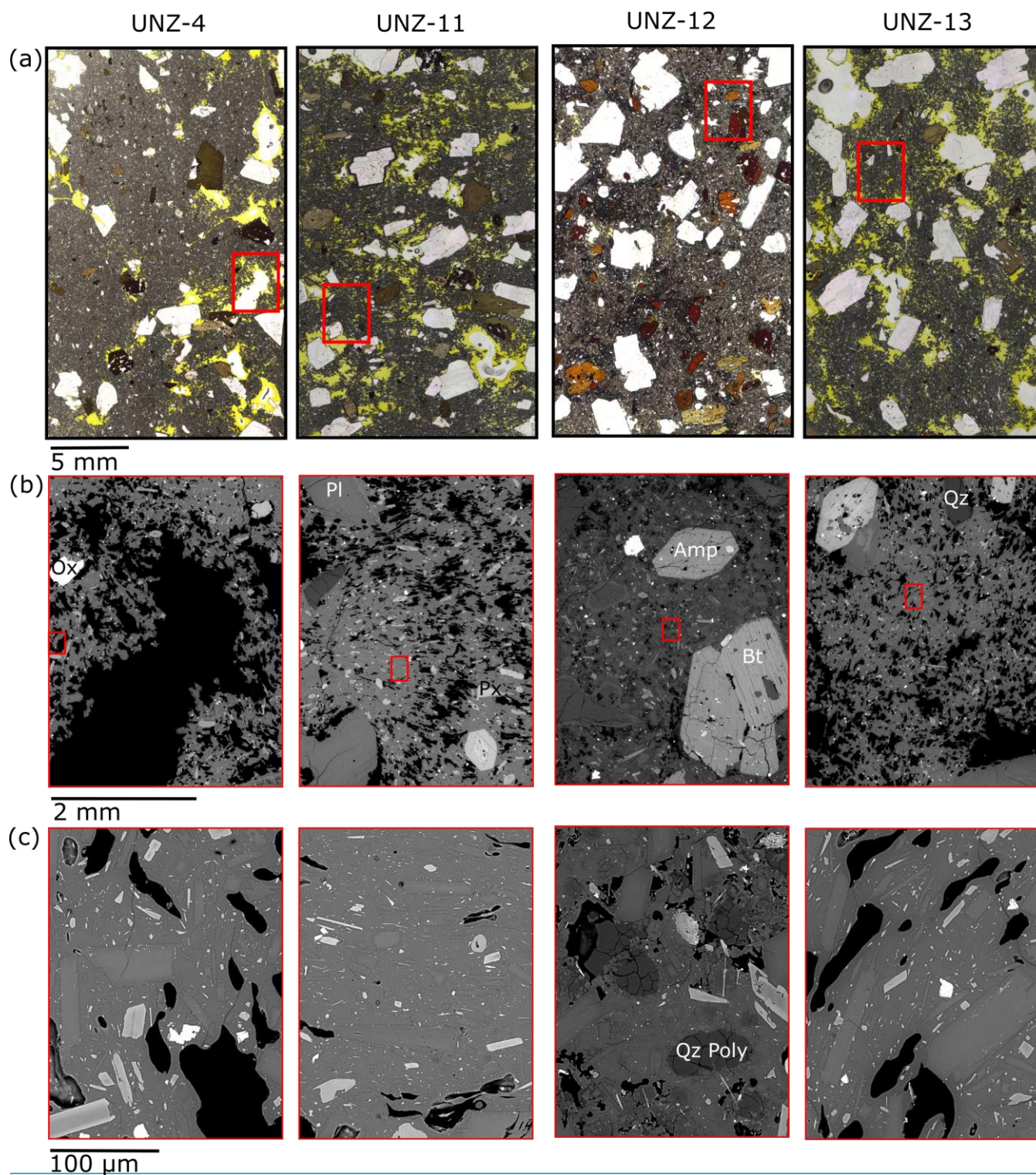
Figure 3. Plane–polarised light (a) and backscattered electron images (b,c) of undeformed samples UNZ-4,-11, -12 and -13. (b) is a zoom into the red box in (a), and (c) is a zoom in of the red box in (b), displaying the groundmass textures. Amp: Amphibole, Bt: Biotite, Ox: Oxides, Pl: Plagioclase, Px: Pyroxene, Qz, Quartz, ~~Qz~~ Poly: ~~Quartz~~ Silica ~~Polymorph~~polymorph. Images are orientated so that the later applied principal stress, σ_1, is in the vertical direction. [Note the scale that is below each set of images.]
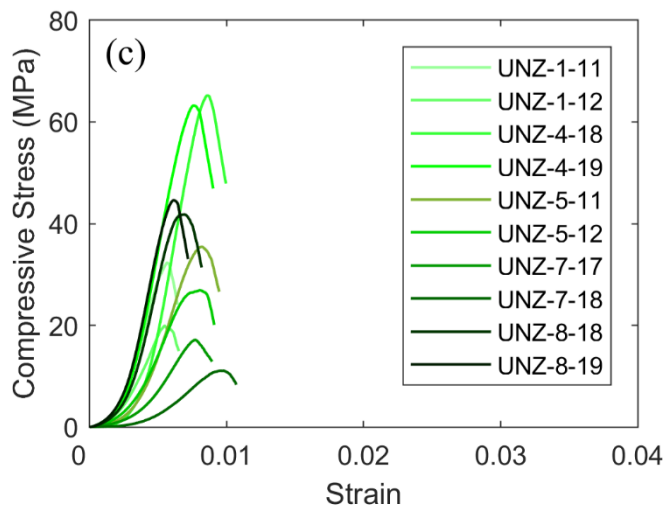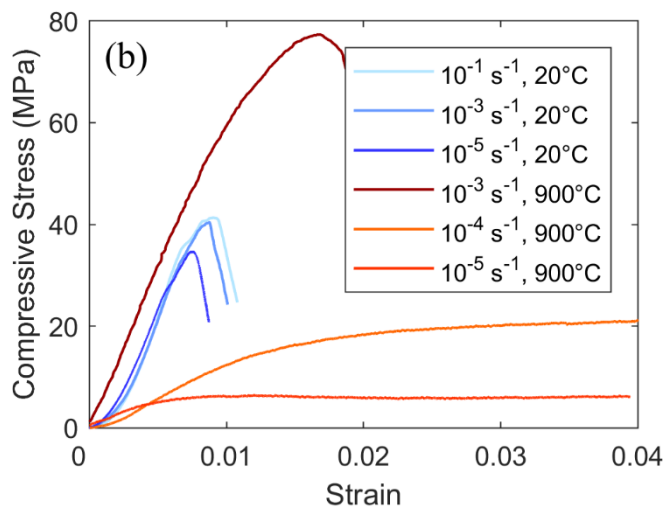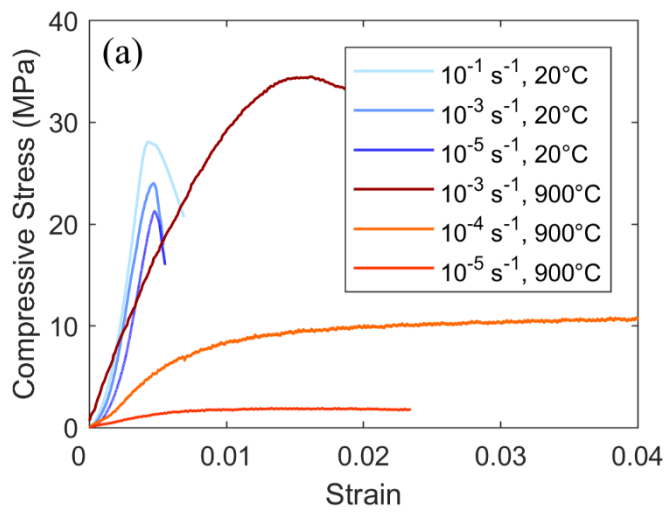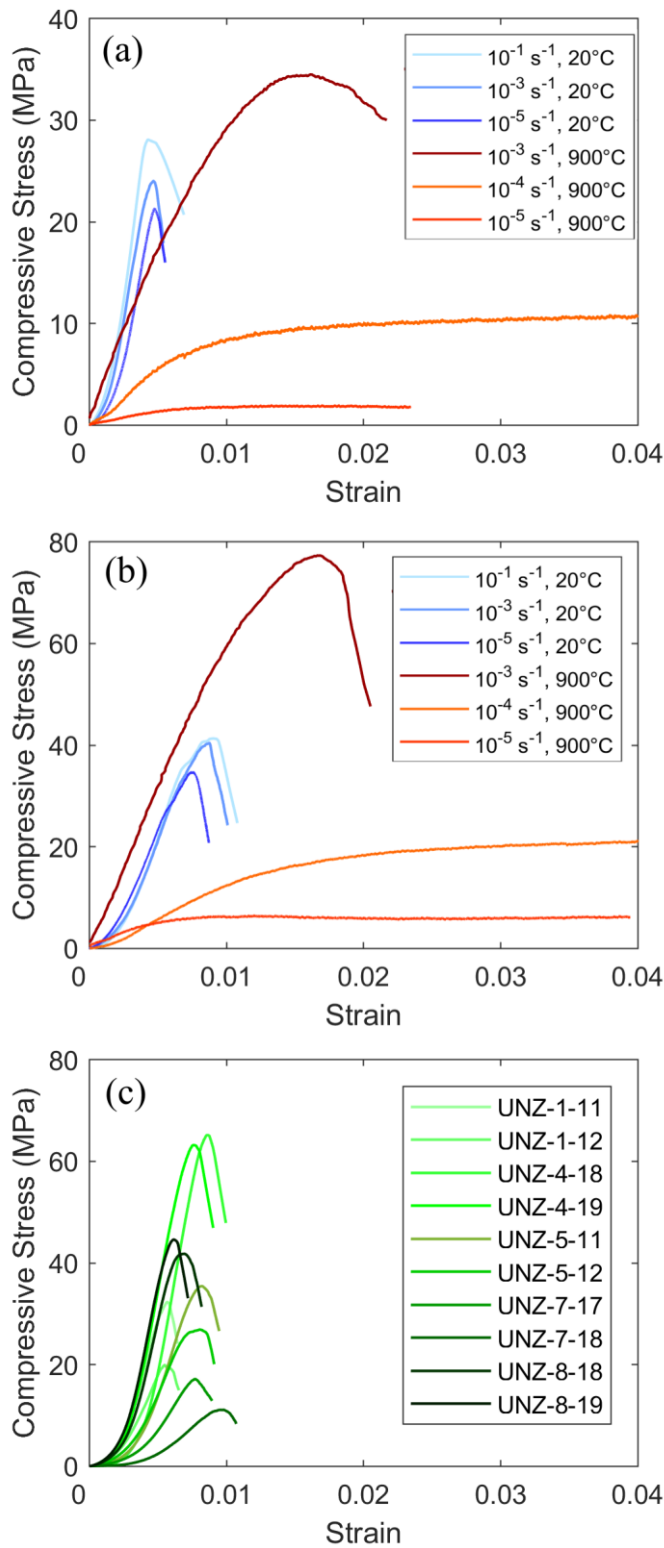
Figure 4. Examples of compressive stress–strain curves for (a) high porosity, UNZ-1 (0.21); (b) low porosity, UNZ-4 (0.12) at a range of rates and temperatures and (c) thermally stressed samples, all performed at a strain rate of 10^{-3} s^{-1}. Mechanical data for high temperature experiments are shown in shades of red, low temperature experiments in shades of blue and thermally stressed experiments in shades of green. At high temperature, faster strain rates cause the sample to break whereas at slower strain rates the sample flows. Brittle high temperature experiments fail at considerably higher peak stresses than those performed at ambient temperatures. In the brittle regime, samples deformed at faster rates failed at higher stresses. [Note: there is a difference in Y–scale between (a) and (b) & (c)]

1665
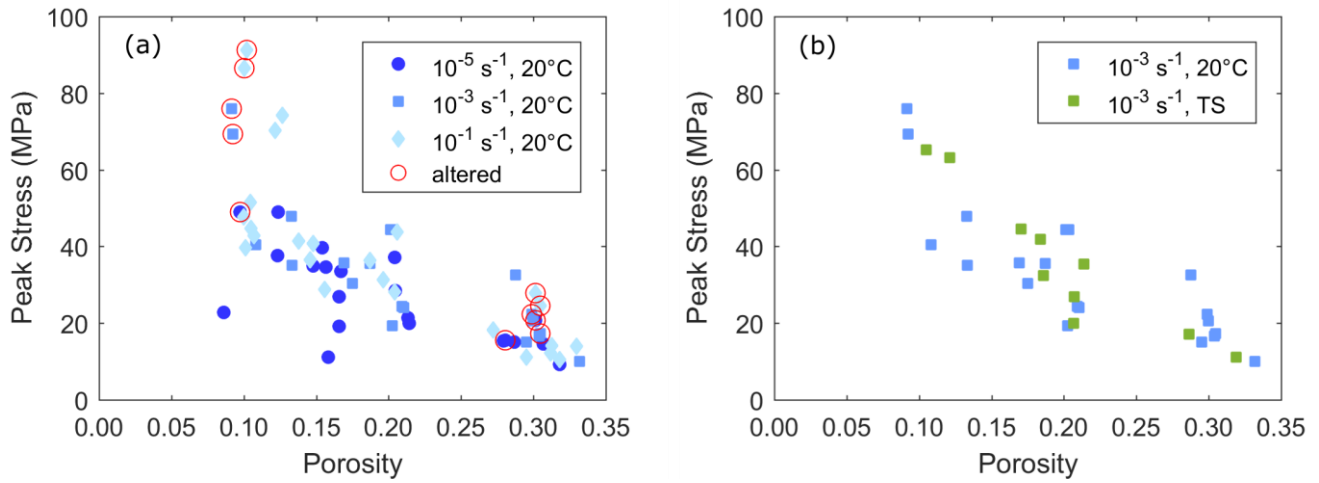
Figure 5. (a) The strength (peak stress) of samples tested at ambient temperatures at varying strain rates, highlighting the apparent strengthening of materials deformed at faster rate. Red rings circle the samples that are visibly altered. (b) A comparison of samples that were thermally stressed and those that were not, both tested at ambient temperatures and strain rates of 10^{-3} s^{-1}, demonstrating that there is no change in strength as a function of porosity due to thermal stressing.

1680

1685
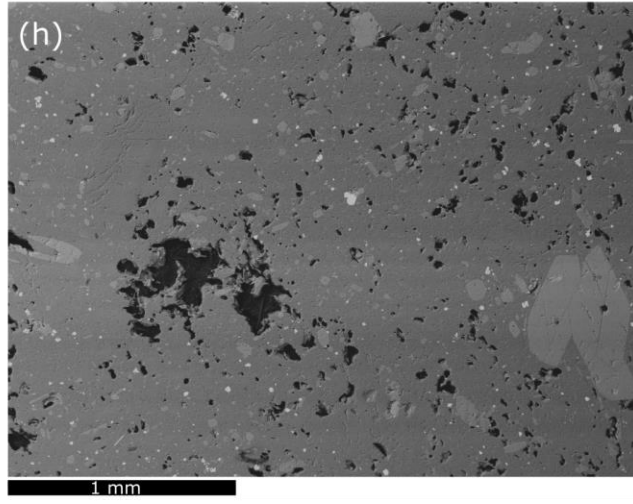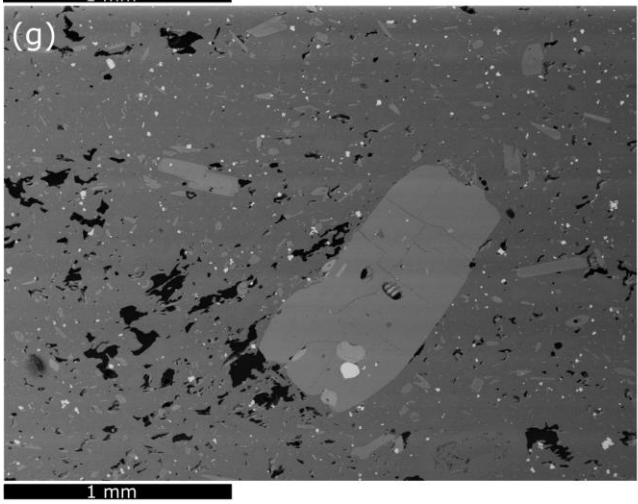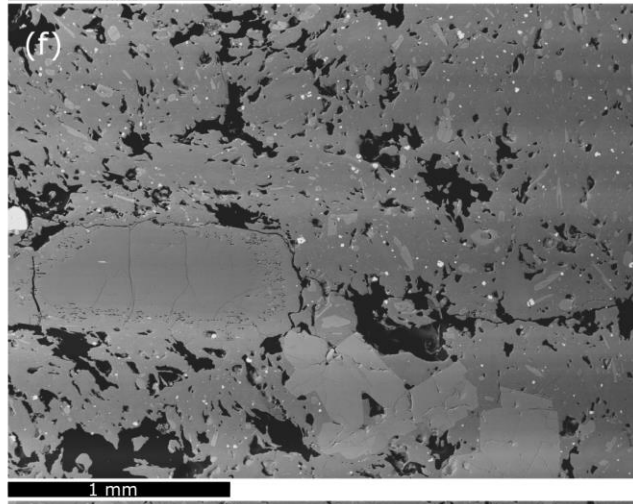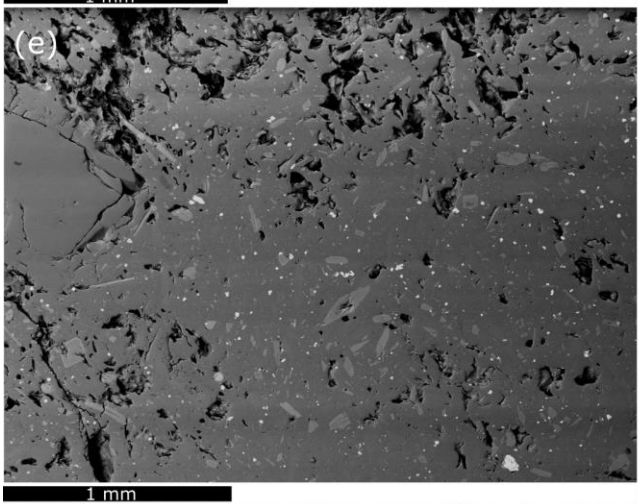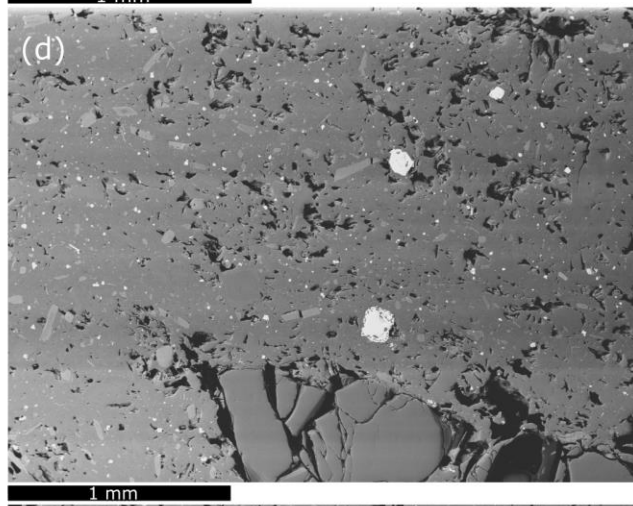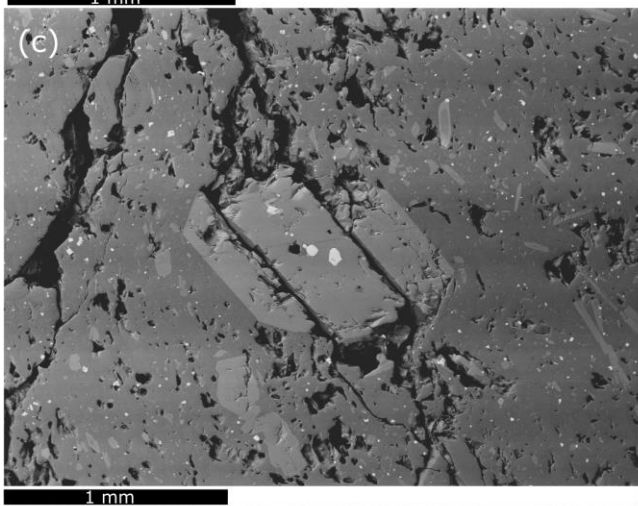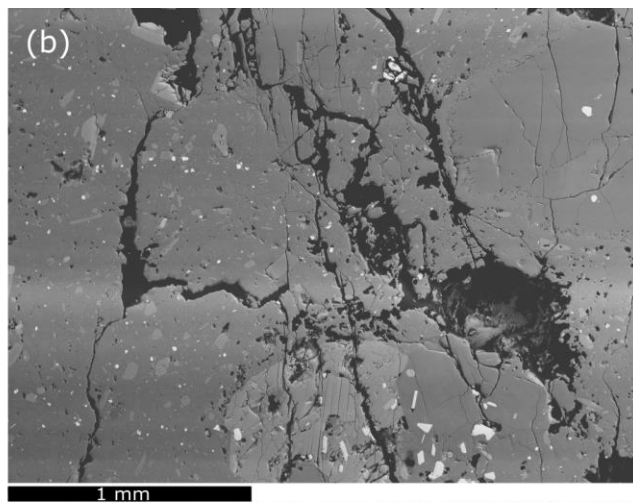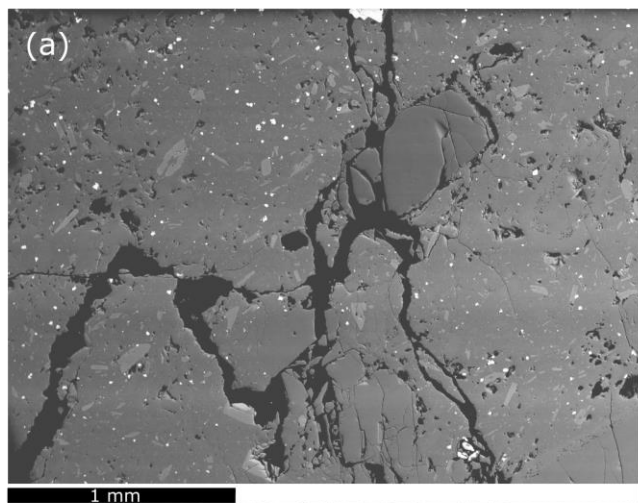
Figure 6. Backscattered electron images of polished stubs for samples after strain (a to f) and before strain (g and h). Panels a) and b) show sample UNZ-4-14 after experiencing brittle deformation at a strain rate of 10^{-3} s^{-1}; macroscopic cracks (> 100 µm in width) propagate through both the groundmass and phenocrysts. Panel c) shows sample UNZ-8-14 after experiencing brittle–dominated transitional behaviour at a strain rate of 10^{-3} s^{-1}; pervasive macroscopic fractures (> 100 µm in width) connect porosity and displace phenocrysts along their planes of weakness. Panels d) and e) are representative images of UNZ-8-21 which underwent viscous–dominated transitional behaviour when strained at 10^{-4} s^{-1}; small (< 200 µm in width) microfractures can be seen in the ground–mass glass, phenocrysts are pervasively fractured but show no sign of displacement. Panel f) is an image of sample UNZ-8-16 after experiencing viscous deformation at a strain rate of 10^{-5} s^{-1}; pores are aligned parallel to the direction of shear around phenocrysts with minor fractures < 100 µm in width. Panels g) and h) show UNZ-4 and UNZ-8, respectively, prior to deformation; with few, hairline fractures visible in the phenocrysts and little to no fractures in the smaller crystals or the groundmass glass.

1690
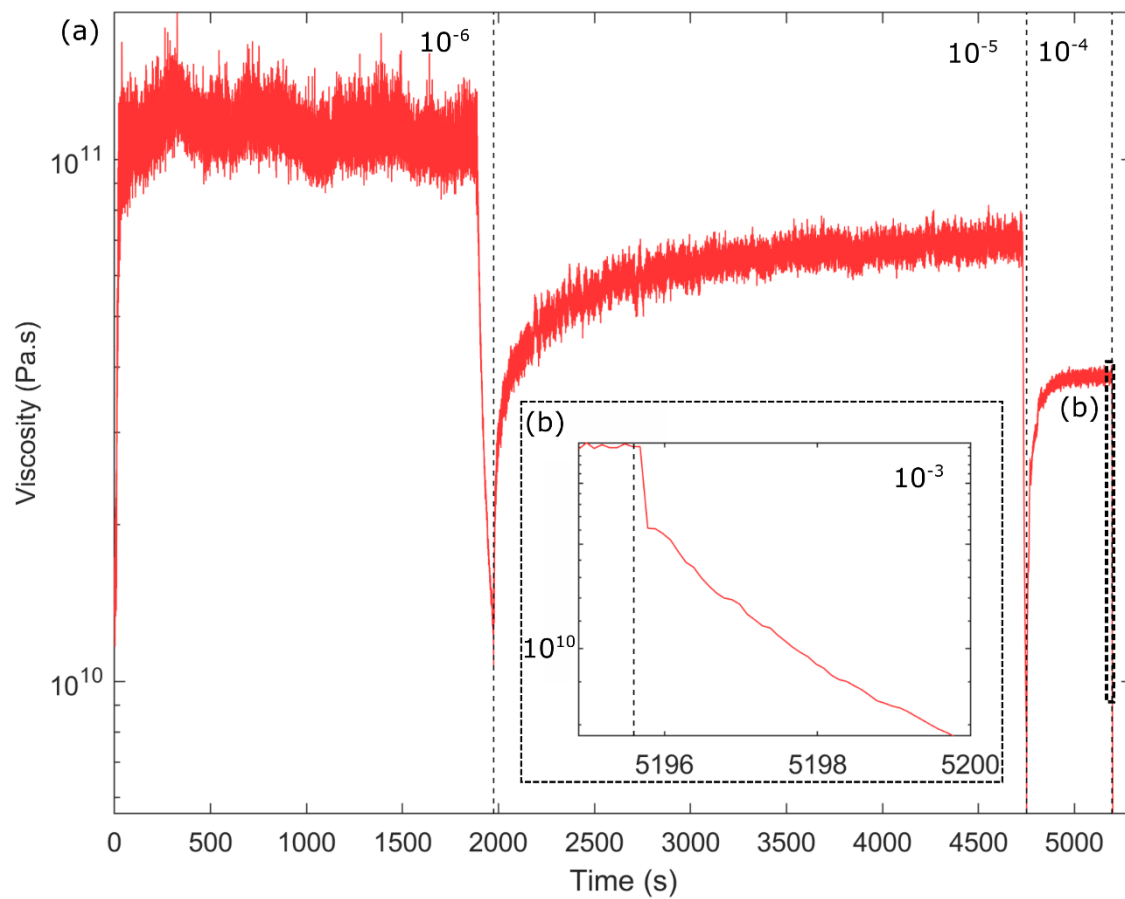
Figure 6Figure 7. Apparent viscosity evolution of UNZ-1 (porosity: 0.22) at 900 °C during a stepped strain-rate experiment (10^{-6} s^{-1}, 10^{-5} s^{-1}, 10^{-4} s^{-1}, 10^{-3} s^{-1}); each step is separated by dashed lines. The insert zooms in on the apparent viscosity decrease that accompanies sample failure at 10^{-3} s^{-1}. The decrease in viscosity at each increasing strain rate increment highlights the shear thinning behaviour of these lavas.

1695
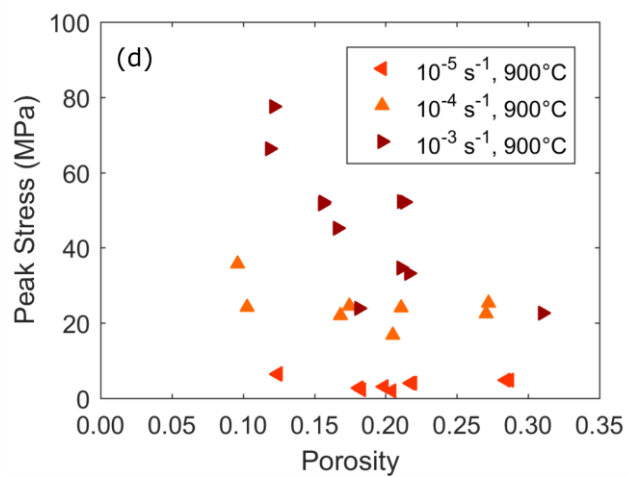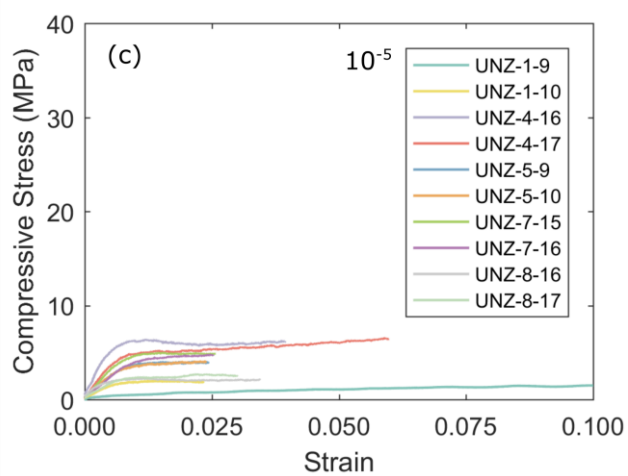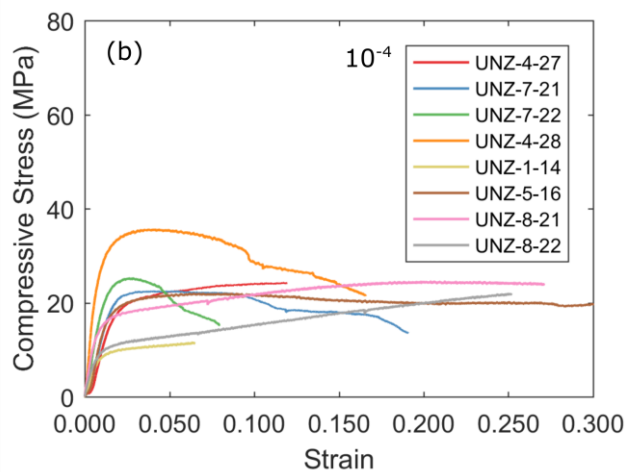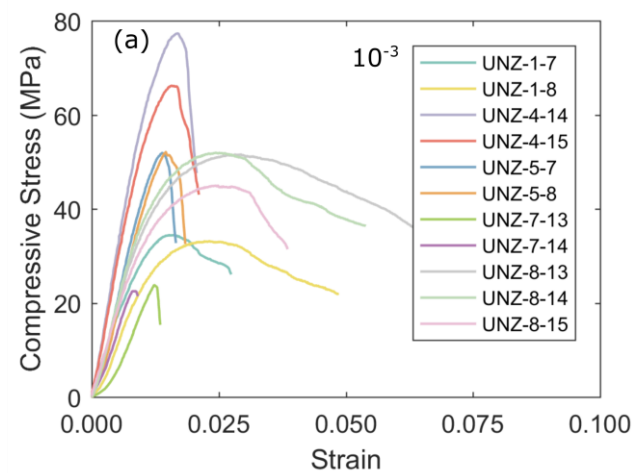
1700

Figure 7Figure 8. High temperature uniaxial experiment results, including stress-strain curves for samples tested at a strain rates of (a) 10^{-3} s^{-1}, (b) 10^{-4} s^{-1}, and (c) 10^{-5} s^{-1}, demonstrating the shift from viscous flow at low rate to increasingly brittle deformation at faster rate. (d) The peak stresses achieved during each experiment carried out at 900 ˚C further highlights this observation and shows the porosity dependence of strength in the brittle regime.
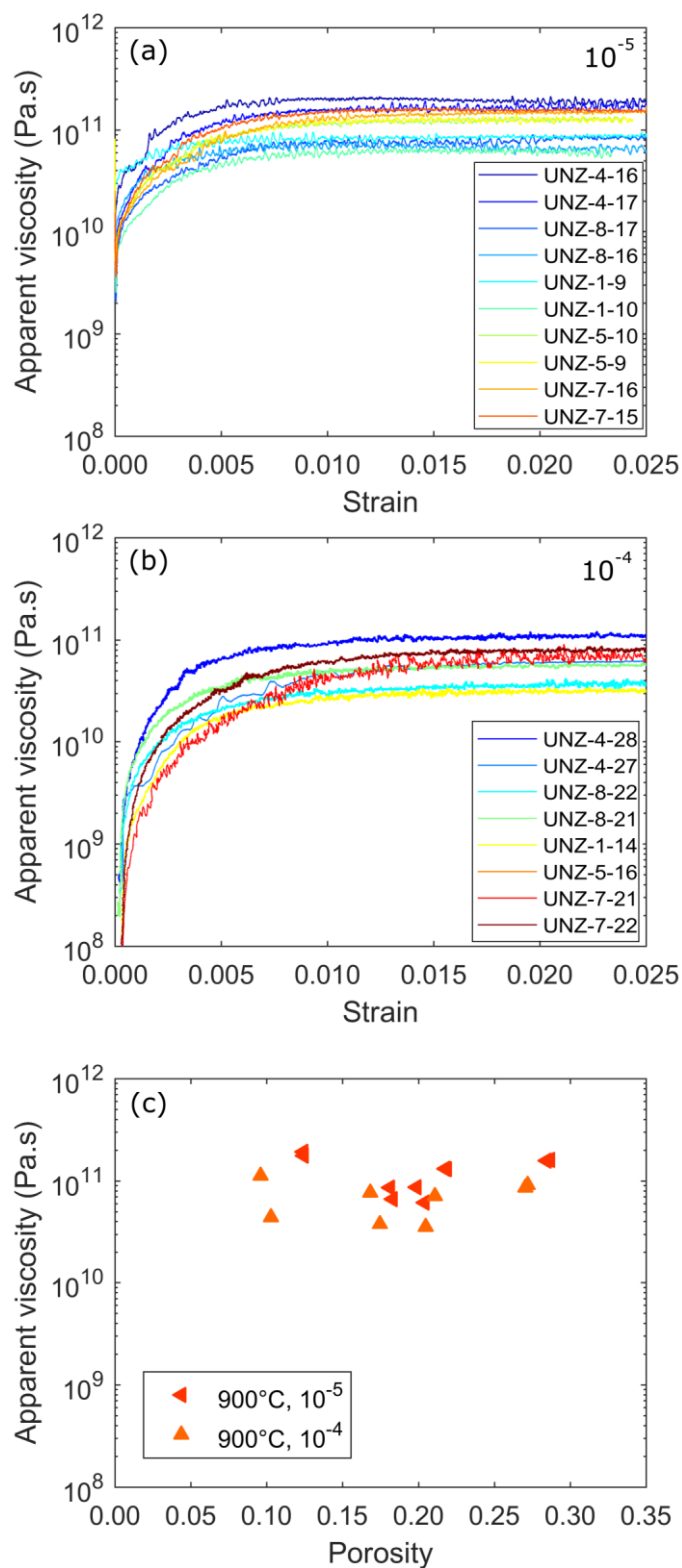
Figure 9~~8~~. Apparent viscosities of porous lavas at 900 °C for strain rates of (a) 10^{-5} s^{-1} and (b) 10^{-4} s^{-1}; colours warm from blue to red with increasing sample porosity. (c) Compilation of apparent viscosities as a function of porosity for samples tested at strain rates of 10^{-4} s^{-1} and 10^{-5} s^{-1}. Viscosities decrease between strain rates of 10^{-5} to 10^{-4} s^{-1}, an example of shear thinning in the Unzen samples. Porosity has no control on the apparent viscosities of the samples tested here.

1705
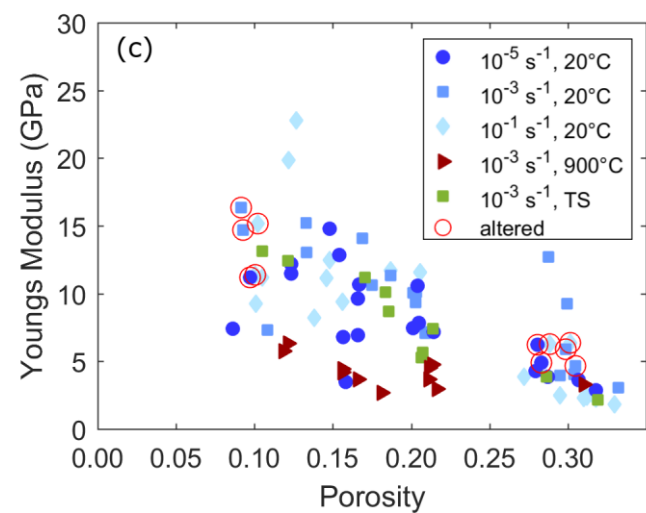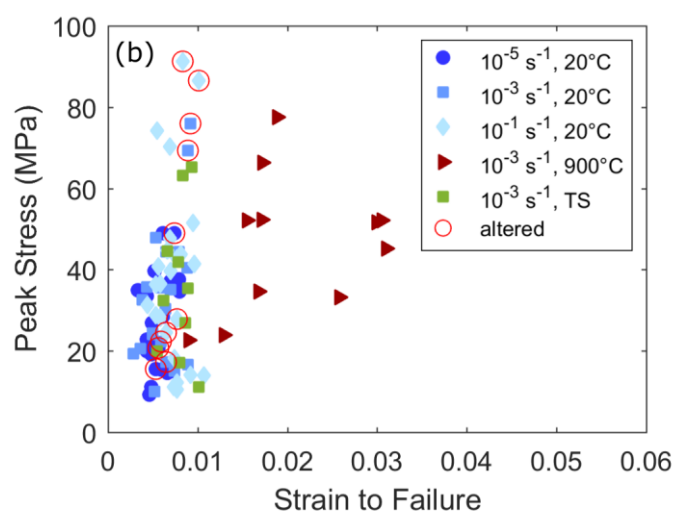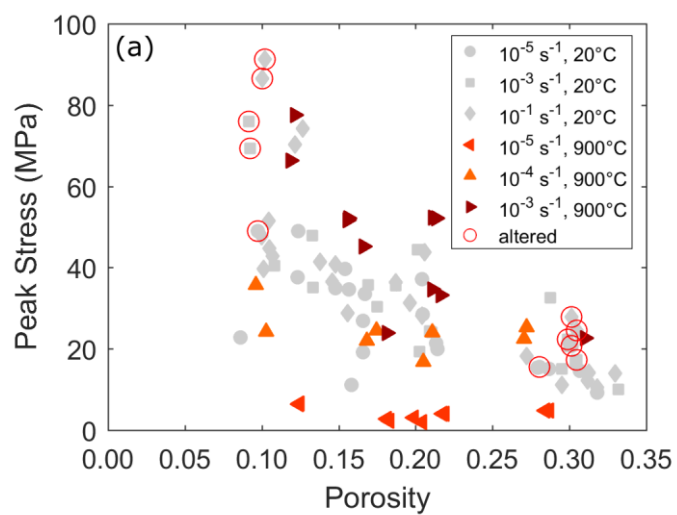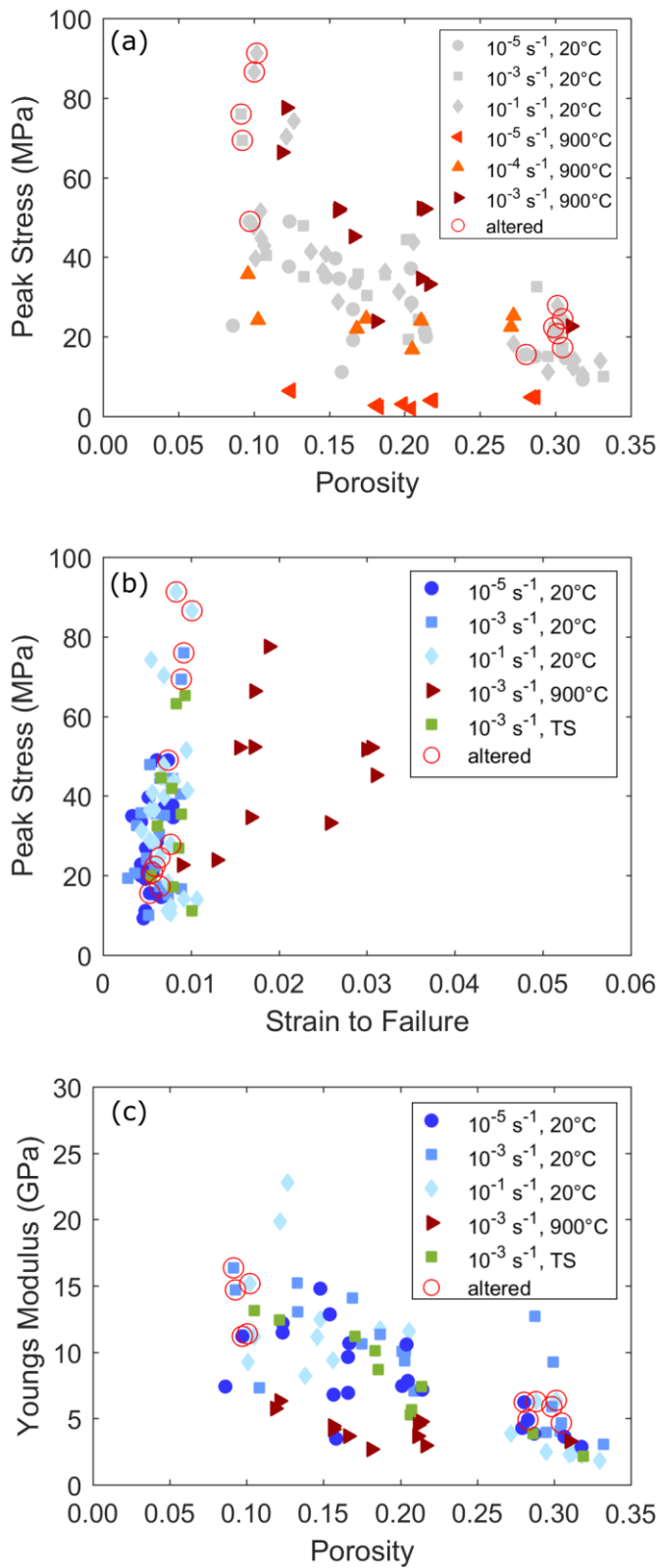
Figure 109. Strength and Young's Moduli of Unzen rocks and lavas at different conditions. Shades of blue represent tests carried out at ambient temperatures, shades of red indicate those performed at 900 °C, and ~~shades of~~ green depicts thermally stressed samples which were tested in ambient conditions. The red rings circle the samples which were deemed visibly altered at collection. (a) Peak stress with porosity for all completed experiments. Low temperature tests, as seen in Figure 5 (ab), are faded to grey. (b) Peak stress with strain at the point of sample failure (i.e. the stain at peak stress) for all experiments with a brittle response. (c) Young's modulus as a function of porosity for all samples that had a brittle response, calculated using the slope of the linear portion of the stress–strain curve (see Fig. S6).

Figure 11 Plot of uniaxial compressive stress against porosity showing the ambient temperature mechanical data (black dots), alongside contours of various values of $\frac{K_{IC}}{\sqrt{\pi r}}$ (5–25 MPa) from the pore–emanating crack model (Eq. 2). The range of UCS given by the wing-crack model is also plotted as a shaded region. The mechanical data are cross-cut by the contours, suggesting a change in the dominant porous structure. At porosities > 0.25 the UCS given by the pore-emanating crack model with $\frac{K_{IC}}{\sqrt{\pi r}}$ = 5–10 MPa seems to fit the data well. For porosities ranging from 0.12–0.2 the UCS given by the pore-emanating crack model with $\frac{K_{IC}}{\sqrt{\pi r}}$ = 10–15 MPa encloses the data. The UCS for the densest rocks in the study (~0.08–0.12) would suggest yet a higher $\frac{K_{IC}}{\sqrt{\pi r}}$ of 20–25 MPa. For porosities < 0.1 the UCS given by the wing–crack model is similar to the mechanical data (σ = 54.2–89.7 MPa).

1720

1725

Figure 10. (a) Peak stress plotted with strain rate for completed experiments, in semi-log space. The power law equation of the line is shown on the figure. Oswald constants k and b are 1606 and 0.7755 respectively. (b) The calculated Deborah number as a function of porosity for each sample tested at high temperature, in semi-log space. Depending on the shape of the stress-strain curve for each sample, it was labelled as viscous, transitional or brittle. The critical Deborah number, De_c, which marks the onset of brittle deformation is approximately 2.11×10^{-4}

1730

60

a)	VISCOUS	viscous dominated TRANSITIONAL	brittle dominated TRANSITIONAL	BRITTLE
	e.g. UNZ-8-16 strain rate: 10^{-5} s^{-1}	e.g. UNZ-8-21 strain rate: 10^{-4} s^{-1}	e.g. UNZ-8-14 strain rate: 10^{-3} s^{-1}	e.g. UNZ-4-14 strain rate: 10^{-3} s^{-1}
Sample				
Stress-strain curve	Peak stress: 2.3 MPa	Peak stress: 22.1 MPa	Strain at failure: 0.031 Peak stress: 52.1 MPa	Strain at failure: 0.019 Peak stress: 77.6 MPa
Descriptor	· Plateau in stress-strain curve · No drop in stress with strain · After deformation the sample has no visible fractures · In BSE images (Fig. S7), microfractures seen in crystals only. Enlongated pores show sense of shear	· Plateau in stress-strain curve [note the rise in stress with strain here is due to uncorrected area effect] · Small drops in stress with strain · After deformation the sample is intact but has small visible fractures · In BSE images (Fig. S7), microfractures are pervasive through crystals and groundmass. No displacement of phenocrysts	· Peak in stress-strain curve · Major drop · in stress with strain · After deformation the sample may be intact but has one or more large visible fractures · In BSE images (Fig. S7), macroscopic fractures propagate through ground mass and displace phenocryts along their cleavage planes	· Peak in stress-strain curve · Major drop in stress with strain · After deformation the sample has fully ruptured · In BSE images (Fig. S7), macroscopic fractures propagate through crystals and groundmass

b)

$\sigma = 1653 \dot{\varepsilon}_{exp}^{0.5}$
$R^2 = 0.8$

c)

1735

61

1740

1745

Figure 12. (a) A schematic demonstration of sample rheological classification [viscous, viscous–dominated transitional (visc-trans), brittle–dominated transitional (brit-trans) or brittle], depending on the respective shape of the stress-strain curve and the amount of strain experienced (b) Peak stress plotted with strain rate for completed experiments in semi-log space. The power law equation of the line is shown on the figure. Ostwald constants k and b are 1653 and 0.5 respectively. The standard error of estimate is shown on the plot as the yellow window, along with the R^2 value (c) The calculated Deborah number as a function of porosity for each sample tested at high temperature, in semi-log space. The viscous–dominated transitional behaviour is marked by the red line bordered by a red window showing the standard estimate of error. The brittle–dominated transitional behaviour is marked by the yellow line bordered by a yellow window showing the standard estimate of error. The critical Deborah number, De_c, can thus be said to be between 1×10^{-4} and 6.6×10^{-4} for dense (pore-free) crystal-rich dome lavas, deceasing linearly with the addition of pores. We find that the two transitional zones converge at a porosity of approximately 0.27, beyond which, no transition zone exists (although this coincide with the limit of the material properties studied). [NOTE: Sample UNZ-4-28 was omitted from this plot as its resulting stress-strain curve was likely due to an experimental artefact caused by chipping of the sample edge]

Sample	Total porosity	Connected porosity	Strain rate (s^{-1})	Temperature (°C)	Peak force (N)	Peak Stress (MPa)	Strain to failure	Thermally treated	Altered	Viscosity (Pa.s)	De number	Young's modulus (GPa)
UNZ-1-2	0.21	0.19	1.E-05	20	6789	21.38	0.0049	N	N	N/A	N/A	7.45
UNZ-4-13	0.09	0.07	1.E-05	20	7180	22.71	0.0043	N	N	N/A	N/A	7.40
UNZ-5-1	0.20	0.18	1.E-05	20	11779	37.09	0.0070	N	N	N/A	N/A	10.58
UNZ-5-5	0.20	0.19	1.E-05	20	9022	28.49	0.0061	N	N	N/A	N/A	7.84
UNZ-7-1	0.29	0.28	1.E-05	20	4750	15.10	0.0071	N	N	N/A	N/A	3.85
UNZ-7-10	0.31	0.30	1.E-05	20	4600	14.63	0.0066	N	N	N/A	N/A	3.63
UNZ-7-12	0.32	0.31	1.E-05	20	2895	9.20	0.0046	N	N	N/A	N/A	2.86
UNZ-7-6	0.28	0.28	1.E-05	20	4889	15.41	0.0060	N	N	N/A	N/A	4.27
UNZ-8-1	0.17	0.17	1.E-05	20	6000	19.15	0.0048	N	N	N/A	N/A	6.93
UNZ-8-10	0.15	0.15	1.E-05	20	12570	39.62	0.0052	N	N	N/A	N/A	12.84
UNZ-8-12	0.17	0.14	1.E-05	20	10600	33.44	0.0043	N	N	N/A	N/A	10.67
UNZ-8-6	0.17	0.17	1.E-05	20	8540	26.90	0.0049	N	N	N/A	N/A	9.65
UNZ-4-25	0.16	0.14	1.E-05	20	3497	11.07	0.0048	N	N	N/A	N/A	3.48
UNZ-4-26	0.16	0.11	1.E-05	20	10981	34.64	0.0080	N	N	N/A	N/A	6.79
UNZ-1-0	0.21	0.19	1.E-05	20	6320	19.92	0.0043	N	N	N/A	N/A	7.16
UNZ-2-4	0.12	0.10	1.E-05	20	13361	41.98	0.0061	N	N	N/A	N/A	12.19
UNZ-2-5	0.12	0.10	1.E-05	20	11957	37.68	0.0079	N	N	N/A	N/A	11.50
UNZ-12-4	0.10	0.09	1.E-05	20	15549	48.95	0.0074	N	Y	N/A	N/A	11.18
UNZ-11-2	0.30	0.28	1.E-05	20	6592	20.71	0.0056	N	Y	N/A	N/A	6.21
UNZ-11-3	0.28	0.27	1.E-05	20	4950	15.60	0.0053	N	Y	N/A	N/A	4.88
UNZ-8-21	0.15	0.12	1.E-05	20	11073	34.90	0.0033	N	N	N/A	N/A	14.77
UNZ-1-4	0.21	0.18	1.E-03	20	7681	24.42	0.0050	N	N	N/A	N/A	7.06
UNZ-1-6	0.21	0.18	1.E-03	20	7639	24.08	0.0050	N	N	N/A	N/A	7.19
UNZ-5-2	0.20	0.18	1.E-03	20	14081	44.47	0.0079	N	N	N/A	N/A	10.04
UNZ-5-3	0.20	0.19	1.E-03	20	14065	44.33	0.0065	N	N	N/A	N/A	10.11
UNZ-7-11	0.33	0.33	1.E-03	20	3150	9.98	0.0052	N	N	N/A	N/A	3.05

UNZ-7-2	0.30	0.29	1.E-03	20	5250	16.70	0.0089	N	N	N/A	N/A	4.05
UNZ-7-7	0.30	0.29	1.E-03	20	4750	15.01	0.0074	N	N	N/A	N/A	3.97
UNZ-8-11	0.19	0.17	1.E-03	20	11300	35.53	0.0059	N	N	N/A	N/A	11.32
UNZ-8-3	0.18	0.15	1.E-03	20	9640	30.39	0.0064	N	N	N/A	N/A	10.63
UNZ-8-7	0.17	0.14	1.E-03	20	11350	35.73	0.0043	N	N	N/A	N/A	14.08
UNZ-4-24	0.11	0.09	1.E-03	20	12841	40.47	0.0088	N	N	N/A	N/A	7.30
UNZ-2-1	0.13	0.11	1.E-03	20	15241	47.94	0.0053	N	N	N/A	N/A	15.22
UNZ-2-6	0.13	0.11	1.E-03	20	11115	35.13	0.0070	N	N	N/A	N/A	13.04
UNZ-13-1	0.29	0.27	1.E-03	20	10341	32.52	0.0038	N	N	N/A	N/A	12.70
UNZ-13-2	0.30	0.29	1.E-03	20	6544	20.58	0.0036	N	N	N/A	N/A	9.25
UNZ-12-1	0.09	0.09	1.E-03	20	22126	69.32	0.0089	N	Y	N/A	N/A	14.71
UNZ-12-3	0.09	0.10	1.E-03	20	24227	75.97	0.0092	N	Y	N/A	N/A	16.33
UNZ-11-4	0.30	0.30	1.E-03	20	7066	22.25	0.0059	N	Y	N/A	N/A	5.90
UNZ-11-6	0.30	0.30	1.E-03	20	5507	17.32	0.0065	N	Y	N/A	N/A	4.65
UNZ-1-14	0.20	0.18	1.E-03	20	7681	19.25	0.0028	N	N	N/A	N/A	9.34
UNZ-1-11	0.19	0.16	1.E-03	20	10257	32.36	0.0062	Y	N	N/A	N/A	8.69
UNZ-1-12	0.21	0.18	1.E-03	20	6334	19.92	0.0055	Y	N	N/A	N/A	5.26
UNZ-4-18	0.10	0.09	1.E-03	20	20556	65.17	0.0093	Y	N	N/A	N/A	13.11
UNZ-4-19	0.12	0.10	1.E-03	20	19939	63.22	0.0083	Y	N	N/A	N/A	12.40
UNZ-5-11	0.21	0.21	1.E-03	20	11240	35.42	0.0089	Y	N	N/A	N/A	7.39
UNZ-5-12	0.21	0.21	1.E-03	20	8515	26.89	0.0086	Y	N	N/A	N/A	5.64
UNZ-7-17	0.29	0.29	1.E-03	20	5412	17.16	0.0080	Y	N	N/A	N/A	3.87
UNZ-7-18	0.32	0.32	1.E-03	20	3515	11.10	0.0101	Y	N	N/A	N/A	2.14
UNZ-8-18	0.18	0.16	1.E-03	20	13266	41.81	0.0078	Y	N	N/A	N/A	10.10
UNZ-8-19	0.17	0.15	1.E-03	20	14175	44.63	0.0066	Y	N	N/A	N/A	11.19
UNZ-1-1	0.20	0.17	1.E-01	20	9970	31.33	0.0044	N	N	N/A	N/A	9.83
UNZ-1-3	0.20	0.18	1.E-01	20	8936	28.11	0.0058	N	N	N/A	N/A	8.66
UNZ-4-20	0.10	0.09	1.E-01	20	16342	51.55	0.0095	N	N	N/A	N/A	8.51

UNZ-4-22	0.14	0.09	1.E-01	20	13050	41.33	0.0096	N	N	N/A	N/A	8.20
UNZ-4-4	0.11	0.09	1.E-01	20	13580	42.84	0.0077	N	N	N/A	N/A	9.18
UNZ-4-5	0.10	0.08	1.E-01	20	15160	47.67	0.0069	N	N	N/A	N/A	11.05
UNZ-4-8	0.11	0.09	1.E-01	20	14200	44.69	0.0066	N	N	N/A	N/A	11.20
UNZ-4-9	0.10	0.09	1.E-01	20	12580	39.67	0.0070	N	N	N/A	N/A	9.24
UNZ-7-19	0.31	0.36	1.E-01	20	4492	14.16	0.0092	N	N	N/A	N/A	2.32
UNZ-7-20	0.33	0.32	1.E-01	20	4442	14.03	0.0107	N	N	N/A	N/A	1.82
UNZ-7-4	0.30	0.29	1.E-01	20	3546	11.18	0.0073	N	N	N/A	N/A	2.49
UNZ-7-5	0.32	0.31	1.E-01	20	3300	10.43	0.0077	N	N	N/A	N/A	2.27
UNZ-7-8	0.31	0.31	1.E-01	20	3858	12.15	0.0077	N	N	N/A	N/A	2.38
UNZ-7-9	0.27	0.26	1.E-01	20	5802	18.29	0.0074	N	N	N/A	N/A	3.85
UNZ-8-4	0.15	0.12	1.E-01	20	11600	36.56	0.0058	N	N	N/A	N/A	11.12
UNZ-8-5	0.19	0.16	1.E-01	20	11540	36.42	0.0053	N	N	N/A	N/A	11.71
UNZ-8-8	0.16	0.13	1.E-01	20	9125	28.79	0.0053	N	N	N/A	N/A	9.39
UNZ-8-9	0.15	0.12	1.E-01	20	12910	40.71	0.0056	N	N	N/A	N/A	12.47
UNZ-2-2	0.13	0.10	1.E-01	20	23562	74.18	0.0055	N	N	N/A	N/A	22.79
UNZ-2-3	0.12	0.10	1.E-01	20	22309	70.24	0.0069	N	N	N/A	N/A	19.83
UNZ-12-2	0.10	0.10	1.E-01	20	29086	91.30	0.0083	N	Y	N/A	N/A	15.15
UNZ-12-5	0.10	0.10	1.E-01	20	27638	86.58	0.0101	N	Y	N/A	N/A	11.36
UNZ-11-1	0.30	0.29	1.E-01	20	8840	27.80	0.0077	N	Y	N/A	N/A	6.35
UNZ-11-5	0.30	0.29	1.E-01	20	7780	24.47	0.0065	N	Y	N/A	N/A	6.25
UNZ-5-15	0.21	0.17	1.E-01	20	13805	43.81	0.0081	N	N	N/A	N/A	11.58
UNZ-1-10	0.20	0.18	1.E-05	900	643	2.02	N/A	N	N	1.40E+11	5.17E-07	N/A
UNZ-1-9	0.20	0.17	1.E-05	900	975	3.08	N/A	N	N	8.98E+10	1.20E-06	N/A
UNZ-4-16	0.12	0.11	1.E-05	900	2041	6.41	N/A	N	N	2.87E+11	5.22E-06	N/A
UNZ-4-17	0.12	0.11	1.E-05	900	2077	6.56	N/A	N	N	2.86E+11	5.46E-06	N/A
UNZ-5-10	0.22	0.20	1.E-05	900	1294	4.06	N/A	N	N	1.77E+11	2.09E-06	N/A
UNZ-5-9	0.22	0.20	1.E-05	900	1277	4.02	N/A	N	N	1.71E+11	2.05E-06	N/A

UNZ-7-15	0.29	0.28	1.E-05	900	1540	4.87	N/A	N	N	2.06E+11	3.01E-06	N/A
UNZ-7-16	0.28	0.27	1.E-05	900	1475	4.80	N/A	N	N	2.01E+11	2.93E-06	N/A
UNZ-8-16	0.18	0.16	1.E-05	900	652	2.30	N/A	N	N	9.09E+10	6.70E-07	N/A
UNZ-8-17	0.18	0.16	1.E-05	900	829	2.72	N/A	N	N	1.09E+11	9.40E-07	N/A
UNZ-4-27	0.10	0.09	1.E-04	900	4696	24.28	N/A	N	N	4.55E+10	7.48E-05	N/A
UNZ-7-21	0.27	0.26	1.E-04	900	7117	22.52	0.0851	N	N	8.38E+10	6.43E-05	N/A
UNZ-4-28	0.10	0.08	1.E-04	900	11337	35.73	0.0529	N	N	1.20E+11	1.62E-04	N/A
UNZ-7-22	0.27	0.26	1.E-04	900	8010	25.27	0.0285	N	N	8.62E+10	8.10E-05	N/A
UNZ-8-21	0.17	0.15	1.E-04	900	7012	22.05	N/A	N	N	7.19E+10	6.17E-05	N/A
UNZ-8-22	0.17	0.14	1.E-04	900	7843	24.60	N/A	N	N	3.83E+10	7.68E-05	N/A
UNZ-5-16	0.21	0.19	1.E-04	900	7625	24.08	N/A	N	N	7.17E+10	7.36E-05	N/A
UNZ-1-14	0.20	0.18	1.E-04	900	5278	16.78	N/A	N	N	3.60E+10	3.57E-05	N/A
UNZ-1-7	0.21	0.19	1.E-03	900	11044	34.70	0.0168	N	N	N/A	1.53E-04	3.65
UNZ-1-8	0.22	0.19	1.E-03	900	10637	33.23	0.0258	N	N	N/A	1.40E-04	2.93
UNZ-4-14	0.12	0.10	1.E-03	900	24575	77.60	0.0189	N	N	N/A	7.64E-04	6.32
UNZ-4-15	0.12	0.11	1.E-03	900	21048	66.40	0.0172	N	N	N/A	5.59E-04	5.75
UNZ-5-7	0.21	0.19	1.E-03	900	16503	52.06	0.0155	N	N	N/A	3.44E-04	4.76
UNZ-5-8	0.21	0.09	1.E-03	900	16566	52.21	0.0171	N	N	N/A	3.46E-04	4.53
UNZ-7-13	0.31	0.31	1.E-03	900	7583	23.90	0.0129	N	N	N/A	7.24E-05	2.67
UNZ-7-14	0.31	0.30	1.E-03	900	7187	22.70	0.0090	N	N	N/A	6.54E-05	3.30
UNZ-8-13	0.16	0.13	1.E-03	900	16384	51.63	0.0299	N	N	N/A	3.38E-04	4.19
UNZ-8-14	0.16	0.13	1.E-03	900	16571	52.07	0.0305	N	N	N/A	3.44E-04	4.43
UNZ-8-15	0.17	0.14	1.E-03	900	14382	45.19	0.0310	N	N	N/A	2.59E-04	3.68
UNZ-1-x	0.22	0.21	1.E-06	900	127	0.34	N/A	N	N	1.20E+11	3.47E-07	N/A
UNZ-1-x	0.22	0.21	1.E-05	900	610	1.94	N/A	N	N	7.00E+10	N/A	N/A
UNZ-1-x	0.22	0.21	1.E-04	900	3682	11.72	N/A	N	N	3.85E+10	N/A	N/A
UNZ-1-x	0.22	0.21	1.E-03	900	8383	26.68	0.9180	N	N	N/A	N/A	N/A

Table 1. Sample properties, measurement data, experimental conditions, mechanical response and resulting properties of each sample.

	XRF			Microprobe	
	UNZ-4	UNZ-11	UNZ-12	UNZ-4 glass	standard deviation
SiO₂	64.07	65.2	65.48	79.20	0.20
TiO₂	0.67	0.66	0.61	0.40	0.01
Al₂O₃	16.34	15.98	16.39	11.13	0.02
Fe₂O₃	4.84	4.67	4.35	-	-
FeO	-	-	-	0.92	0.01
MnO	0.10	0.10	0.09	0.01	0.01
MgO	2.57	2.37	2.02	0.07	0.02
CaO	5.18	4.55	4.63	0.56	0.02
Na₂O	3.61	3.56	3.69	2.83	0.09
K₂O	2.31	2.55	2.46	4.87	0.07
P₂O₅	0.17	0.12	0.15	-	-
LOI	0.14	0.23	0.14	-	-
Total	100	100	100	100	0

1750 **Table 2. Normalised chemical composition of bulk rocks obtained by XRF analysis and interstitial glass obtained by EPMA. UNZ-4 was selected as it is representative of fresh lavas tested in this study; in contrast, UNZ-11 and UNZ-12 were deemed to display a certain degree of alteration. Original totals were 99.97, 100.39, 100.09, and 99.95 for UNZ-4, UNZ-12, UNZ-11, UNZ-4 glass, respectively, before normalisation for direct comparison. The standard deviation of the UNZ-4 glass was taken from 2 measurements.**

1755

Sample block name	Average total porosity	Standard deviation	Average connected porosity	Standard deviation	Average isolated porosity	Standard deviation	No. samples
UNZ-1	0.21	0.011	0.18	0.012	0.02	0.002	17
UNZ-2	0.13	0.016	0.11	0.018	0.02	0.003	7
UNZ-4	0.12	0.016	0.12	0.021	0.00	0.016	30
UNZ-5	0.21	0.006	0.19	0.009	0.02	0.006	18
UNZ-7	0.30	0.024	0.29	0.025	0.01	0.002	23
UNZ-8	0.16	0.016	0.14	0.016	0.02	0.003	24
UNZ-11	0.30	0.009	0.29	0.011	0.01	0.004	8
UNZ-12	0.10	0.025	0.09	0.026	0.00	0.002	7
UNZ-13	0.32	0.005	0.30	0.004	0.01	0.004	6

Table 3. Average total, connected, and isolated porosities for each sample block used. A larger number of cores were measured to calculate the average porosities than those used in strength tests. *Note: values are presented to 2 d.p. but were calculated with 4 d.p.*

1760